Politecnico di Torino

Corso di Laurea Magistrale in
Ingegneria Aerospaziale

A.a. 2025/2026
Sessione di Laurea Marzo/Aprile 2026

Experimental analysis of fuel cell system and modelling for drone application

Relatori:
Massimo Santarelli
Mohsen Mansourkiaei

Candidato:
Simone Chiale

Table of contents

Table of figures

Table of tables

Abstract

This thesis investigates the experimental assessment of a hybrid propulsion system for unmanned aerial vehicles (UAVs), combining hydrogen fuel cells with batteries. The motivation arises from the growing demand for sustainable aerial propulsion solutions capable of extending flight endurance while minimizing environmental impact.

Fuel cells, characterized by high efficiency and zero local emissions, are presented in the first part of the work through a theoretical overview of their operating principles and a review of their applicability in the drone sector. Particular emphasis is placed on the benefits and challenges associated with hybrid configurations, where batteries support dynamic load variations while fuel cells provide continuous power.

The second part of the thesis describes the design and implementation of the experimental test bench, which was specifically developed to reproduce realistic operating conditions of the hybrid system. The architecture, instrumentation and data acquisition strategy are detailed to provide a comprehensive framework for performance evaluation.

The third section presents and discusses experimental results, focusing on the energy management between the fuel cell and the battery, the system's efficiency, and its contribution to extending the UAV's endurance compared to conventional powertrains. The findings highlight the potential of fuel cell-battery hybridization in addressing the limitations of current drone technologies, offering insights for further research and development in the field of sustainable aviation.

Chapter 4 concludes with the modeling of a hexacopter drone and the analysis of multiple alternative configurations that differ in fuel cell systems and hydrogen storage solutions. The study evaluates the potential advantages and disadvantages of each configuration in terms of endurance and payload capacity, identifying conditions under which specific setups may offer superior performance.

Ultimately, this work contributes to the growing body of knowledge that supports hydrogen fuel cells as a promising pathway for the future of clean and efficient aerial propulsion.

1 Introduction

1.1 Motivation

Depending on their design, drones can be classified into three categories: fixed-wing, single-rotor, and multi-rotor [1].

Multirotor drones have some advantages, like a small take-off and landing footprint, good positioning control, being able to hover in the same geographical location, and being able to carry payloads at both low and high velocities. They typically have a take-off mass of up to 25 kg and a payload capacity of almost 5 kg.

Equipped by different tools and sensors, they are highly suitable for precision agriculture, aerial filming, inspections, delivery, wireless coverage, thermal imaging, and many other types of missions in various fields, including commercial use and other engineering applications. They had also been useful in COVID-19 pandemic handling, by means of social distancing monitoring [2].

They also offer beneficial performance features, including excellent mobility, reliability, energy efficiency, and minimal heat and noise emissions.

In line with what has been stated so far, multi-rotor drones are currently the mainstream product in the drone market.

Most commercialized drones are powered by batteries as unique power sources due to their low cost and simplicity. However, batteries have a relatively low energy density (the current state-of-the-art lithium-polymer batteries have a specific energy of 130-200 Wh/kg) that results in short flight time of drone and obstruction of long and persistent missions. Increasing battery capacity cannot be a practical solution due to the weight constraint. A possible solution is represented by fuel cells-hydrogen power systems, which can have twice the energy density of traditional lithium batteries.

When evaluating different electrical energy storage technologies, it is often helpful to compare their energy density and power density using a Ragone plot, as illustrated in Figure 1. The regions indicated for each technology on the plot serve as a general reference for where various technologies typically fall. The performance of these technologies spans a wide range, from the upper-left region (high energy storage, low power density) to the lower-right region (low energy density, high power density). No single technology simultaneously achieves very high energy and power densities, which partly explains the increasing interest in hybrid systems (note that both axes are presented on a logarithmic scale) [3].

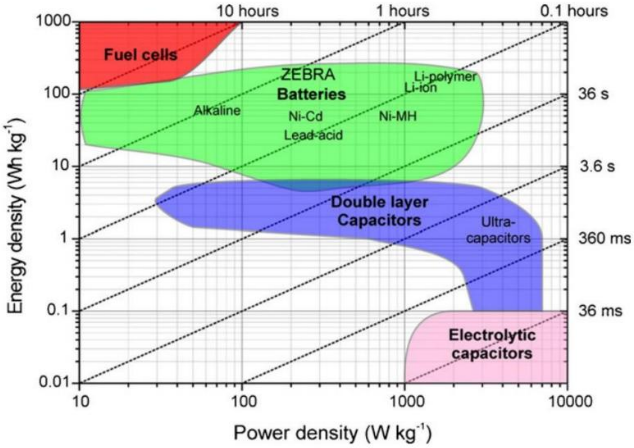

Figure 1: Energy density vs. power density of various energy storage technologies [3]

Fuel cell hybrid systems have been found to be capable of providing a specific energy of 250-540 Wh/kg on a power system level. Moreover, refuelling can be done quickly, unlike batteries, which generally require more time to recharge. Furthermore, fuel cells have a very low environmental impact: as in most types (like PEMFC) their only byproduct is water.

A recent study ([4], [5]), examined the performance of multirotor drones powered by either fuel cell hybrid systems (FCHS) or batteries. Based on the evaluation model used, FCHS outperforms batteries in terms of endurance when the power system weighs more than 7.3 kg (Figure 2).

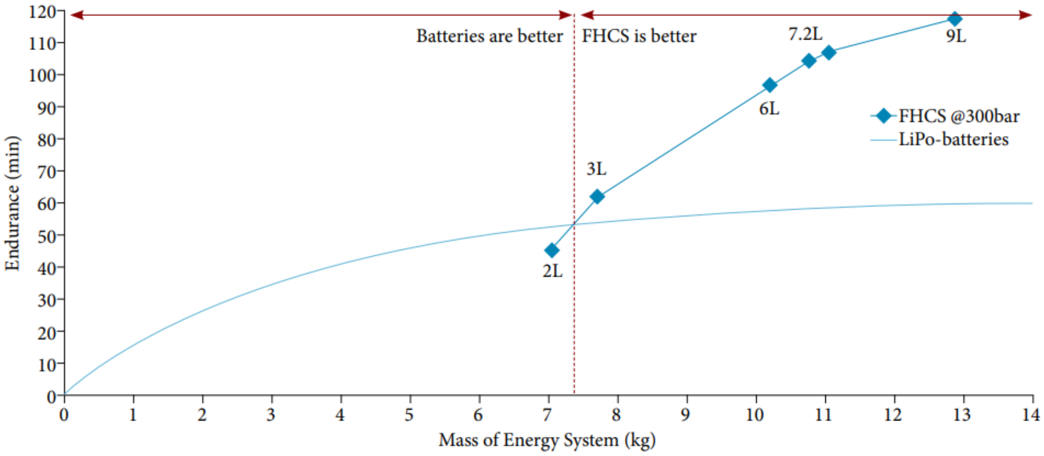

Figure 2: Endurance plot for various power sources as a function of system mass. Note that a minimum battery mass is required to provide sufficient power to take off [5]

Using a commercially available multirotor drone with a maximum take-off weight of 25 kg as a case study, the results showed that endurance improved by 76% with the use of FCHS.

In the battery-powered version, the increase in E/P is smaller compared to the Fuel Cell Hybrid System (FCHS) as we move to the right in the diagram.

$$P \propto (m_{Fr} + m_{SS})^{\frac{3}{2}} ; E \propto m_{SS}$$

$$t = \frac{E}{P}$$

When additional structural or system mass is added, the power demand increases faster than the stored energy in the battery case, leading to a smaller improvement in endurance compared to the FCHS configuration.

1.2 Fuel Cells

Fuel cells produce electricity in an electrochemical reaction combining hydrogen and oxygen. This reaction is exothermic (releases heat) and its only byproduct is water. Traditional electricity production involves a three-step energy conversion process: from chemical to thermal, then from thermal to mechanical, and finally from mechanical to electrical energy. Instead, in a fuel cell, chemical energy is transformed directly into electrical energy [6].

The most commonly used types of fuel cells (FC) are PEMFC (Proton Exchange Membrane FC), DMFC (Direct Methanol FC), and SOFC (Solid Oxide FC). The options differ in operating temperature ranges, the materials they use, their performance levels, and how well they handle various fuels.

The proton exchange membrane fuel cell (PEMFC) is very simple and represents the most used type for FC powered UAVs. The electrolyte is a polymer membrane that protons can move through, and a platinum catalyst is used to achieve sufficient reaction rates at low temperatures. They have relatively high-power density, a short start-up time and have high technical maturity. In addition, they simply adapt to load changes. They require extremely pure hydrogen (99.999%) and are susceptible to contamination from carbon monoxide (CO) and hydrogen sulphide (H_2S).

Direct methanol fuel cells (DMFC) are similar to PEM fuel cells and also operate at low temperatures. The term direct is used because this type of cells directly oxidizes methanol. The main advantage is simple fuel management, but they have a very low power density. Thus, they are best for applications with low and steady power consumption for long durations.

Solid Oxide Fuel Cells (SOFCs) are characterized by very high operating temperatures. Because of this, they have a high reaction rate without any expensive catalyst, and they can run on natural gases such as propane and methane, which are readily available and simple to store. However, thermal management can be complex, they adapt slowly to load fluctuations, and it does take some time to get up to operational temperature. The ceramic materials used are difficult to handle and manufacture due to their high cost, and they experience high thermal stress. So, additional sub-systems must be added to pre-heat the air.

Table 1 summarizes their characteristics, advantages, and disadvantages.

Table 1: Comparison of various fuel cells [7]

	DMFC	**PEMFC**	**SOFC**
Operating temperature (°C)	60-130	< 120	800-1000
Released power (kW)	< 5	5-250	100-250
Type of electrolyte	Nafion membrane	Nafion membrane	Yttria stabilized zirconia
Anode reaction	$CH_3OH + H_2O \text{ -> } CO_2 + 6H^+ + 6e^-$	$H_2 \text{ -> } 2H^+ + 2e^-$	$H_2 + O^{2-} \text{ -> } H_2O + 2e^-$
Cathode reaction	$3/2O_2 + 6H^+ + 6e^- \text{ -> } 3H_2O$	$1/2O_2 + 2H^+ + 2e^- \text{ -> } H_2O$	$1/2O_2 + 2e^- \text{ -> } O^{2-}$
Advantages	Easy fuel storage, simple structure without thermal management	High power density, fast startup	Diversified fuel, non-noble metal for catalyst
Disadvantages	Low power density, CO_2 emissions	Low energy density of storing hydrogen at high pressure or in metal hydride	Slow startup and complex auxiliary equipments due to high operating temperature

Low power density, slow start-up time, and slow load adjusting characteristics do not make SOFC and DMFC attractive options for multi-rotor drone applications. They might be attractive options for fixed-wing UAVs, which operate at lower power levels and more continuous loads [8].

Thanks to their lightweight, high-energy density, low operating temperature, and fast startup, PEMFCs are the most widely used fuel cells for drone applications.

1.3 Proton Exchange Membrane Fuel Cell (PEMFC)

Figure 3 shows the typical structure of a PEMFC.

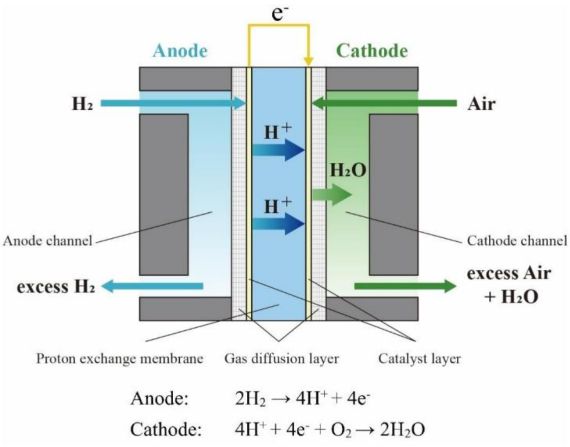

Figure 3: Proton exchange membrane fuel cells (PEMFC) single-cell structure [9]

1.3.1 Bipolar plates

The bipolar plates make up about 80% of the total weight of a fuel cell stack [10]. Therefore, it is important to design lightweight bipolar plates to decrease the weight of fuel cell systems.

Bipolar plates play a fundamental role in PEMFCs operation: they provide an electrical pathway for electrons between adjacent cells, mechanical support for the stack, channels that enable uniform distribution of reactant gases across the electrodes and the effective removal of by-products such as water and heat. The performance of a fuel cell (its efficiency, power density, and energy density) is therefore strongly influenced by the behaviour of the bipolar plates during operation. Their main properties, including electrical conductivity, gas impermeability, hydrophobicity, and mechanical and electrochemical durability are strongly influenced by the material selection, manufacturing process, and flow-field design. As a result, optimizing these aspects is essential to ensure reliable, efficient, and long-lasting operation of PEM fuel cells. [11].

Most commonly used materials for bipolar plates include graphite, metals, and composites [12]. Graphite materials have been used in the production of bipolar plates for a long time thanks to their low density, good corrosion resistance, and great compatibility with carbon fiber diffusion layers. However, due to their low strength and high brittleness, graphite bipolar plates are typically made with a high thickness to meet the stack's strength requirements, resulting in an increase in the volume and mass of the stack [13].

Composite bipolar plates are made by injection molding a polymer resin with conductive fillers, such as graphite [14]. They have a higher specific resistance than graphite plates, offering significant advantages in lightweight design. However, due to their complex manufacturing process and high cost, composite bipolar plates are not yet widely used. With the development of 3D printing, researchers are attempting to adapt this technology to simplify the production process.

Although composite bipolar plates generally offer better strength compared to graphite plates and can be produced with reduced thickness and weight, they face significant limitations in terms of thickness and volume when compared to metal ones, due to the inherent characteristics of the materials and the hot compaction processes involved. In addition to the advantages in thickness and volume, metal materials offer good electrical conductivity and workability and can be directly molded through stamping, which is why they are currently the most commonly used materials for bipolar plates [15].

Common metal materials used for the production of bipolar plates include stainless steel, aluminum alloys, magnesium alloys, and titanium alloys. From a lightweight design perspective, lightweight alloys, such as titanium and aluminum alloys, have a lower density compared to stainless steel. Additionally, titanium alloys offer higher specific strength and superior corrosion resistance. The corrosion products generated by titanium alloys during prolonged use have minimal toxicity on the proton exchange membrane, making them ideal materials for bipolar plates [16].

However, similar to other metal bipolar plates, after prolonged use, a passivation film forms on titanium alloy bipolar plates, which increases the resistivity of the plate and reduces the output power of the fuel cell. To avoid this phenomenon, the surface of the bipolar plate must be modified. Based on the materials, the main surface modification methods include carbon modification, chromium and chromium compound modification, nitriding, and modification with precious metals [17].

Due to the high cost of titanium bipolar plates, they are rarely studied and applied, making stainless steel the most commonly used metal material for bipolar plates.

1.3.2 Membrane Electrode Assembly

The membrane electrode assembly (MEA) is the central component of a PEMFC and is constructed by superimposing the polymer membrane, catalyst layers, and gas diffusion layers. It is therefore a multilayered system in which each layer interacts closely with the others, jointly determining the cell's overall electrochemical performance. The choice of constituent materials and the final architecture of the MEA play a fundamental role in ensuring high efficiency, operational stability, and system durability [18].

1.3.2.1 Gas Diffusion Layer

The gas diffusion layer (GDL) is a critical component in fuel cells, consisting of a thin, carbon-based structure positioned between the catalyst layer and the polymer electrolyte membrane. Its primary functions are to facilitate the uniform distribution of reactant gases (hydrogen and oxygen) to the catalyst sites, efficiently remove water produced during the electrochemical reaction, provide a conductive path for electrons, and mechanically support and protect the catalyst layer. Structurally, the GDL typically comprises two distinct regions: a macroporous layer, which ensures bulk gas transport and mechanical stability, and a microporous layer, which enhances contact with the catalyst layer and promotes uniform reactant distribution. To further optimize water management and prevent flooding, GDLs are often treated with hydrophobic agents, such as polytetrafluoroethylene (PTFE), commonly also known as Teflon, which improve water expulsion while maintaining gas permeability and electrical conductivity [19].

1.3.2.2 Catalyst Layer

The catalyst layer is typically deposited directly onto the surface of the polymer electrolyte membrane and is positioned between the gas diffusion layer and the membrane. It constitutes the site where the electrochemical reactions take place: the hydrogen oxidation reaction at the anode and the oxygen reduction reaction at the cathode. As depicted in Figure 3, reactions are:

$$Anode\ (oxidation):\ \ 2H_2 \rightarrow 4H^+ + 4e^-$$

$$Cathode\ (reduction):\ \ 4H^+ + 4e^- + O_2 \rightarrow 2H_2O$$

The structural and morphological characteristics of the CL have a direct impact on the overall performance of the fuel cell, as they govern the kinetics of the electrochemical reactions and the effective utilization of the catalyst material.

The active phase generally consists of platinum nanoparticles dispersed on carbon black support particles, embedded within an ionomer matrix to enable proton conduction. An optimized and homogeneous distribution of the platinum catalyst over the carbon support is crucial to maximize the electrochemically active surface area, thereby enhancing reaction rates and improving fuel cell efficiency. Pt is used as the catalyst because it provides the highest performance in terms of current density for both the hydrogen oxidation reaction (HOR) at the anode and the oxygen reduction reaction (ORR) at the cathode. The microstructure of the catalyst layer must also provide a continuous network for electron conduction through the carbon support, proton conduction through the ionomer, and sufficient porosity to allow for reactant gas transport and product water removal. Any non-uniformity in catalyst dispersion or ionomer coverage can lead to localized transport limitations and reduced cell performance [20].

1.3.2.3 Membrane

The polymer electrolyte membrane is typically made of Nafion and represents the core component of the PEMFC, acting as a solid electrolyte that enables proton conduction from the anode to the cathode while maintaining electronic insulation and gas separation. Its high proton conductivity, combined with low gas permeability and good chemical and thermal stability, is essential to ensure the overall efficiency and durability of the fuel cell system.

Another material used is Aquivion which, unlike the more widely used Nafion, features a short-chain structure that provides specific operational advantages, including reduced need for humidification to maintain high ionic conductivity. This characteristic makes it particularly suitable for applications where humidity management is critical, such as in high-efficiency fuel cell systems (for example in automotive applications) [21].

The performance of PEMFCs is highly dependent on humidity levels, as demonstrated by numerous studies, because the ionic conductivity of the membrane is directly influenced by the water content in it. Water is produced at the catalyst layer during electrochemical reactions and subsequently diffuses through the cell structure. While it is essential to maintain adequate membrane hydration to ensure efficient proton transport, excessive water accumulation can lead to flooding within the gas diffusion layer (GDL), blocking its pores and preventing the proper flow of reactant gases. To achieve a suitable balance between hydration and water removal, the reactant gases (typically air and hydrogen) are often humidified before entering the cell. This approach helps to prevent excessive membrane drying while maintaining the optimal operating conditions required for stable and efficient fuel cell performance [22].

The most commonly used method for humidifying PEMFCs involves conditioning the gas streams before they enter the cell. Prior to entry, the gas is passed through a dedicated humidification section [23].

The findings in [24] showed that, at an ambient temperature of 30 °C, increasing the anode relative humidity from 0% to 100% led to an improvement of over 40% in the limiting current density. Moreover, at high current densities, higher anode humidity did not result in H_2O flooding.

In summary, optimal water content within the membrane is essential for maintaining proton conductivity and overall fuel cell efficiency. Current research focuses on improving humidity control efficiency, developing lightweight and compact humidification systems and ensuring real-time environmental adaptability [25].

1.3.3 Balance of plant

The Balance of Plant (BoP) of a PEMFC system encompasses all auxiliary components necessary to support the fuel cell stack, including the air supply and management system, the hydrogen supply loop, and the thermal management network, which together ensure optimal operating conditions, efficient reactant delivery, and safe temperature regulation.

1.3.3.1 Air loop

The air loop in a Proton Exchange Membrane Fuel Cell is a critical subsystem responsible for supplying oxygen to the cathode while ensuring optimal operating conditions. It typically includes a compressor, which pressurizes the incoming air to meet the stoichiometric and pressure requirements of the fuel cell. Following compression, the air often passes through a humidifier to increase its moisture content, as proper hydration of the membrane is essential for maintaining high ionic conductivity and overall cell performance. Additional components such as filters may be used to remove particulates and contaminants, while flow controllers ensure a uniform and controlled distribution of air across the cell stack [26].

In PEMFCs open-cathode and closed-cathode configurations differ mainly in how the cathode is supplied with oxygen and how heat and water are managed. Open-cathode fuel cells draw ambient air through the cathode, which both provides oxygen for the reaction and carries away heat (and water vapor) generated during operation. This design is simpler, lighter, and less expensive, since it does not require separate cooling hardware. However, its performance is more sensitive to ambient conditions (temperature, humidity) and airflow limitations.

In contrast, closed-cathode systems use a controlled oxygen supply (from air, or even a dedicated oxygen source) and typically employ dedicated cooling (air-cooled or liquid-cooled) plus active water management to prevent membrane flooding or drying. Closed-cathode designs tend to achieve higher power density, better thermal stability, and more consistent performance (especially in demanding applications) but at the cost of increased complexity, cost, and potentially system weight [27].

1.3.3.2 Hydrogen loop

In PEM fuel cells, the hydrogen loop refers to the way hydrogen is supplied, consumed, and managed within the anode compartment. Two common configurations are the dead-end system and the recirculation system.

In a dead-end system, the hydrogen feed to the anode is equal to the consumption rate, and the outlet is normally closed. This enables very high fuel utilization, but over time inert gases (such as N_2 or CO_2 from crossover) and water accumulate in the anode channels. To prevent hydrogen starvation and performance losses, the anode must be periodically purged by briefly opening a valve, releasing hydrogen alongside impurities and restoring fresh hydrogen supply.

In contrast, a recirculation system employs a loop in which unused hydrogen from the anode outlet is actively circulated back to the inlet, often with the help of a recirculation pump or ejector. This increases the hydrogen flow rate inside the stack, improving reactant distribution, humidity balance and water removal. The recirculation loop, however, remains in a transient state, as hydrogen is selectively consumed while other species accumulate, requiring periodic purges to maintain stable operation.

Overall, dead-end operation is simpler, while recirculation offers better stability, efficiency and durability [28].

1.3.3.3 Heat Generation and Cooling Methods

Thermal management is crucial for the safe and efficient operation of PEMFCs. Excessive heat generation can cause membrane drying, reduced performance, and accelerated degradation, while temperatures that are too low hinder reaction kinetics and may lead to flooding. Uneven temperature distribution affects reactants, current density, and water content in the membrane, thereby influencing PEMFC performance and water management [29].

During their operation, PEMFCs generate a notable quantity of heat, as shown in Figure 4:

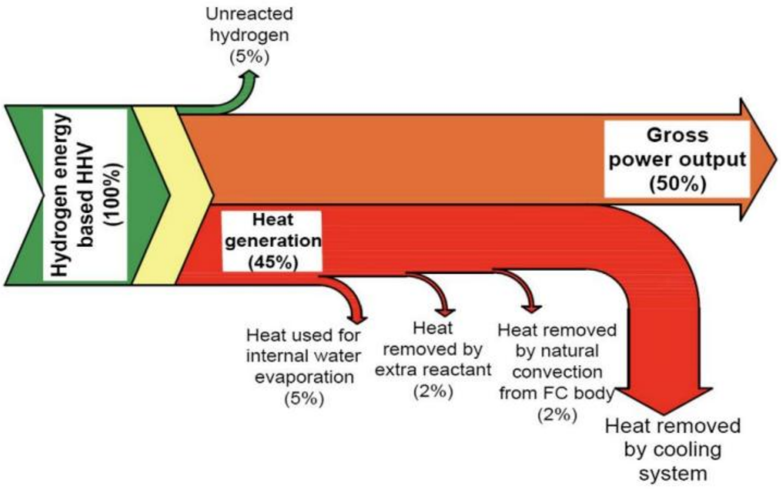

Figure 4: A typical energy flow diagram in a PEMFC [30]

The heat generated accounts for 45% of the total energy of hydrogen, which can cause the membrane electrode to dry out and lead to a deterioration in cell performance if the heat is not dissipated in time. Therefore, the cooling system is a very important part of fuel cells [31].

The most common cooling methods for PEMFCs are liquid cooling and air cooling, each with specific applications and associated advantages and disadvantages. Liquid cooling systems are widely used in high-power PEMFCs. Heat generated by the fuel cell stack is dissipated through a coolant circulating in dedicated cooling channels. However, liquid cooling systems introduce additional complexity and cost due to the need for pumps and pipes, while also presenting potential risks of leakage [32].

A typical configuration of a liquid cooling system for PEMFC is represented in Figure 5.

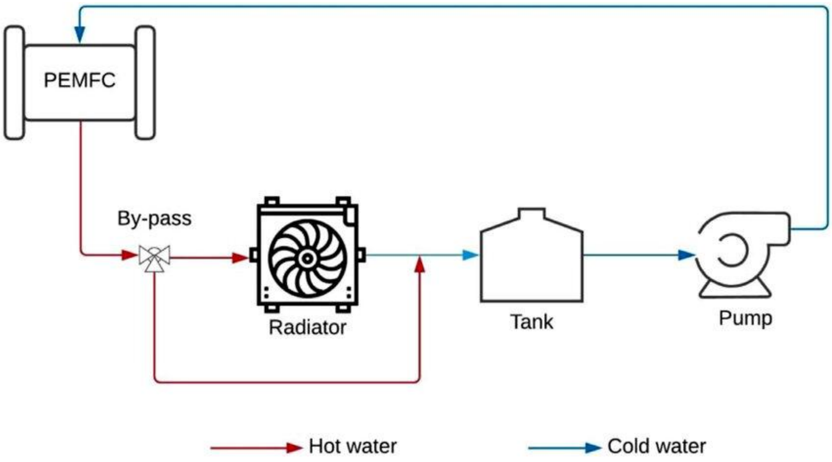

Figure 5: Typical cooling system of PEMFC using water [33]

Compared to water-cooled PEMFCs, air-cooled PEMFCs dissipate heat through air, avoiding the need for complex auxiliary components. This simplifies the overall system and reduces its weight, an advantage especially relevant for low-power devices, where heat dissipation demands are limited.

Figure 6 illustrates a typical diagram of a air-cooled PEMFC system: ambient air passes through an inlet air filter before entering the stack, while a fan ensures proper airflow and removal of exhaust gases. The figure also shows the supply valve (H_2 IN), through which hydrogen is introduced into the system, and the purge valve (H_2 OUT), used to expel it.

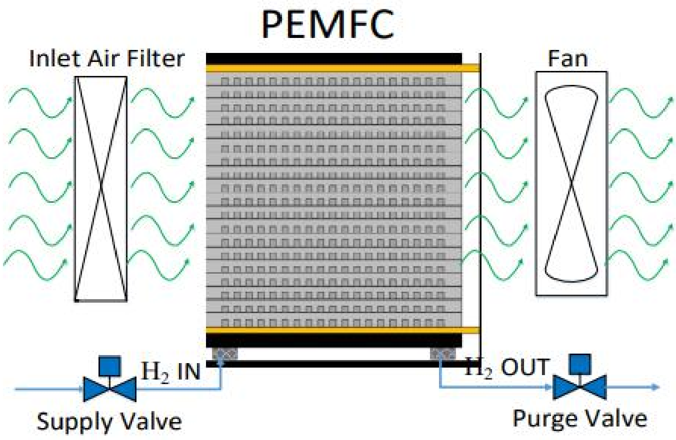

Figure 6: Diagram of a typical air-cooled PEMFC system [34]

Air-cooled PEMFCs can be categorized into three types based on their design: area air-cooled, edge air-cooled, and open-cathode. In the open-cathode configuration, the cathode channel is directly exposed to the ambient air, which both supplies the oxygen necessary for the cathode reaction and cools the stack via fan-induced airflow. This configuration (illustrated in Figure 7) combines a simple design with a wide power range, making it the most advanced and commonly adopted through the three types of air-cooled PEMFCs [35]. The challenge with this approach, however, is that it is challenging to balance the cell cooling, reactant supply and membrane hydration, specially when operating with a highly dynamic load profile under a range of environmental conditions. This can lead to poor cooling and thermal gradients within the fuel cell. The membrane can become over- or under-hydrated, which can result in low performance and slow transient load response. It can also enhance degradation mechanisms, leading to a reduced lifetime. If not used regularly, open cathode fuel cells must be conditioned to keep the membrane hydrated. This typically has to be done every month and must be considered in the maintenance program.

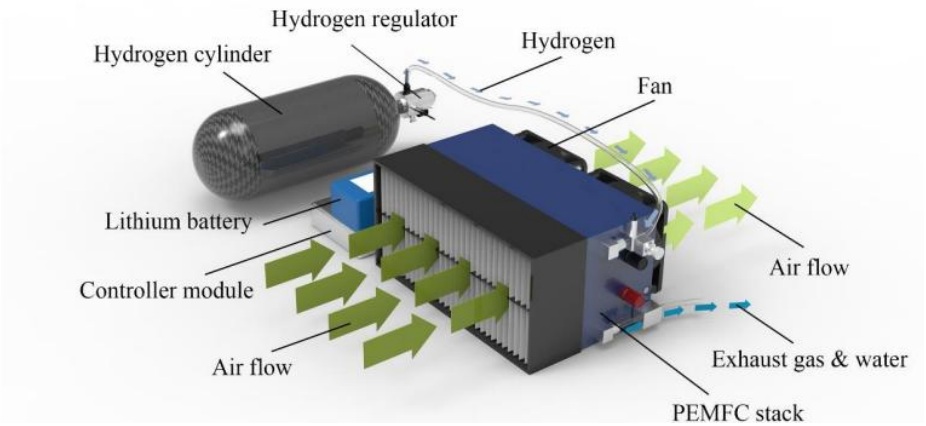

Figure 7: Typical configuration of an open-cathode PEMFC power system [1]

Liquid-cooled, closed-cathode fuel cells are more compact, but require a liquid coolant system, including a radiator and pump. This increases the complexity of the balance of plant, which impacts the overall system weight, size, and parasitic loads. As a result, these cells provide lower specific power and energy compared to open-cathode fuel cells for power ranges below 5 kW. However, they only need a fraction of the air consumed by air-cooled fuel cells (less than 1/15th). This results in better hydration control, the ability to filter air in dusty or sandy conditions, and a reduced sensitivity to air pressure and humidity changes. Additionally, using an anti-freeze coolant could allow operation in sub-zero temperatures [36].

1.4 PEM fuel cells for drone application

Power requirements for multi-rotor drones are generally more stringent compared to fixed-wing UAVs, and their load profiles tend to be more dynamic. As a result, fuel cell systems intended for these platforms must be designed with higher nominal power outputs and incorporate more sophisticated hybrid energy management strategies, often involving a larger battery component. This inevitably leads to an increase in the overall mass of the power system and introduces additional challenges. In a Fuel Cell Hybrid System (FCHS), the fuel cell serves as the primary energy source, while a secondary battery supplements the system (Figure 8).

Ideally, the fuel cell delivers continuous baseline power, whereas the battery enhances the system's responsiveness to rapid load fluctuations, supports peak power demands, provides redundancy, and acts as a buffer in emergency scenarios such as forced landings.

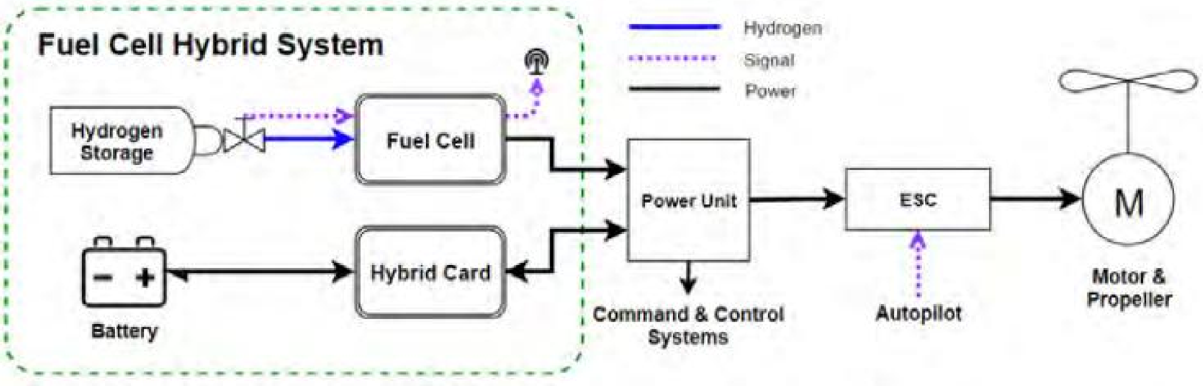

Figure 8: Simplified layout of a fuel cell hybrid system based multirotor propulsion system [4]

A typical FCHS consists of four main subsystems: the Fuel Cell Stack, the Balance of Plant, the Hybrid Battery, and the Hydrogen Storage. The BoP includes critical auxiliary components, including air and hydrogen feeding systems, control electronics, power management units, and thermal management system. The configuration of the fuel cell stack primarily determines the nominal power output, while the total available energy in the system depends on the capacities of both the hydrogen storage and the hybrid battery. When evaluating the performance of fuel cell systems relative to battery-only alternatives, it is crucial to consider the total mass of the complete power system.

For lightweight aerial platforms such as drones, PEMFCs are typically designed with simplified architectures that minimize auxiliary components and reduce system mass. In this context, the open cathode configuration is widely adopted, where ambient air provides both the oxidant and the cooling medium, eliminating the need for dedicated compressors and complex cooling systems. On the anode side, a dead-end configuration without hydrogen recirculation is commonly employed to maximize hydrogen utilization, with timed purging events used to remove accumulated inert gases and water. The cooling strategy relies entirely on natural or forced convection of air across the stack, making it efficient and lightweight. To further reduce weight while ensuring adequate electrical conductivity and corrosion resistance, bipolar plates are usually made of metallic materials (such as coated stainless steel or aluminum) or, in some cases, graphite composites.

Finally, these drone-oriented fuel cell systems typically operate without an external humidifier, relying instead on internal water management to maintain membrane hydration, which simplifies the balance of plant and enhances suitability for mobile, small-scale applications.

Table 2 presents a selection of commercially available fuel cell units developed by key industry players. These fuel cells are commonly integrated into existing commercial UAV platforms and demonstrator projects. It is important to note that fuel cell systems may operate at different voltage levels, and variations in hybrid system configurations can significantly influence their ability to manage dynamic loads.

Table 2: Commercially available fuel cell systems from some of the most relevant actors in the market [4], [37]

Vendor	System	Power [W]	Weight [kg]	Specific Power [W/kg]	Cooling Type
HES	A-1000	1000	1.800	556	Air
	A-1500	1500	2.800	536	Air
	A-2000	2000	4.380	457	Air
Intelligent Energy	650 FCPM	650	0.810	802	Air
	800 FCPM	800	0.930	860	Air
	2.4 FCPM	2400	3.250	738	Air
Ballard	FCair 600	600	1.800	333	Liquid
	FCair 1200	1200	4.000	300	Liquid
MMC	H1	1000	1.700	588	Air
Doosan	DP30	2600	3.400	764	Air
Spectronik	Protium-1000	1000	5.755	174	Air
	Protium-2000	2000	7.585	264	Air
	Protium-2500	2500	9.020	277	Air

Unlike land or sea vehicles that use hydrogen fuel cells, rotorcrafts (like drones) face a much more challenging operating environment. This is because, besides being influenced by factors like location and humidity, they also have to deal with significant changes in air pressure and temperature as altitude increases. These changes in temperature and air density are key elements that impact both the drone's power needs and its ability to maintain thermal balance.

For example, at 3,000 meters above sea level, the air pressure drops to about 0.7 bar. This lower pressure reduces the fuel cell's efficiency, which in turn affects how well the fuel-cell-powered drone can operate.

In the troposphere (the layer of the atmosphere that stretches from sea level up to 10 kilometers) the temperature changes with altitude, following the relationship given by the equation below:

$$T_{atm} = T_0 - 6.5 * \frac{h}{1000}$$

Exponential function models were used to fit temperature and density data curves, based on the reference atmospheric data. Efforts were made to determine the relationship between atmospheric pressure, temperature, and flight altitude h within the lower atmosphere:

$$P_{atm} = P_0 * \left(1 - \left(0.0065 * \frac{h}{T_0}\right)\right)^{5.2561}$$

Where P_0 = 101325 Pa, T_0 = 288.15 K and h is expressed in meters.

To guarantee the precise and effective collection of temperature data for rotorcraft unmanned aerial vehicles (UAVs), several factors need to be considered. These include choosing the right sensors, reducing environmental disturbances, improving response time, and using advanced signal processing methods. Implementing these strategies improves the accuracy and real-time temperature control of hydrogen-powered UAVs, ensuring they operate reliably and efficiently [38].

In [39], the influence of altitude on ambient pressure and temperature, and consequently on the efficiency of the PEMFC, is investigated.

Table 3: Ambient pressure and temperature at different altitudes [39]

Altitude [m]	Ambient pressure [Pa]	Ambient Temperature [K]
0	101325	288.15
1000	89874.11	281.65
2000	79494.39	275.15
3000	70107.44	268.65
4000	61638.93	262.15
5000	54018.46	255.65

Figure 9 illustrates how, as altitude increases (and consequently temperature and pressure decrease), both voltage and power density decrease at the same current density.

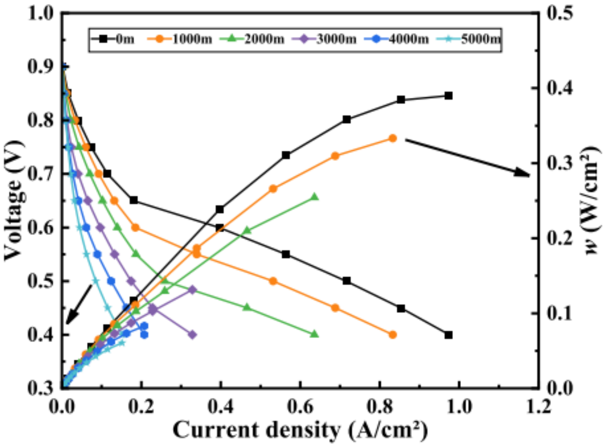

Figure 9: PEMFC polarization curves and power density curves at different altitudes [39]

As the altitude increases from 0 to 5000 meters, the ambient pressure decreases by 46.7% and the temperature by 11.3%. Specifically, for a current density of 0.2 A/cm^2, the cell voltage decreases from 0.65 V to approximately 0.4 V, corresponding to a 38.5% reduction, while the power density is halved, dropping from 0.14 W/cm^2 to 0.07 W/cm^2.

1.5 Hydrogen storage

Under constant power output conditions, the total take-off weight of a drone imposes strict limitations on the allowable mass of each onboard component, necessitating an optimized and well-balanced weight distribution among all hardware elements. For fuel cell-powered UAVs, flight endurance is primarily determined by the amount of hydrogen that can be stored and utilized during operation. Consequently, minimizing the weight of individual system components directly enables an increase in hydrogen storage capacity by allowing for a larger gas tank within the same total weight constraints. Thus, the lightweight design of the hydrogen fuel cell system hardware and the drone structure are important technical pathways to improve the flight time of drones.

1.5.1 Hydrogen Storage Technologies

While PEM fuel cells are the most promising stack type for multi-rotor applications, the hydrogen fuel introduces some challenges. It poses a safety risk, and available storage solutions have a certain mass and volumetric impact and can be challenging to integrate.

Currently, there are 3 main methods for hydrogen storage: compressed gas, liquid, and solid state [40].

1.5.1.1 Compressed gaseous hydrogen storage

The most commonly used hydrogen storage method for mobile devices is compressed gaseous hydrogen, and its containers are high-pressure gas cylinders. According to cylinder's material and structure, high-pressure gas cylinders can be divided into four types (Type I, II, III, and IV), which parameters are depicted in Table 4, while Figure 10 represents their structure.

Table 4: Technical parameters of the different types of high-pressure hydrogen cylinders [41]

Cylinder Types	Materials	Hydrogen Storage Pressure [MPa]	Mass Percent [%]	Volumetric Hydrogen Storage Density [g/L]	Service Life [years]
Type I	All metal	17.5-20	≈ 1	14.28-17.28	15
Type II	Metal liner with hoop wrapping	26.3-30	≈ 1.5	14.28-17.28	15
Type III	Metal liner with full composite wrapping	30-70	2.4-4.1	35-40	15-20
Type IV	Plastic liner with full composite wrapping	>70	2.5-5.7	38-40	15-20

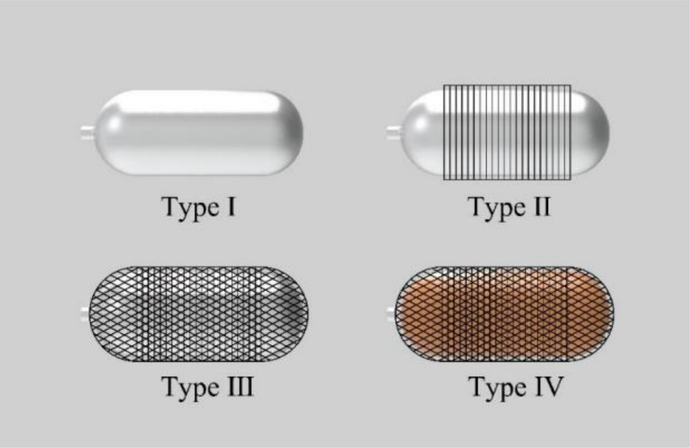

Figure 10: Structure of different types of gas cylinders [1]

The purpose of adopting the fiber-wrapped structure (Type II, III, and IV) is to apply a certain precompression to the casing through the tension of the fiber, thereby improving the load capacity of the hydrogen cylinder. Since the density of the lightweight fiber is significantly lower than that of the casing, the weight of a fiber-wrapped gas cylinder is considerably lower compared to that of a fully metal gas cylinder with the same hydrogen storage pressure [42].

1.5.1.2 Liquid hydrogen storage

The hydrogen must be cooled to a cryogenic temperature and stored in special containers in liquid form. Thanks to its high density of up to 70.8 g/L, liquid state contains much more hydrogen mass than the gaseous form for the same storage volume, allowing a significantly higher onboard fuel amount and therefore greatly extending the flight range and endurance of hydrogen fuel cell drones.

Despite the advantages of high energy density and high compression ratio at low operating temperatures, the liquid hydrogen storage method also presents significant limitations, especially regarding the number of hydrogen reuse cycles, limited by material aging and structural fatigue.

Moreover, liquid hydrogen requires extremely low temperatures (20-30 K) to remain in liquid form, which means that storage equipment must have high insulation capacity to prevent rapid evaporation due to thermal losses. This results in high construction costs for liquid hydrogen cylinders, and over time, the performance of the insulating materials degrades, affecting cooling efficiency and reducing the effective storage time [43].

1.5.1.3 Solid-state hydrogen storage

There are two methods for solid-state hydrogen storage: the first involves the physical combination of hydrogen with storage materials in the form of molecules, while the second involves the chemical combination of hydrogen with other components through ionic or covalent bonds to form hydrides [44].

The benefits of chemical storage solutions can be safe low-pressure storage, easy to handle and transport, and low volumetric density. However, some general challenges are low gravimetric density, slow reaction kinetics, low gas supply, high cost, and reusability [45].

Commonly used materials for physical hydrogen storage include mainly carbon-based, silicon-based, and metallic materials. There are also other porous materials with a large specific surface area, which combine with hydrogen molecules via van der Waals forces [46].

Materials for chemical hydrogen storage mainly include metal alloys and coordination hydrides.

Table 5 summarizes and compares the main characteristics of several different hydrogen storage methods. Metal hydrides can be volume efficient, but they perform poorly in terms of mass. Liquid hydrogen has the best energy to volume and mass characteristics. Compressed hydrogen performs better in terms of mass efficiency than volumetric density.

Table 5: Comparison of direct hydrogen storage technologies [7], [23]*

Storage System	**Mass Storage Efficiency**	**Storage Density**	**Specific Energy**	**Energy Density**
	$\% \frac{H_2\,mass}{storage\,mass}$	$\frac{H_2 mass\,[g]}{Storage\ vol.\,[L]}$	$\frac{Wh}{kg}$	$\frac{Wh}{L}$
Compressed H_2 @30 MPa	3.10	14	1200	550
Compressed H_2 @70 MPa	4.80	33	1900	1300
Liquid H_2, Cryogenic	14.20	43	5570	1680
Liquid H_2, Cryo-compressed	7.38	45	2460	1510
Metal Hydride, Conservative	0.65	28	260	1120
Metal Hydride, Optimistic	2.00	85	800	3400

**Note that the mass and the volume of the entire storage system (pressure vessel, valve, tubing and regulator) are taken into account in these data*

1.6 Energy Management

Although hydrogen fuel cells provide high energy density, zero emissions, and low noise, their limited ability to respond quickly to rapid changes in power demand makes them unsuitable for applications requiring high instantaneous power. In addition, an external power source is required for start-up. They are, however, well suited for missions involving steady, long-duration energy supply [47].

Lithium batteries, by contrast, can deliver high instantaneous power but have limited energy capacity. Therefore, combining hydrogen fuel cells with lithium batteries in a hybrid power configuration represents an optimal solution, effectively overcoming the inherent limitations of fuel cells [48].

Active energy management in a hybrid fuel cell-battery system allows independent control of the power delivered by the fuel cell and the battery. The fuel cell can provide a steady baseline at its optimal efficiency, while the battery handles peak or transient loads. Compared to passive management (where the fuel cell and battery respond according to their polarization curves to the load), this approach improves overall efficiency, reduces battery stress, and ensures the fuel cell operates safely, efficiently and at high power rate.

A typical hybrid fuel cell-battery system topology is shown in Figure 11.

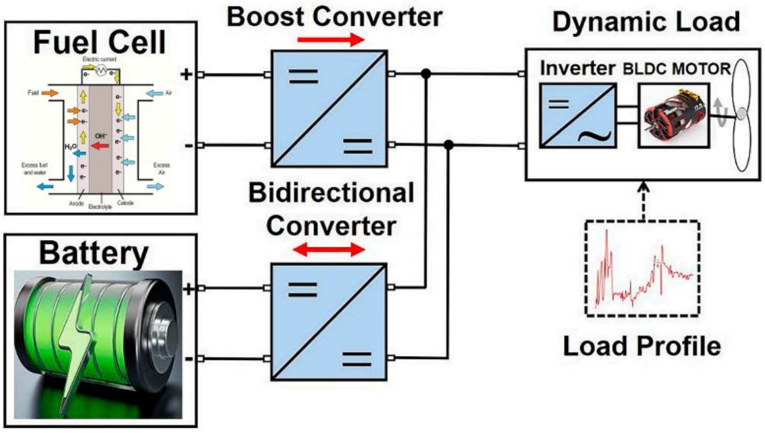

Figure 11: Hybrid power supply system topology [2]

The fuel cell is connected in parallel with the lithium battery through a DC/DC boost converter, and then connected to the dynamic load. Additionally, to effectively manage the charge and discharge current of the battery, a bidirectional DC/DC converter has been integrated between the battery and the DC bus.

The control system distributes the energy between the fuel cell and the lithium battery by adjusting the parameters of the DC/DC converters.

Typically, there are three possible operating conditions for multi-rotor drones:

- Take-off or rapid ascent: the power required by the drone might exceed the power supplied by the fuel cell.
- Cruise: the power required by the drone is almost equal to the power supplied by the fuel cell.
- Landing: the power required by the drone is less than the power supplied by the fuel cell.

When the control system recognizes the specific flight condition, it adjusts the battery charge or discharge [49].

Figure 12 represents the power sharing control strategy:

- If the required power is less than the power supplied by the fuel cell, only the fuel cell is used and, if the State Of Charge of the battery is less than 100%, the fuel cell recharges the battery.

- If the power required by the drone exceeds the power supplied by the fuel cell, the battery is also used. In this case, it discharges to provide the additional power needed.

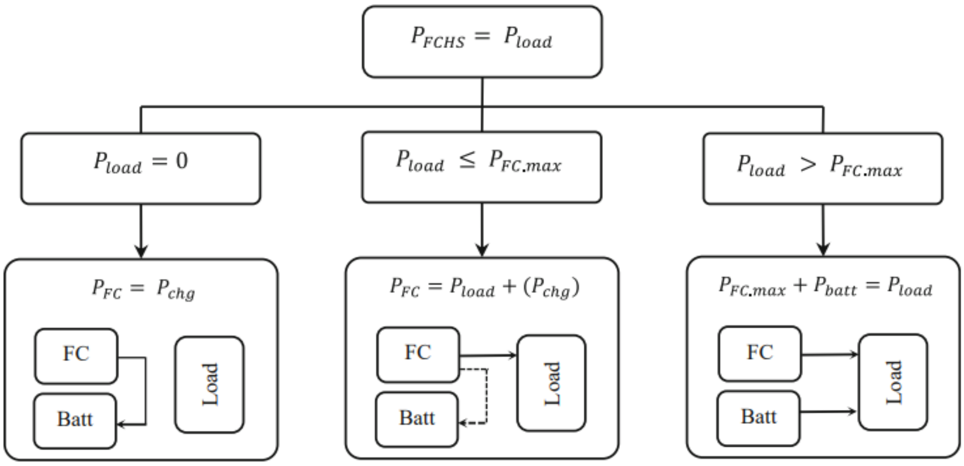

Figure 12: The three main states of the hybrid system [4]

1.6.1 Energy management strategy (EMS)

The energy management strategy should be conceived to optimize the power allocation respecting the sources characteristics and preserving their lifetimes.

EMS is responsible for determining the optimal allocation and use of hydrogen fuel cells and lithium batteries according to the specific requirements of a mission. Implementing an effective strategy can significantly reduce unnecessary hydrogen consumption, thereby enhancing the overall endurance and flight performance of the drone [50].

In the literature, different topologies are proposed for integrating an energy storage system into the fuel cell-based power supply system. The selection of an appropriate architecture for the drone platform is crucial in optimizing overall system efficiency, weight, and cost. A passive topology, where power sources are directly linked to the DC bus, offers notable advantages in terms of simplicity and high efficiency. This approach minimizes the complexity of the system, allowing for more straightforward integration while maintaining efficient power transfer across the platform. However, this topology lacks power controllability, thus resulting in oversized fuel cell stack and reduced power density.

In [2], three energy management strategies are compared:

- Rule-based strategy
- Frequency separation rule-based strategy
- Equivalent Consumption Minimization Strategy

They are outlined below.

1.6.1.1 Rule-based strategy (RB-EMS)

The energy management strategy (EMS) employed in the Intelligent Energy fuel cell power module is based on a set of if-then rules. As depicted in Figure 13, the fuel cell consistently provides a rated power output, corresponding to the required power for hovering (800 W), regardless of variations in load power. The battery compensates for any additional power requirements, particularly during peak demands (black areas), or is charged when the fuel cell's rated power exceeds the load power (blue areas). However, this straightforward approach presents several limitations. The hovering power is not constant, as it is influenced by factors such as payload, mission type, and environmental conditions. Consequently, the rated power of the fuel cell does not always align with the actual hovering power, causing the system to operate outside of its optimal performance range. This misalignment may also result in the battery being called upon to supply higher currents to meet the power demands, leading to accelerated wear and reduced lifespan for both power sources. Furthermore, the drone is designed to perform various mission types, not solely hovering-based operations, necessitating an adaptive EMS. It is important to note that the implementation of the RB-EMS assumes an ideal scenario in which the nominal power coincides with the hovering power (an assumption that does not hold true in all cases).

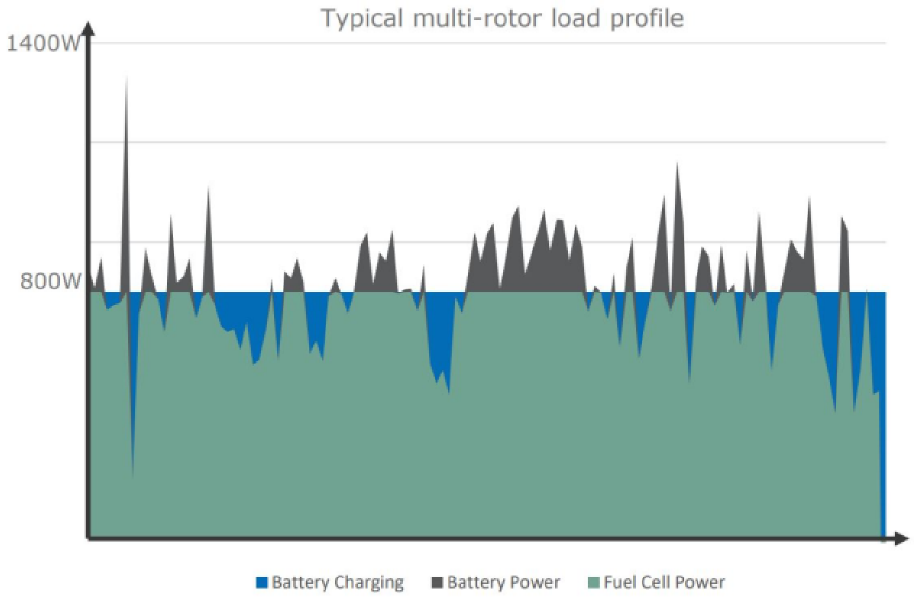

Figure 13: Intelligent Energy implemented EMS [2]

1.6.1.2 Frequency separation rule-based strategy (FSRB-EMS)

This method represents an enhanced version of the frequency separation strategy, where power distribution is based on the frequency decomposition of the load power, with the fuel cell handling only low-frequency components. This approach improves the fuel cell's lifespan by reducing exposure to power fluctuations. However, the lifetime of the energy storage system remains unaddressed. Specifically, the battery's state of charge (SOC) and charge/discharge current are not monitored, leading to high stress on the battery and a consequent reduction in performance. Additionally, safety measures require maintaining a minimum battery energy threshold during flight to ensure sufficient power for emergency landings in the event of fuel cell or DC/DC converter failure. Although the fuel cell's power profile remains smooth with this strategy, it cannot guarantee optimal operational efficiency. To ensure effective performance, the fuel cell must operate within the manufacturer's specified minimum and maximum power limits, as prolonged operation outside these limits can lead to issues like clogging and inadequate cooling.

1.6.1.3 Equivalent Consumption Minimization Strategy (ECMS)

The main objective of the ECMS is to minimize hydrogen consumption. However, due to the rapid and significant load power fluctuations typical of multirotor UAVs, PEMFCs (limited by their inherent structural characteristics) are not well-suited to efficiently meet these fast-changing power demands. To compensate for this, lithium batteries are used to either supply or absorb power on the DC bus, which can lead to substantial fluctuations in the battery's state of charge (SOC). Specifically, when the SOC is high, even without the need for charging, the PEMFC may struggle to decrease its output power quickly due to its structural limitations, which could result in unnecessary charging of the lithium batteries. In such cases, DC converters may cause significant energy losses, increasing hydrogen consumption and negatively impacting the SOC management of the lithium batteries. To address these issues, further optimization of the power distribution between the PEMFC and lithium batteries is required. By fine-tuning the lithium battery output power, energy losses during power transfer can be minimized, leading to more efficient energy distribution, better SOC management, and a reduction in unnecessary hydrogen consumption. This optimization enhances both the economic and operational efficiency of the hybrid power system.

The study presented in [2] demonstrated that the ECMS effectively optimizes the distribution of load power between the two power sources, resulting in a 3% improvement in hydrogen efficiency. This enhanced fuel economy directly contributes to an increase in drone autonomy.

The study in [51] presents an improved ECMS for hybrid hydrogen fuel systems in multirotor UAVs. By addressing the limitations of PEMFCs under dynamic load conditions, the proposed ECMS optimizes energy management through effective coordination between PEMFCs and lithium batteries. This strategy considers charging-related losses and introduces penalty factors to balance the SOC of lithium batteries, thereby reducing unnecessary hydrogen consumption and improving overall system efficiency. Simulation results show that the optimized ECMS outperforms the standard ECMS in terms of efficiency and hydrogen consumption. The proposed strategy significantly reduces hydrogen consumption, enhances system efficiency, and effectively maintains the SOC of lithium batteries under various initial conditions. These improvements ensure reliable and efficient energy management, supporting extended flight durations and operational flexibility for multi-rotor UAVs. The findings demonstrate the practical applicability of the optimized ECMS in addressing real-world challenges, such as frequent power fluctuations and energy losses in hybrid systems.

1.7 Development and Application of Hydrogen Fuel Cell Multi-Rotor Drones

Research on the application of fuel cells to multi-rotor drones has only begun in recent years, particularly since 2015.

Figure 14: Early hydrogen fuel cell multi-rotor drones: (a) H2Quad from EnergyOr; (b) fuel cell drone from Intelligent Energy; (c) Ranger from Zhongyu Power; (d) HYDrone-1800 from MMC [1]

Below are some fuel cell-powered multi-rotor drones along with their respective parameters:

Table 6: Hydrogen fuel cell multi-rotor drones [1], [52], [53]

Name	Manufacturer	Year	FC System Power [W]	N° Rotors	Hydrogen Storage Method	Flight Time [min]	Weight of the Drone [kg]
-	Intelligent Energy	2015	650	4	Compressed gaseous	60	4.3 (with a 1.5L cylinder)
Hycopter1	HES	2015	1500	4	Compressed gaseous	90-240	5.2
HYDrone-1550	MMC	2015	1800	6	Compressed gaseous	150	17
HYDrone-1800	MMC	2016	1800	6	Compressed gaseous	270	20
Sensus4	ISS Aerospace	2018	800	4	Compressed gaseous	90@1.5kg 30@6kg	
Sensus6	ISS Aerospace	2019	2400	6	Compressed gaseous	120@8kg 25@20kg	
Phoenix	Spectronik	2019	2000	6	Compressed gaseous	90	19 (with a 9L cylinder)
BG-200	Nordic Unmanned	2020	2000	8	Compressed gaseous	99	20.7 (with a 7.2L cylinder)
Hydrocopter-04	Hydrogen Craft	2020	3400	6	Compressed gaseous	180 150@1kg 96@5kg	20 (with a 12L cylinder)
DT30X	DMI	2023	2700	6	Compressed gaseous	150	21 (with a 10.8L cylinder)

1.7.1 Intelligent Energy

The IE-Soar series of fuel cells developed by Intelligent Energy for unmanned aerial vehicles currently includes some of the lightest fuel cell modules available globally. The company has achieved a high stack power density exceeding 800 W/kg, exemplified by the IE-Soar 650 W, 800 W, and 2400 W models. These modules enable greater allocation of weight and space to auxiliary systems, thereby contributing to an extended flight endurance of the drone.

In particular, the AC64 650W fuel cell module is a compact and lightweight system can be integrated into drones to increase their range. In 2015, IE developed a drone prototype (Figure 15) and made it fly for 60 minutes with a 1.5L compressed hydrogen tank. Table 7 and Table 8 summarize respectively the specifications of AC64 650W fuel cell module and of the drone system, which also provides an emergency battery with a capacity of 1000 mAh, designed to ensure the safety of the UAV's flight. Weighing only 0.20 kg and with compact dimensions (140×30×20 mm), this battery has been developed to keep the overall weight of the drone as low as possible, providing an emergency flight time of about 2 minutes [52].

Figure 15: Intelligent Energy's fuel cell prototype system mounted in UAV

Table 7: Specifications of AC64 650W fuel cell module for UAV

Parameter	Data
Maximum continuous power [W]	650
Maximum peak power [W]	1000
Output voltage - custom configurable [V]	14.8–25.2
Energy capacity of 1.5 dm^3 bottle (30 MPa) [Wh]	600
Energy density of FC module (+1.5 dm^3 bottle) [Wh/kg]	300
Dimensions of fuel cell module [mm]	196×84×155
Dimensions of 1.5 dm^3 H_2 bottle [mm]	Ø 116×238
H_2 bottle weight [g]	1010
Fuel Cell module weight [kg]	0.950
Total Fuel Cell module weight (+1.5 dm^3 bottle) [kg]	1.960

Table 8: Approximated specifications of UAV system with fuel cell module

Parameter	Data
Maximum payload (for non-weight reduced platform) [kg]	0.50
Maximum flight time with 500g payload [minutes]	60
Operating temperature [°C]	5-35
Maximum altitude [m]	3000
System lifetime [hours]	1000

1.7.2 Hycopter1

Hycopter1 represents the next generation of the Hycopter platform, which initially served as a prototype featuring integrated hydrogen storage within transparent cylinders that were structurally embedded into the UAV's frame. This drone is powered by an ultra-lightweight fuel cell stack, supplied by a compressed hydrogen bottle operating at 30 MPa. Both the fuel cell stack and the hydrogen storage system (equipped with a lightweight pressure regulator) are housed within the UAV's airframe, contributing to a compact and efficient power integration.

Figure 16 shows Hycopter1 in flight, while Table 9 summarizes its specifications.

Figure 16: Hycopter1 [54]

Table 9: Specifications of Hycopter1

Parameter	Data
MTOW [kg]	5.2
Energy supply system	A-200 PEM 200W - HES fuel cell
Hydrogen storage	Compressed, 30 MPa
Engine	Electric
Endurance	1.5 - 4 h flight (with 1kg payload)

1.7.3 MMC (Micro Multi Copter)

The Chinese company MMC, based in Shenzhen, manufactures drones used in various industrial sectors, including agriculture, delivery, power line inspection, oil inspection, forestry firefighting, mapping, and public security surveillance.

The HyDrone 1550 (Figure 17), developed by MMC, is a hydrogen-powered drone with six propellers. Its lightweight carbon fiber airframe allows for extended flight times (up to 2.5 hours) and a maximum payload of 5 kg (MTOW 22 kg). The hydrogen fuel is stored in a 9 dm^3 pressure bottle that powers the fuel cell stack. With the ability for fast refueling, and a rainproof and dustproof design, this UAV is suitable for use in various environments.

Figure 17: Hydrogen powered HyDrone 1550 manufactured by MMC [52]

MMC's latest UAV model, the HyDrone-1800 (Figure 14d), represents an evolution of the earlier HyDrone-1550 and features a carbon fiber airframe as his predecessor. According to the manufacturer, the structural design is described as "almost indestructible" and has been developed specifically to withstand operation in highly demanding and adverse environmental conditions.

1.7.4 Meta Vista - liquid hydrogen

In order to extend the endurance of fuel cell-powered multi-rotor drones, current research efforts focus on increasing the onboard hydrogen capacity by modifying storage approaches. For instance, in 2019, Meta Vista Inc. (Seoul, South Korea) equipped a drone with a 6 L liquid hydrogen tank in combination with Intelligent Energy's 800 W IE-Soar fuel cell. This configuration, illustrated in Figure 18, raised the energy density of the power system to 1865 Wh/kg and enabled flight durations exceeding 12 hours [55].

Figure 18: The liquid hydrogen storage fuel cell drone from Meta Vista [55]

Nevertheless, due to the high costs of liquid hydrogen, the complexity of its storage, and the immaturity of the related technologies, this solution has not been widely adopted by other drone manufacturers. Consequently, gaseous hydrogen storage remains the predominant method used in multi-rotor drones.

1.8 Purpose of the thesis

The primary objective of this thesis is to conduct a comprehensive experimental investigation of a hybrid fuel cell/battery system applied to an unmanned aerial vehicle (UAV).

An investigation of this kind is of significant importance due to the growing demand for drones with extended flight endurance and enhanced operational capabilities. Traditional battery-powered drones are often limited by energy density, which constrains flight time and payload capacity. Integrating a fuel cell with a battery offers the potential to overcome these limitations by providing higher energy density and more efficient power management. Experimental studies are essential to evaluate the practical performance of such hybrid systems under real operating conditions, identify potential technical challenges, and provide empirical data that can support the development of more reliable and capable UAV platforms. By addressing these aspects, the study contributes to advancing both the technological maturity and the practical applicability of fuel cell-based hybrid propulsion systems for aerial vehicles.

The study is organized into two main phases: a laboratory-based experimental campaign and a flight test. The laboratory phase focuses on characterizing the electrical and operational performance of the hybrid system under controlled conditions, analyzing key parameters such as voltage, current, power distribution, hydrogen flow, and overall system efficiency. The subsequent flight test aim to validate these findings in real operational scenarios, evaluating the impact of the hybrid configuration on drone endurance and overall flight performance.

In addition, other objectives include assessing the stability and responsiveness of the system under varying electrical loads, analyzing its efficiency in both laboratory and flight conditions, characterizing the interactions between the fuel cell and the battery during different operational phases.

This approach provides a detailed understanding of the hybrid system's behaviour, highlighting its potential advantages and limitations in practical UAV applications.

2 Experimental setup description

The initial experimental activities were carried out using a dedicated test bench set up at the laboratories of Environment Park in Turin, specifically in HysyLab.

This facility provided the necessary infrastructure and safety conditions for testing the hybrid hydrogen-battery powered system, including access to certified hydrogen supply, ventilation systems, and instrumentation suited for electrical and thermal measurements.

2.1 Test bench architecture

The test bench main components are two electronic loads and the hydrogen subsystem. Furthermore, a temperature sensor was installed near the fuel cell stack to monitor thermal behaviour and ensure safe operating conditions. This configuration allows for a comprehensive analysis of system performance, energy efficiency, and dynamic response under both steady-state and time-varying loads.

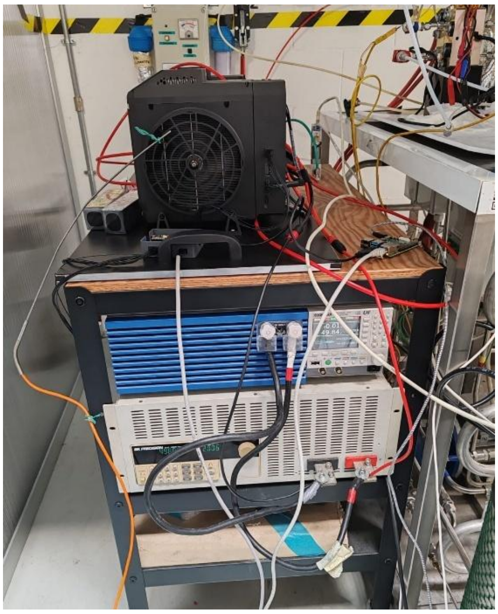

Figure 19: Test bench

2.1.1 Electronic loads

The electronic load is a programmable device designed to simulate the behaviour of a real electrical load in a controlled and repeatable manner. In the test bench setup, it plays a fundamental role in replicating the power demand that the fuel cell-battery hybrid system would experience during real-world operations.

The main programmable electronic load used in the tests is the BK-precision 8520, which is capable of providing up to 2400 W of power. It allows precise control over the load profile by enabling different operating modes, including constant current (CC), constant voltage (CV), constant power (CP) [56].

Figure 20: BK precision 8520 electronic load

This electronic load is a versatile instrument designed for the testing and characterization of various DC power sources. Thanks to its broad operating range (supporting voltages up to 120 V and currents up to 240 A) combined with multiple control modes and high measurement precision, it is particularly well-suited for evaluating devices such as DC power supplies, DC-DC converters, batteries, fuel cells, and photovoltaic systems.

The safety of the system is guaranteed by Over-Current, Over-Voltage, Over-Power and Over-Temperature protections.

To handle power peaks exceeding 2400 W, a second electronic load was connected in parallel. This configuration provided both flexibility and safety, allowing seamless handling of dynamic or peak load phases. The model used for this purpose is the Kikusui PLZ1205W, which has a rated power of 1200 W and supports voltage levels of up to 150 V and currents up to 240 A. The detailed operation is described in section 3.3.

Figure 21: Kikusui PLZ1205W electronic load [57]

2.1.2 Hydrogen mass flow meter/controller

The hydrogen mass flow controller used in the test bench is the Bronkhorst EL-FLOW F-201AV.

This model incorporates a thermal sensor technology with digital temperature and pressure compensation, allowing for accurate and stable readings over time, even under variable operating conditions. It is also equipped with digital electronics featuring Multi-Gas and Multi-Range capabilities, which enable the device to be configured and adapted to different gases and flow ranges without requiring hardware modifications. With a measurement range extending up to 100 NL/min, the F-201AV offers excellent precision, versatility, and fast response time, making it an ideal solution for continuous hydrogen flow monitoring in the experimental test bench [58].

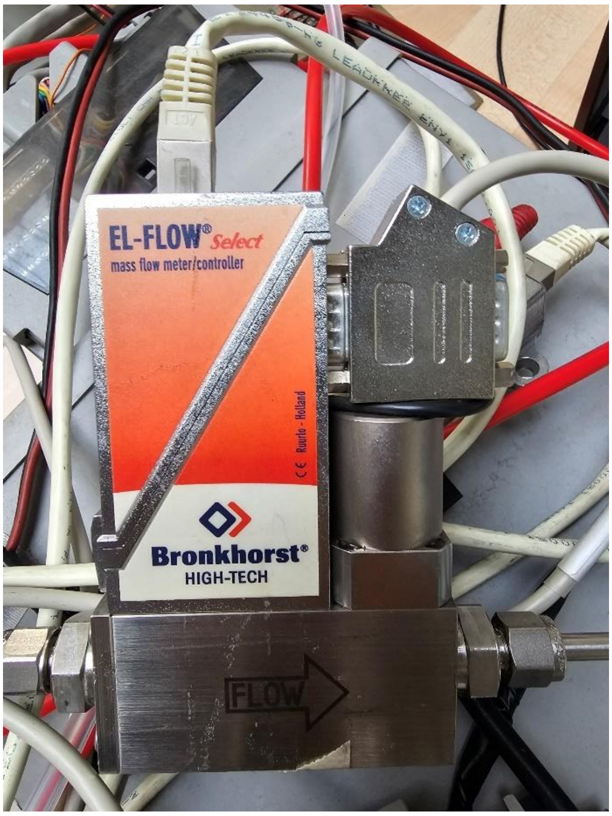

Figure 22: Bronkhorst EL-FLOW F-201AV mass flow meter

2.2 Power Sources

The power sources tested in the previously described test bench are the IE-SOAR 2.4 kW fuel cell and the Li-Po battery, which are detailed in this section.

2.2.1 IE-SOAR 2.4 kW Fuel cell

The IE-SOAR 2.4 kW is a lightweight, commercial air-cooled hydrogen fuel cell power module designed by Intelligent Energy and produced primarily for fixed-wing, rotary-wing, and VTOL UAV applications, when battery-based systems limit flight duration [59].

A Power Control Module (PCM) that controls the power sharing between the fuel cell and the battery is integrated.

The fuel cell system is composed of two integrated power modules, referred to as SPM1 and SPM2 (Smart Power Modules). Each module operates as an independent fuel cell stack with its own control and power electronics, and together they form a redundant and modular system architecture.

Figure 23: IE-SOAR 2.4 kW, SPM1 and SPM2

The combined output of SPM1 and SPM2 delivers a total continuous power of 2.4 kW, with each module contributing approximately half of the total output. This configuration enhances system reliability, as the two modules can dynamically share the load, and in case of a fault, one module can be disengaged while the other continues to operate.

Such a dual-stack design is particularly advantageous for aerospace applications, as it provides both operational flexibility and fault tolerance, while maintaining a compact and lightweight form factor.

The main characteristics of the fuel cell system are reported in Table 10:

Table 10: Characteristics of IE-SOAR 2.4 kW [60]

Parameter	Value
Through life power [W]	2400
Peak system power [W]	Up to 8000
Output voltage (DC/DC regulated) [V]	Configurable between 50 and 70
Dimensions [mm]	128 x 442 x 233
Mass [g]	4800
Operating air Temperature [°C]	Between -5 and 40
Maximum altitude [m]	3000

2.2.2 Battery

The experimental setup utilizes a 12-series (12S) Lithium Polymer (Li-Po) battery pack, consisting of twelve cells connected in series. Each cell has a nominal voltage of 3.7 V, resulting in an overall nominal pack voltage of 44.4 V. When fully charged, the battery pack reaches a maximum voltage of 50.4 V (4.2 V per cell), while the recommended minimum discharge voltage is approximately 50-60% of the nominal voltage. Maintaining the battery within this voltage range is crucial both for safe operation and for ensuring the longevity of the cells [61].

In the hybrid power system, the battery plays a crucial role in supporting the dynamic behaviour of the fuel cell. While the fuel cell provides the primary continuous power supply, it is inherently limited in its ability to respond rapidly to sudden changes in load demand. For this reason, the battery is integrated as a complementary energy source, designed to compensate for power peaks and fast transients that the fuel cell alone cannot address effectively.

During phases of rapid power increase (such as take-off, acceleration, or abrupt load shifts) the battery discharges to supply the additional required power. Conversely, during periods of low power demand or when the fuel cell output exceeds the load, the battery can be recharged. This bidirectional power flow allows the system to maintain stability, continuity, and responsiveness, improving both the efficiency and lifespan of the fuel cell by avoiding excessive stress and oversizing.

The integration of the battery therefore enables a more flexible and reliable power delivery architecture, especially under real-world operating conditions where the power demand is highly variable, such as in UAV flight profiles.

2.3 Control interface

The objective of the control system is to monitor, in real-time, the main electrical and physical parameters during the experimental tests carried out on the fuel cell system. Specifically, data acquisition is aimed at analyzing system performance, computing efficiency, and evaluating the dynamic response of the system under realistic operating scenarios.

2.3.1 LabVIEW-Based Data Acquisition and Control

The data acquisition system was developed using the software LabVIEW (Laboratory Virtual Instrument Engineering Workbench), a graphical programming environment developed by National Instruments. LabVIEW is particularly well-suited for experimental setups involving real-time monitoring, instrumentation control, and data logging, thanks to its intuitive block-diagram approach, fully integrated user-interfaces and native compatibility with hardware devices [62].

In this application, LabVIEW performs several key functions. First, it reads a power reference profile from an Excel file, which defines the desired power levels to be applied to the electronic loads during the test. These values are used to dynamically control the programmable DC loads, ensuring the system operates according to the predefined test scenario.

Simultaneously, LabVIEW continuously acquires signals from multiple devices connected to the fuel cell system. These include voltage, current and power measurements from the fuel cell, as well as physical quantities such as hydrogen mass flow rate and temperature.

The acquired data are displayed in real time on the LabVIEW front panel and are also saved to an output Excel file for post-processing and analysis. This allows precise tracking of the system's behaviour during the test, including performance evaluation and efficiency computation.

2.3.1.1 Front Panel

Figure 24 shows the front panel of the LabVIEW Virtual Instrument (VI) developed for the experimental tests. The interface is organized into different sections to facilitate both control and monitoring during the operation of the fuel cell system.

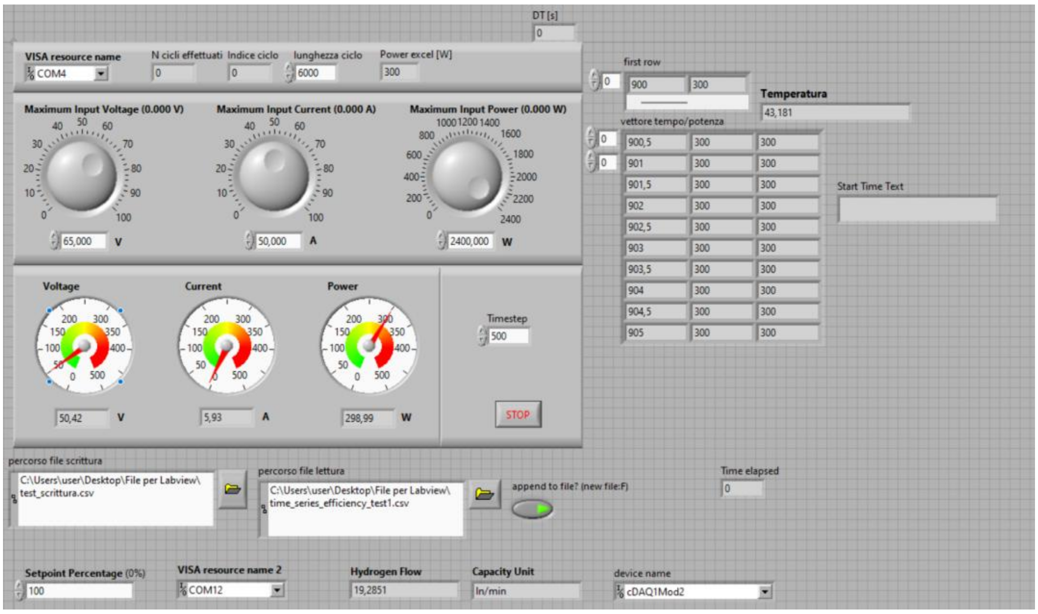

DT [s]
0

VISA resource name
COM4

N cicli effettuati
0

Indice ciclo
0

lunghezza ciclo
6000

Power excel [W]
300

Maximum Input Voltage (0.000 V)
65,000 V

Maximum Input Current (0.000 A)
50,000 A

Maximum Input Power (0.000 W)
2400,000 W

Voltage
50,42 V

Current
5,93 A

Power
298,99 W

Timestep
500

first row
0

900	300

Temperatura
43,181

vettore tempo/potenza
0
0

900,5	300	300
901	300	300
901,5	300	300
902	300	300
902,5	300	300
903	300	300
903,5	300	300
904	300	300
904,5	300	300
905	300	300

Start Time Text

percorso file scrittura
C:\Users\user\Desktop\File per Labview\test_scrittura.csv

percorso file lettura
C:\Users\user\Desktop\File per Labview\time_series_efficiency_test1.csv

append to file? (new file:F)

Time elapsed
0

Setpoint Percentage (0%)
100

VISA resource name 2
COM12

Hydrogen Flow
19,2851

Capacity Unit
ln/min

device name
cDAQ1Mod2

Figure 24: LabVIEW VI Front Panel

In the upper part, the user can set the maximum allowable values of voltage, current, and power to ensure safe operation of the electronic loads. The middle section displays real-time indicators of the main electrical quantities (voltage, current, and power) measured at the fuel cell output. These values are shown both numerically and through analog-style gauges, allowing an immediate visualization of the system's performance.

On the right-hand side, the panel displays the power profile vector, read from the Excel input file, which defines the power steps or dynamic variations applied during the test. The temperature sensor reading is also displayed in real time.

The bottom part of the panel includes the file path selectors, where the input Excel file (containing the desired power profile) and the output file (used to write acquired data) are specified. Additional indicators show the hydrogen flow rate, the elapsed time, and the connection status with the DAQ modules and instruments.

This layout allows the operator to easily control the test sequence, monitor the fuel cell behaviour and ensure proper data acquisition for subsequent analysis.

2.3.1.2 Block Diagram

The complete block diagram of the developed VI is shown in Figure 25. The diagram integrates the different functions required for the test management, including signal and data acquisition and control of the applied load profile.

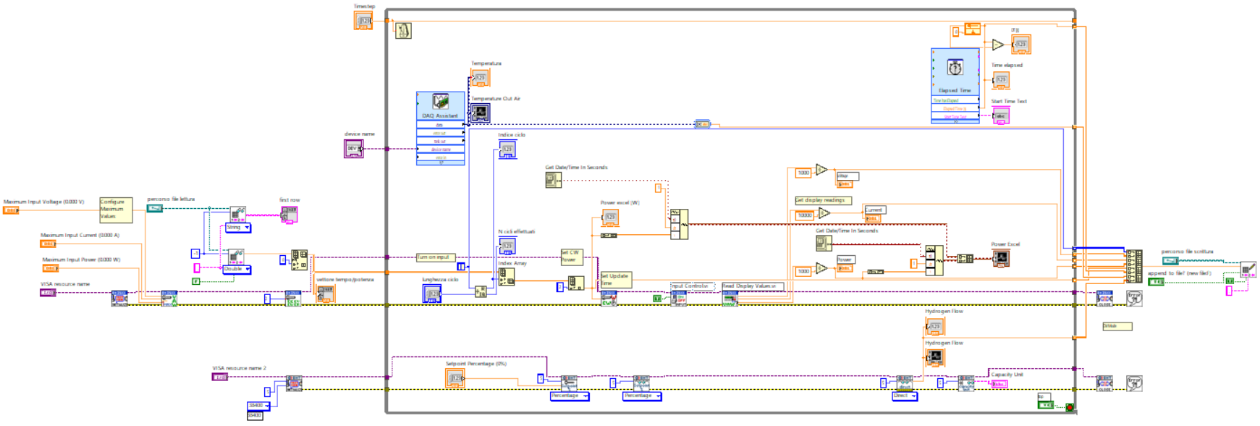

Figure 25: Complete LabVIEW block diagram of the developed VI

Due to its complexity and for better readability, the diagram is hereafter divided into three functional sections, which are described in detail.

The first section of the block diagram (Figure 26) manages the initialization of the electronic loads and the import of the power profile used as input for the test.

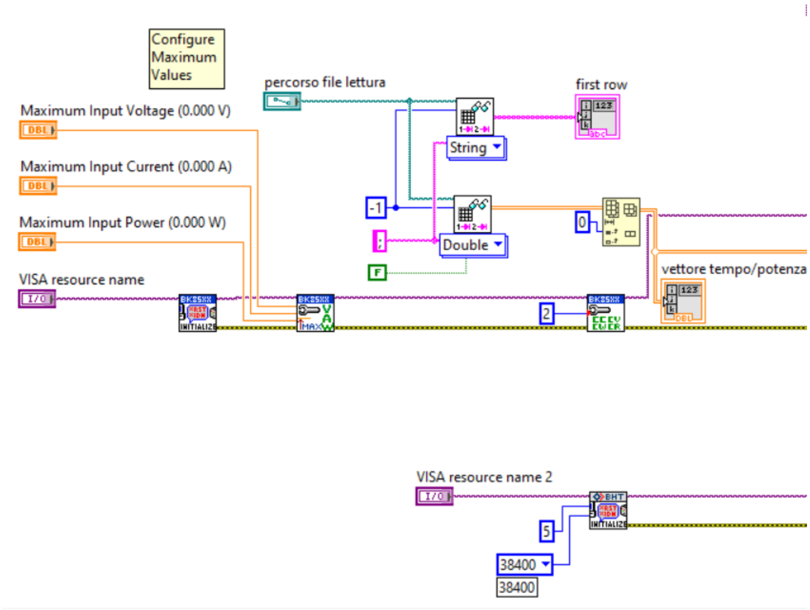

Figure 26: Initialization and Input File Handling

On the left-hand side, the maximum admissible values of voltage, current, and power are set, which define the operating limits of the BK Precision 8520 electronic load. These parameters are transferred through the VISA communication protocol, ensuring that the device is correctly initialized before the test starts.

In parallel, the program reads the power profile from an external file in .csv format, specified by the “file path” control. The file is imported and converted into numerical arrays corresponding to time and power setpoints. The first row of the file is identified and processed, after which the values are organized into a time/power vector that will be used to drive the electronic load according to the desired profile.

Finally, a second VISA communication channel (bottom part of Figure 26) is initialized to establish a connection with the hydrogen flow meter, setting its communication parameters.

The central part of the block diagram (Figure 27), enclosed within a while loop, constitutes the core of the acquisition and control system. During each iteration, LabVIEW performs several coordinated tasks, ensuring both the monitoring of the fuel cell system and the management of the electronic load.

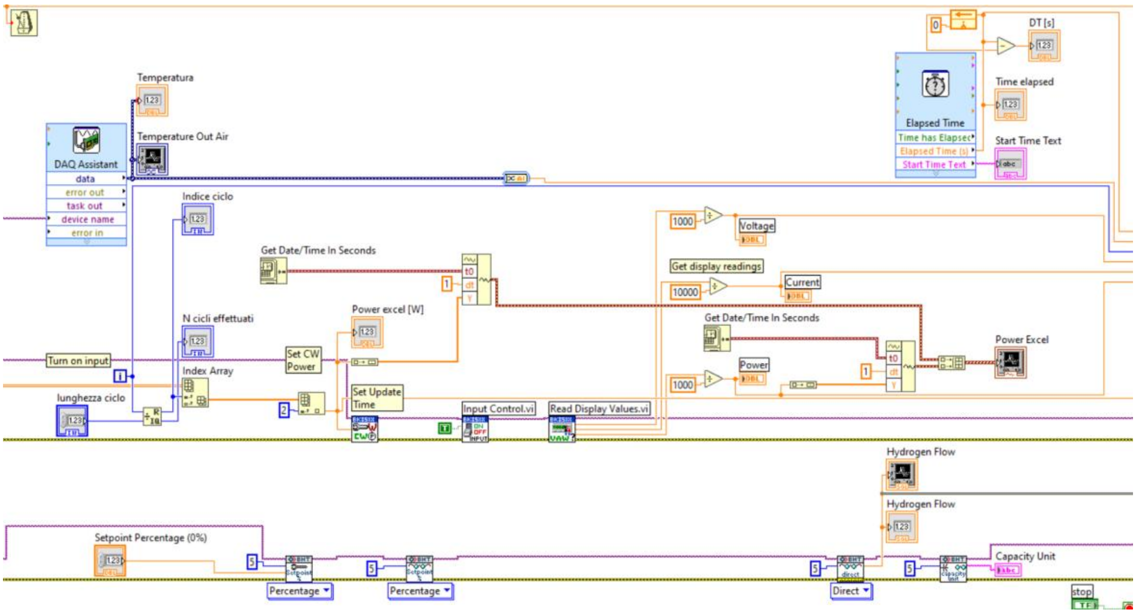

Figure 27: Main Acquisition and Control Loop

First, the loop acquires the real-time measurements of voltage, current, and power from the electronic load, using VISA communication blocks. These values are continuously updated and displayed on the front panel gauges, providing the operator with an immediate visualization of the system status. In addition, the instantaneous temperature is read from the *NI DAQ* module through the *DAQ Assistant* block, allowing for thermal monitoring of the system during operation.

The loop also handles the execution of the power profile imported from the input file: at each time step (defined by the “timestep” parameter, in the top left-hand corner), the corresponding setpoint is sent to the electronic load, which applies the required power to the fuel cell. This enables both static and dynamic test conditions to be reproduced faithfully.

Simultaneously, the hydrogen flow sensor is read through the second VISA interface. The measured values are combined with the electrical data to prepare a complete dataset describing the performance of the fuel cell system.

Finally, all the acquired signals (time, voltage, current, power, temperature and hydrogen flow) are organized into arrays and written in a csv (Comma-Separated Values) output file using the *Write to Spreadsheet File* function. This format was chosen for its simplicity and compatibility with common analysis tools such as MATLAB and Excel, making the post-processing of experimental results straightforward.

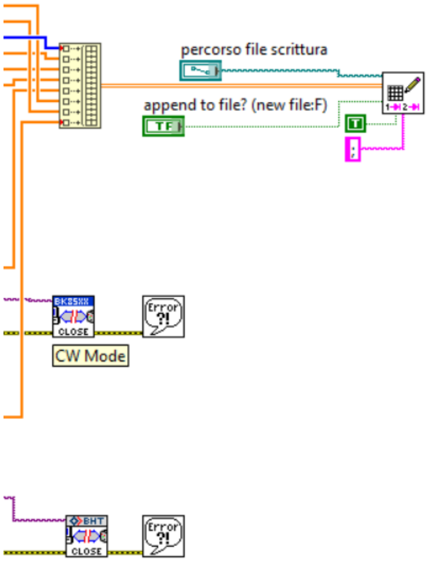

Figure 28: File writing

A dedicated control allows the user to select the file path for data storage, while an option flag (*"append to file"*) ensures flexibility: the program can either overwrite an existing file to create a new dataset or append new measurements to a previously generated file, depending on the requirements of the test.

This block is therefore fundamental to ensure that all experimental data are recorded in real time and preserved in a consistent format, providing a reliable basis for the subsequent efficiency analysis and validation of the fuel cell system.

3 Data analysis/Results

3.3 Fuel cell operation analysis

3.3.1 Test 1

The aim of this experimental test was to analyse the operational behaviour of the fuel cell under variable load conditions, in order to assess its performance in response to different power demands. For the data acquisition, the test was conducted using the software LabVIEW, which allowed for real-time monitoring of main parameters of the system, as described in detail in section 2.3.1.

A predefined load profile was created using an Excel file containing a sequence of power values that changed at fixed time intervals. This approach allowed us to study the effect of variations in electrical load on the system's efficiency and stability.

The test lasted approximately 65 minutes and was intended as an initial assessment to verify the correct operation of the fuel cell and evaluate its efficiency under controlled conditions. For this purpose, a dedicated firmware was uploaded to enable bench testing of the fuel cell. This firmware allowed the hydrogen tank sensor to be bypassed, as the system would not have started otherwise.

Following this preliminary test, a second experimental session will be conducted using dynamic loads, with the objective of simulating a realistic flight scenario of the drone.

3.3.1.1 Analysis

In this first test, during the final two power steps (2700 W and 2900 W) the second electronic load (1200 W) was activated. This was necessary to handle the increased power demand, as the primary electronic load alone was not capable of sustaining the required output beyond its rated capacity. By enabling the additional load in the final phase of the test, we ensured that the system could safely deliver the full input power without overloading the equipment.

Figure 29 shows the power profile that was given as input to the system.

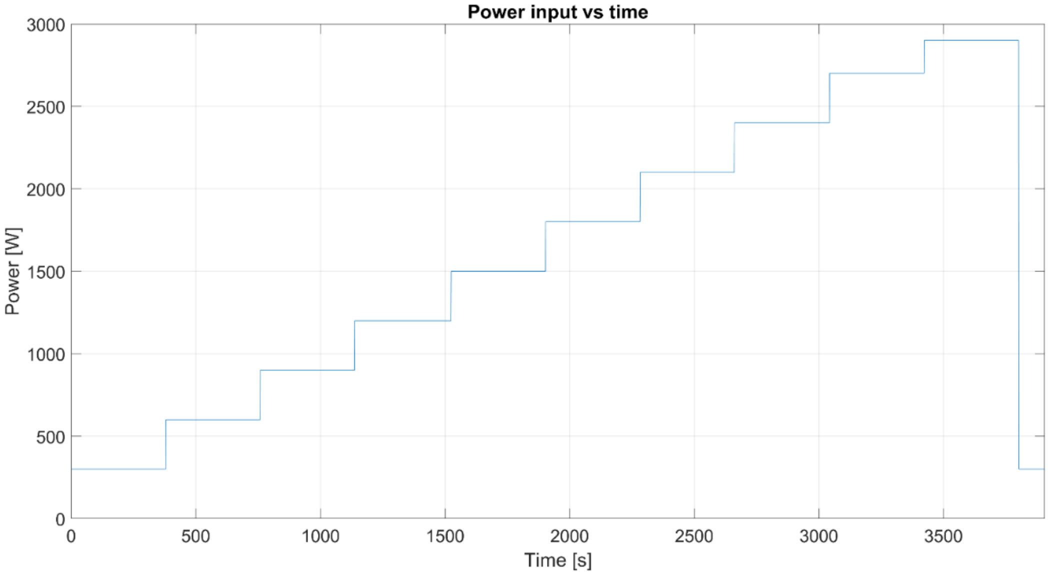

Figure 29: Power input - test 1

The parameters acquired through LabVIEW, and printed in the Excel file are: time [seconds], voltage [Volt], current [Ampere], power [Watt], temperature air out of the fuel cell [°C], hydrogen flow [Normal Litres/minute]

The analysis of these parameters, along with the corresponding plots, were carried out using MATLAB.

The voltage remained almost constant at around 50 V, as reported in Figure 30.

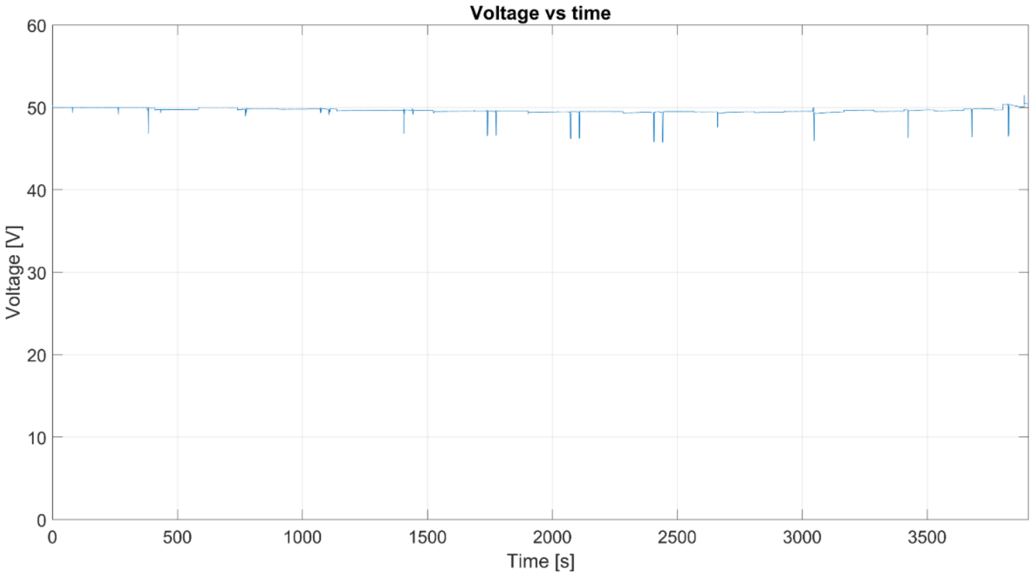

Figure 30: Voltage – test 1

The current followed the trend of the power which, except for a few sudden drops, generally followed the pattern of the input provided, as it is shown in Figure 31 and Figure 32. The value of the current follows the equation:

$$Current = \frac{Power}{Voltage}$$

For example, at the power peak value of 2900 W:

$$I_{2900\ W} = \frac{2900\ W}{50\ V} = 58\ A$$

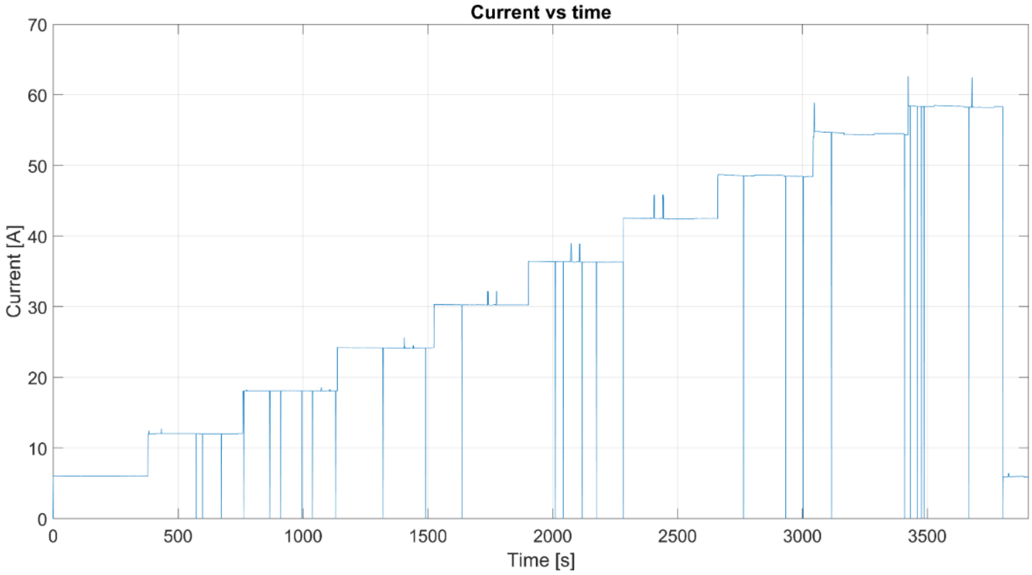

Figure 31: Current – test 1

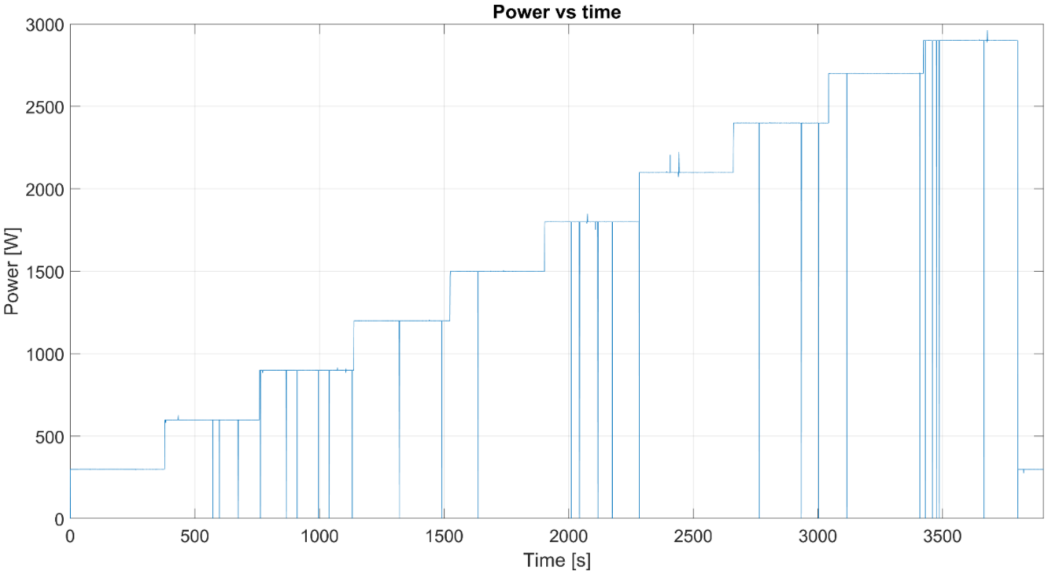

Figure 32: Power output – test 1

In Figure 33 is illustrated the temperature measurement of the outlet air: it is visible that after an initial warm-up phase of the cell, the outlet air temperature stabilized between 40°C and 45°C, reaching the peak at 45.64°C. This measurement was useful to detect any potential issues related to excessive temperature rise when increasing the power level.

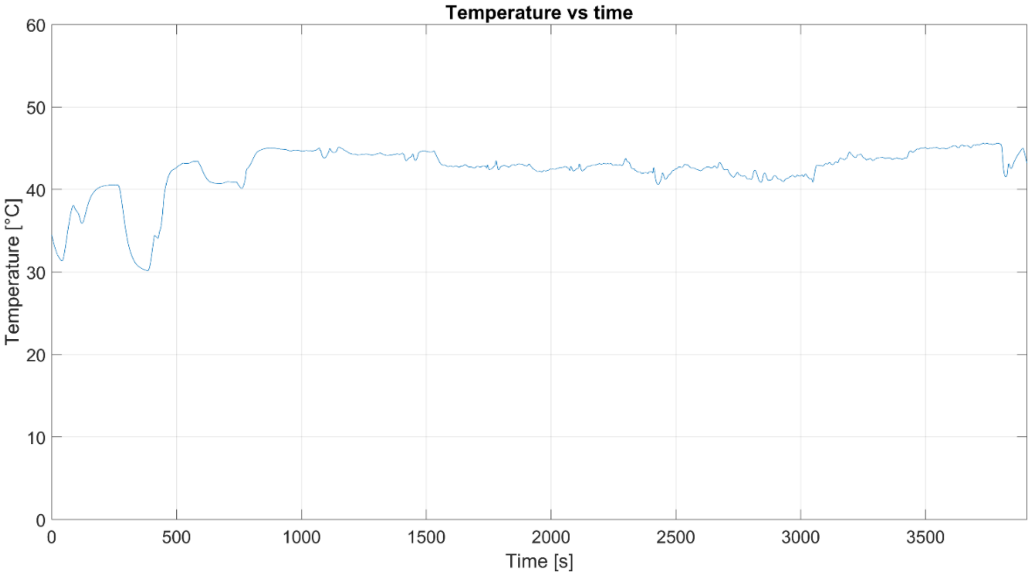

Figure 33: Outlet air temperature of the Fuel Cell – test 1

The hydrogen flow (Figure 34) generally showed significant fluctuations (initially larger, between 5 and 30 NL/min) and overall followed an increasing trend with the power demand. Note that the higher peaks are associated with the purge events. During these phases, the anode outlet valve opens suddenly, releasing hydrogen, causing a temporary and abrupt increase in the measured flow rate.

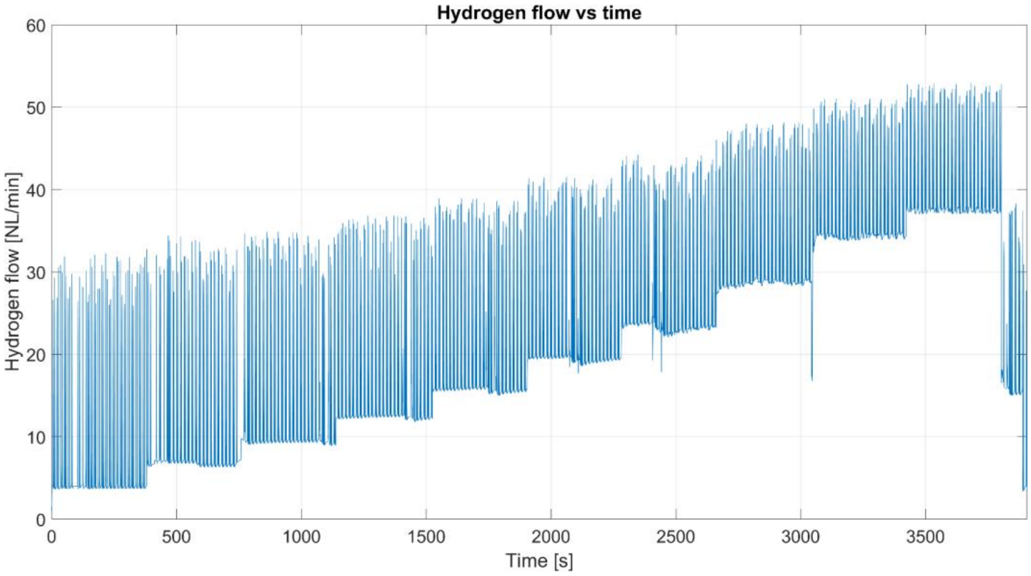

Figure 34: Hydrogen flow consumption – test 1

3.3.1.2 Log Analysis

The log file acquired from the fuel cell control unit, stored on the system's SD card, is saved in CSV format and contains a time-series recording of the system's key operational parameters. Specifically, it includes the values of voltage, current and power for the different components involved in the powertrain:

- Battery
- SPM1 (Smart Power Module 1)
- SPM2 (Smart Power Module 2)

In addition to these component-specific measurements, the log file also provides the value of System Output Power, which represents the total power delivered by the system as a whole.

A comparison between the log file and the data acquired via LabVIEW reveals the presence of an offset between the measured power and the System Output Power value reported in the log file, as depicted in Figure 35.

However, when computing the sum of the power values from SPM1 and SPM2 and including the contribution of the battery, the resulting total power (blue curve) matches closely with the one obtained from the LabVIEW data (yellow curve), especially at high power values. This consistency confirms the validity of the measurements and supports the reliability of the experimental setup, especially in terms of power distribution among the system components.

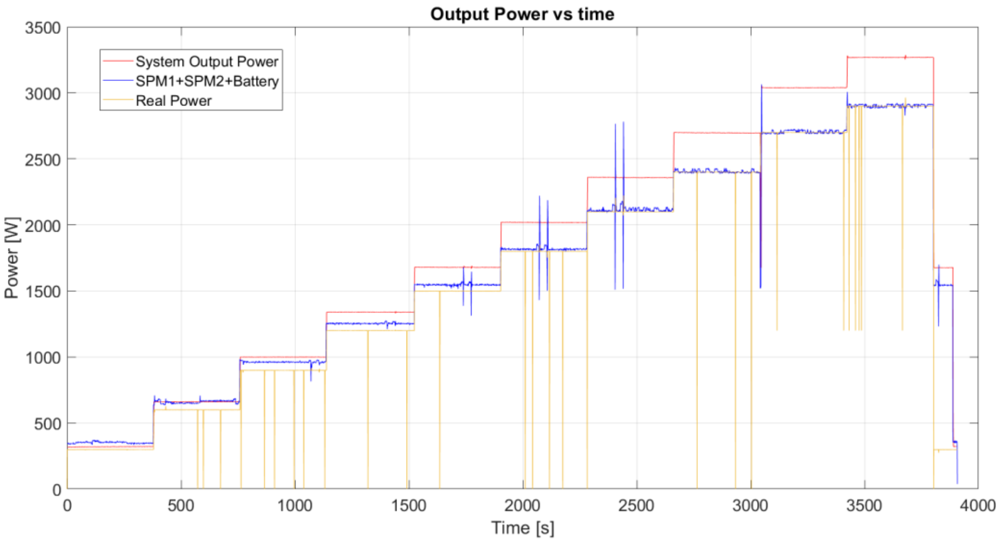

Figure 35: Comparison between different curves of Output Power – test 1

The discrepancy in the System Output Power value recorded in the log file suggests that the fuel cell system is not correctly measuring this parameter. Moreover, another inconsistency is observed in the battery power, since when the fuel cell is turned off, a charging power of about 80 W is recorded, which is not physically possible.

3.3.1.3 Efficiency calculation

One of the main objectives of this test was to construct the efficiency curve of the fuel cell. This curve serves as a fundamental tool for assessing the system's performance across different power levels and is essential for characterizing its operational behaviour.

The system efficiency was calculated as the ratio between the electrical energy produced and the chemical energy supplied by hydrogen, according to the following expression:

$$\eta = \frac{\int P_{el} dt}{\int P_{H_2} dt}$$

In this equation, P_{el} represents the instantaneous electrical power delivered by the system, while P_{H_2} denotes the chemical power associated with hydrogen consumption.

The integrals in the numerator and denominator provide, respectively, the total electrical energy produced and the total chemical energy supplied during the considered time interval. This approach accounts for possible instantaneous fluctuations in power and yields a comprehensive and representative measure of the system performance.

Primarily we have to calculate the power supplied by the hydrogen. In order to do so, we must convert the hydrogen flow from [NL/min] to [mol/s].

We know that in standard conditions (T=0°C, p=1 atm):

$$1\, mol\ H_2 = 22.414\ NL$$

So:

$$\dot{n}_{H_2}\left(\frac{mol}{s}\right) = \frac{H_2 flow\left[\frac{L}{min}\right]}{22.414\left[\frac{L}{mol}\right] * 60\left[\frac{s}{min}\right]}$$

Then we can find the power provided by the hydrogen using the following equation:

$$P_{H_2} = \dot{n}_{H_2} * \Delta H$$

Where ΔH=241.83 [KJ/mol] is the Lower Heating Value (LHV) of Hydrogen.

Then the formula of η was applied to each power step to determine the corresponding average efficiency, using the data recorded during the steady-state period of each step, which lasted approximately 380 seconds.

In doing so, we obtain a characteristic efficiency-power curve typical of fuel cell systems (Figure 36), which has a peak value at intermediate power steps and drops slightly at high power.

It can be observed that the maximum efficiency is essentially equal to the nominal value of 45% and is achieved within the power range of 1500 W to 2100 W.

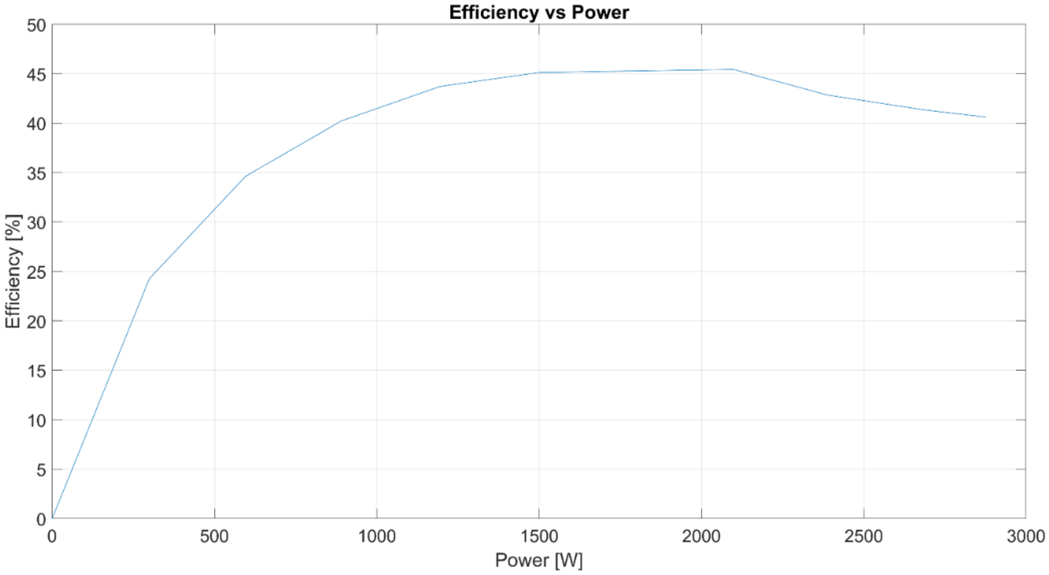

Figure 36: Efficiency curve of Fuel cell system

3.3.2 Test 2

Following the preliminary test conducted under stepwise power conditions, a second experimental campaign was carried out to assess the performance of the fuel cell under dynamic load conditions. In this test, the power demand profile was derived from a real flight mission performed by the drone, in order to simulate operating conditions as close as possible to actual in-flight behaviour.

As in the previous test, the setup was managed through the LabVIEW-based acquisition system. The power profile was provided as input via an Excel file, while the corresponding measured data (such as voltage, current, power output, temperature and hydrogen flow) were recorded and saved in a separate Excel output file for subsequent analysis. This approach allowed us to capture the behaviour of the system and evaluate its response to rapid power fluctuations, which are typical during flight manoeuvres.

The main goal of this dynamic test was to analyse real-time performance and the behaviour of the fuel cell throughout a realistic mission profile, in preparation for its integration into a fully operational aerial platform.

3.3.2.1 Analysis

In this second test, to meet the power requirements of the dynamic load profile, both electronic loads were activated. The primary electronic load (as described in 2.1.1) had a maximum capacity of 2400 W, which was insufficient to handle the power peaks observed in the flight-derived profile. To compensate for this limitation, the second electronic load rated at 1200 W was kept active throughout the entire duration of the experiment. This setup ensured that the fuel cell system could be tested under the full range of power demands without exceeding the limits of the individual loads, thereby maintaining the integrity and continuity of the test.

The input power profile (shown in Figure 37) was generated based on a real flight performed by the drone, which in this case was powered by batteries. Two power profiles of approximately 15 minutes each were acquired, placed in sequence, and repeated twice to obtain a total test duration of about 1 hour. In order to accurately reproduce the power profile, additional weight was added to the drone to simulate the mass of the hydrogen power system, in order to ensure the same MTOW as the drone powered by the hybrid system.

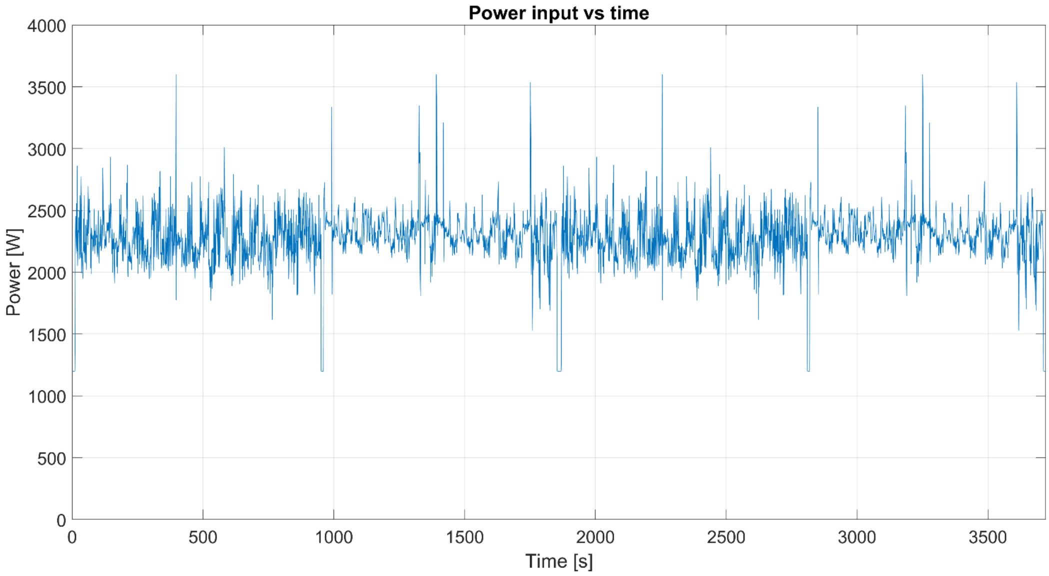

Figure 37: Power input - test 2

Below are the plots illustrating the trends of the voltage (Figure 38), current (Figure 39), and output power (Figure 40) provided by the fuel cell.

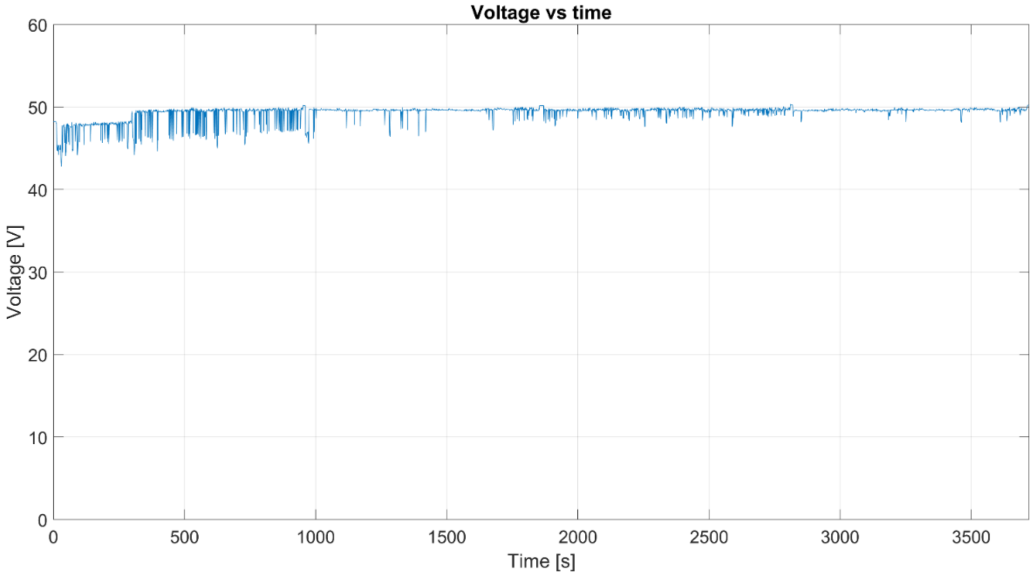

Figure 38: Voltage: test 2

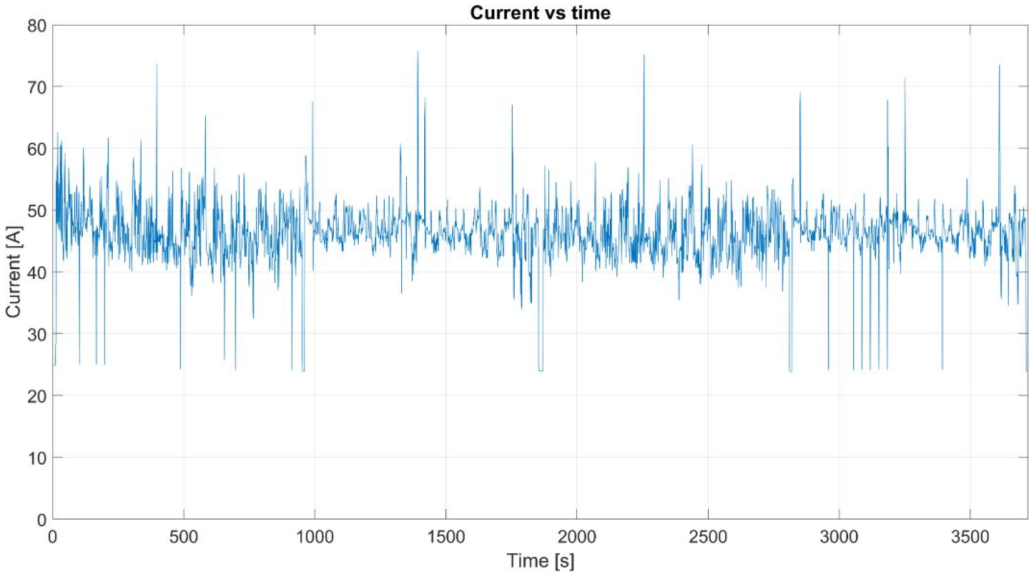

Figure 39: Current - test 2

The output power followed the trend of the input power profile.

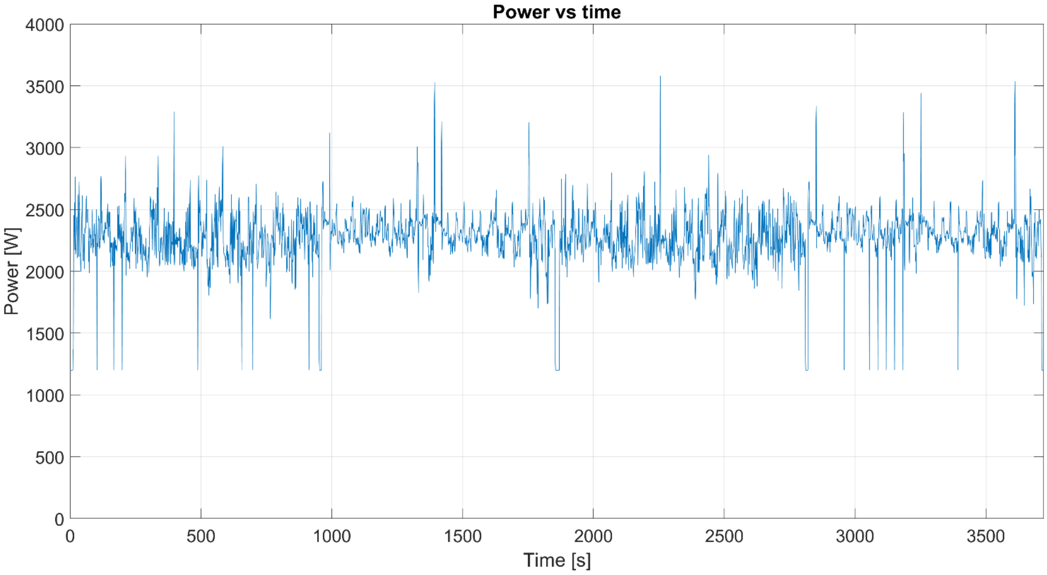

Figure 40: Power output – test 2

The outlet air temperature (Figure 41), after the initial warm-up phase, remained almost constant between 42°C and 43°C.

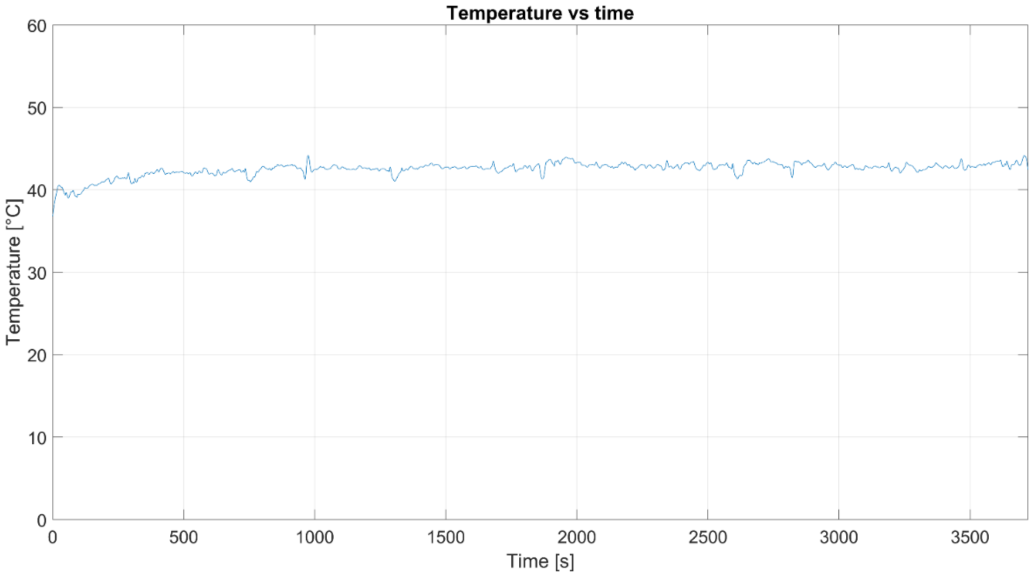

Figure 41: Outlet air temperature of the Fuel Cell – test 2

The hydrogen flow rate exhibited an oscillating trend (Figure 42), with a minimum value of 12.55 NL/min and a maximum of 51 NL/min. However, it generally remained within the 20–30 NL/min range and the higher peaks were associated with the purge events, as described in the analysis of test 1 (section 3.3.1.1). The total amount of hydrogen consumed during the test was 156 g, which corresponds to almost 80% of the theoretical hydrogen content of the 9L 300 bar tank.

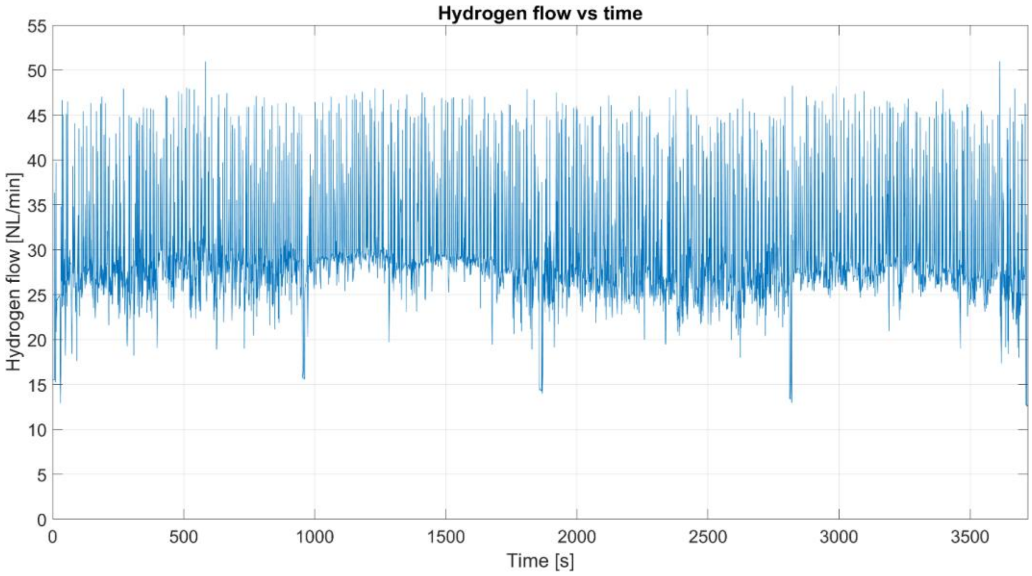

Figure 42: Hydrogen flow consumption – test 2

3.3.2.2 Log Analysis

In the second test performed under dynamic load conditions, the offset observed in the first test between the measured power and the System Output Power value acquired in the log file is confirmed, as illustrated in Figure 43.

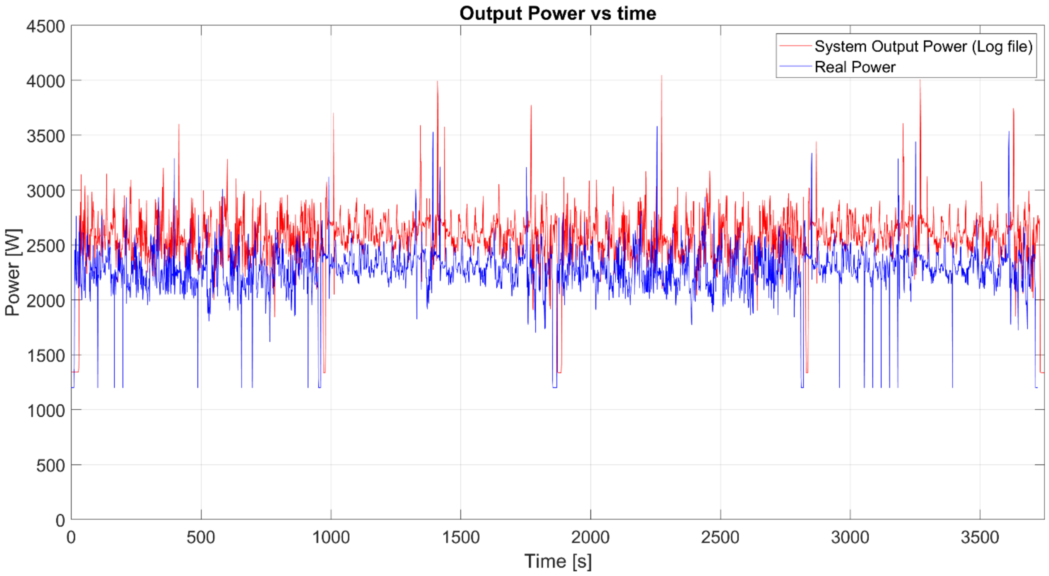

Figure 43: Comparison between System output power (Log file) and Real Power acquired through LabView

However, we also observe that the curve representing the system real power closely matches the one obtained by summing the power output of SPM1, SPM2, and considering the contribution of the battery. This further confirms that, especially at higher power levels, the agreement between these curves remains consistent, as already observed in Test 1 and as it can be seen in Figure 44.

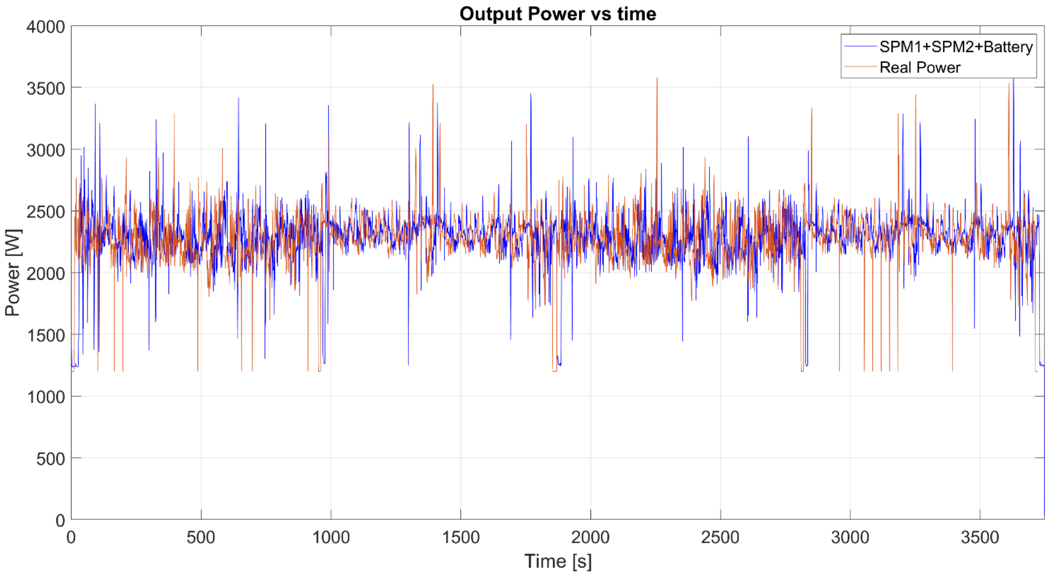

Figure 44: Comparison between sum of SPM1+SPM2+battery contribution and Real Power acquired through LabView

It is interesting to observe the behaviour of the power output from SPM1 and SPM2 (Figure 45): it is evident that they do not exactly split the power output requested, as they do not deliver the same amount of power at every instant. Moreover, it is worth noting that, at certain moments, they alternately stop supplying power, as part of the fuel cell system's management strategy, with the battery compensating to meet the power demand of the load.

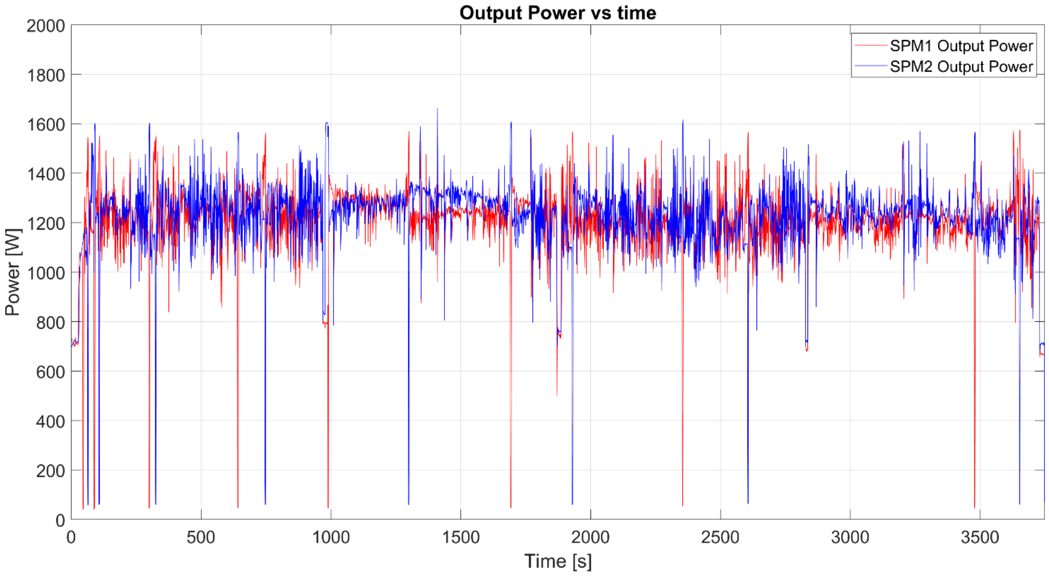

Figure 45: SPM1 and SPM2 output power – test 2

Figure 46 shows the power trend of the battery: when the value is negative, the battery is supplying power to the system, meanwhile when it is positive, the battery is being recharged.

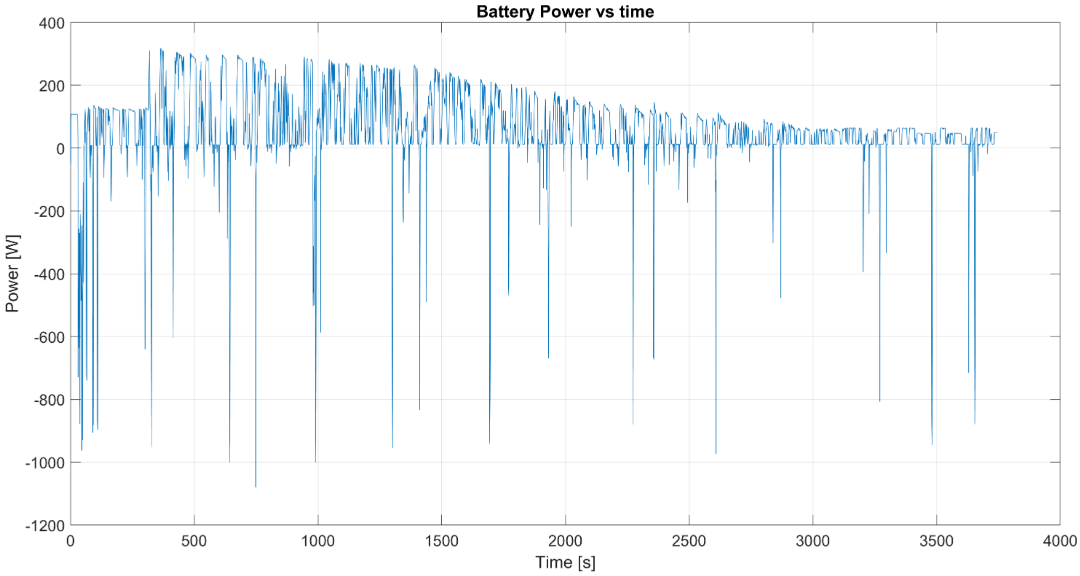

Figure 46: Battery power supply – test 2

Figure 47 shows the power distribution among SPM1, SPM2, and the battery. It is interesting to note that the two Smart Power Modules share the power almost equally, while the battery is slightly recharged for most of the time, although it is required at certain moments to compensate for power peaks. It is important to highlight that in this case a negative value for the battery indicates that it is being recharged, whereas a positive value means that it is discharging and supplying power to the system.

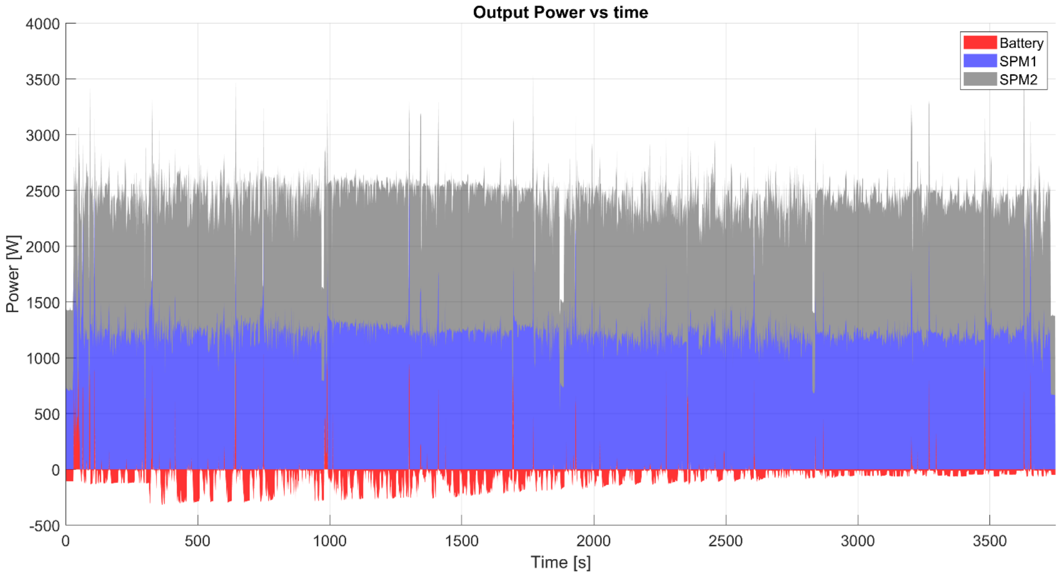

Figure 47: Power sharing between SPM1, SPM2 and the battery

3.3.2.3 Efficiency calculation

The efficiency was calculated using the same methodology adopted in Test 1, described in section 3.3.1.3.

The calculated average efficiency is 43.12%, a high value which can be explained by the fact that the fuel cell operates within a power range where, as demonstrated in the stationary test, the efficiency is very close to the system's nominal value of 45%, providing further evidence of the reliability and consistency of the experimental test.

3.4 Flight Test

After the completion of bench tests, during which the fuel cell system was evaluated under controlled laboratory conditions, a flight test was conducted to validate its performance in a real operating environment. This test represent a crucial step in the experimental campaign, as it allows the assessment of the system's behaviour under actual flight dynamics, including variations in load demand and environmental conditions. The transition from laboratory to flight testing provides essential insights into the integration, reliability, and overall efficiency of the fuel cell system when installed on board the aerial platform.

3.4.1 Hover test flight

The flight test was conducted on September 12, 2025, on a sunny day with light wind and consisted of a hover operation lasting approximately 50 minutes with zero payload. This test was carried out in a green field in the countryside near Chivasso (TO) and aimed at evaluating the performance and stability of the fuel cell system under steady flight conditions, where power demand remains relatively constant.

The cylinder employed is a certified type 3 model manufactured by Luxfer, with a nominal volume of 9 L, and is capable of storing up to 180 g of hydrogen at a pressure of 300 bar.

The quadcopter drone used in the test is shown below in its folded (Figure 48) and deployed (Figure 49) configurations. Table 11 summarizes its main characteristics.

Figure 48: Folded drone

Figure 49: Deployed drone

Table 11: Main characteristics of quadcopter drone

Characteristic	Value
Motor centers distance	1456 [mm]
Dimension: deployed arms and propellers	1766*1766*863 [mm]
Dimension: folded arms	600*630*863 [mm]
Propeller diameter	29”
MTOW	18700 [g]

As observed during the laboratory experiments, the flight test results also show that the voltage (Figure 50) remained essentially stable, maintaining a value of approximately 50 V.

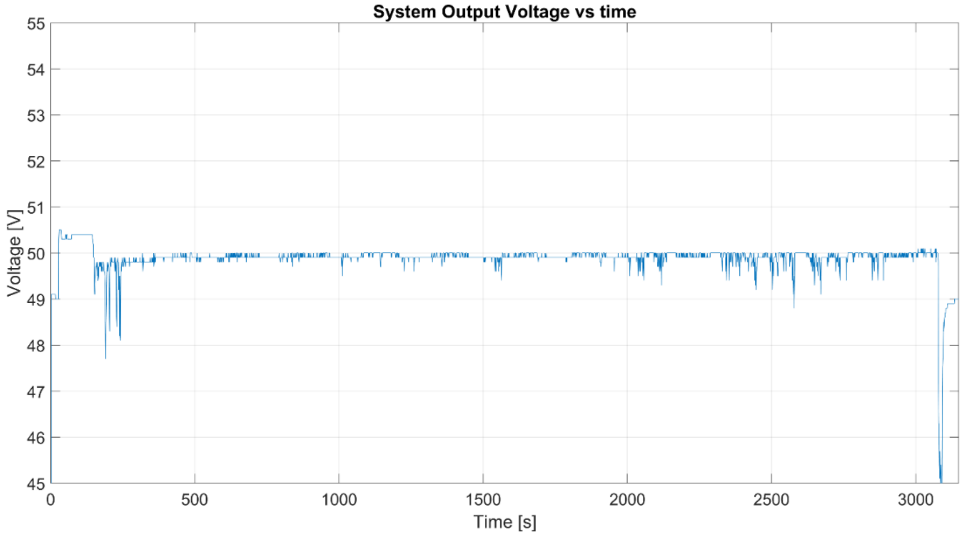

Figure 50: Voltage - Hover flight

The current (Figure 51) exhibits oscillations between 44 A and 55 A (with some peaks near 60 A), following the same trend observed in the power profile.

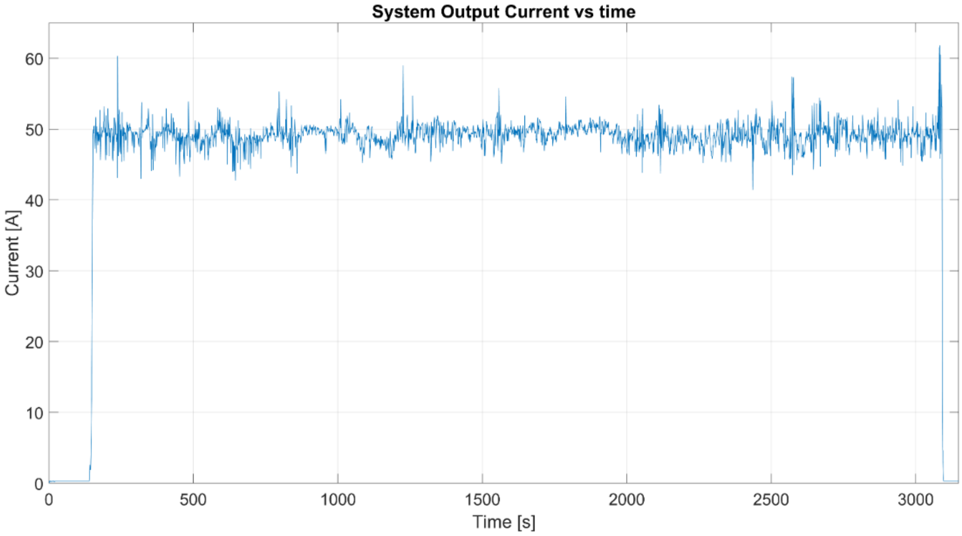

Figure 51: Current - Hover flight

As highlighted in the laboratory test analysis, the “System Output Power” value recorded by the system is affected by a measurement error. Therefore, the output power plot (Figure 52) was obtained by summing the contributions of SPM1, SPM2 and the battery, which proved to be consistent and accurate.

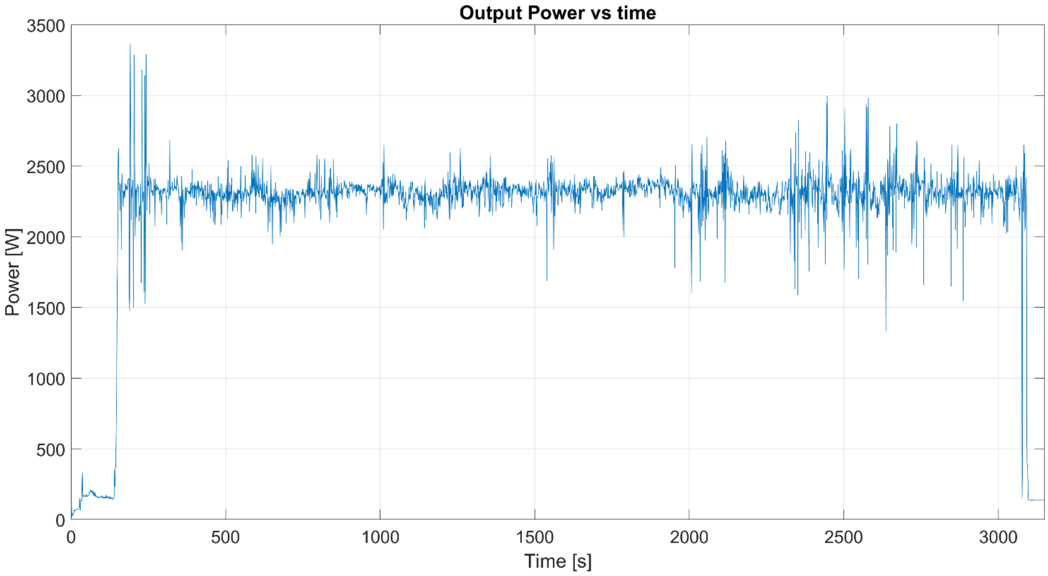

Figure 52: Output power - Hover flight

To determine the efficiency of the propulsion system, the following formula was applied:

$$\eta = \frac{P_{ideal}}{P_{real}}$$

Where P_{ideal} is obtained from the Momentum theory (or Disk Actuator theory):

$$P_{ideal} = \frac{\left(\frac{Thrust/4 * 9.81}{1000}\right)^{\left(\frac{3}{2}\right)}}{\sqrt{2\rho\pi r^2}}$$

In this case:

- Thrust is expressed in [g] and represents the weight of the drone, which is divided by 4 to consider the thrust required from a single rotor
- ρ=1.225 kg/m^3 is the air density at sea level
- r=14.5” = 36.83 cm = 0.3683 m is the propeller radius.

By calculating the average value of the power actually required by the drone (P_{real}) and dividing it by four to obtain the reference for a single rotor, was determined that η=51%.

The following graph (Figure 53) confirms the presence of the offset between the real output power (calculated as the sum of SPM1, SPM2 and the battery contribution, shown in red) and the "System Output Power" value acquired by the fuel cell (shown in blue).

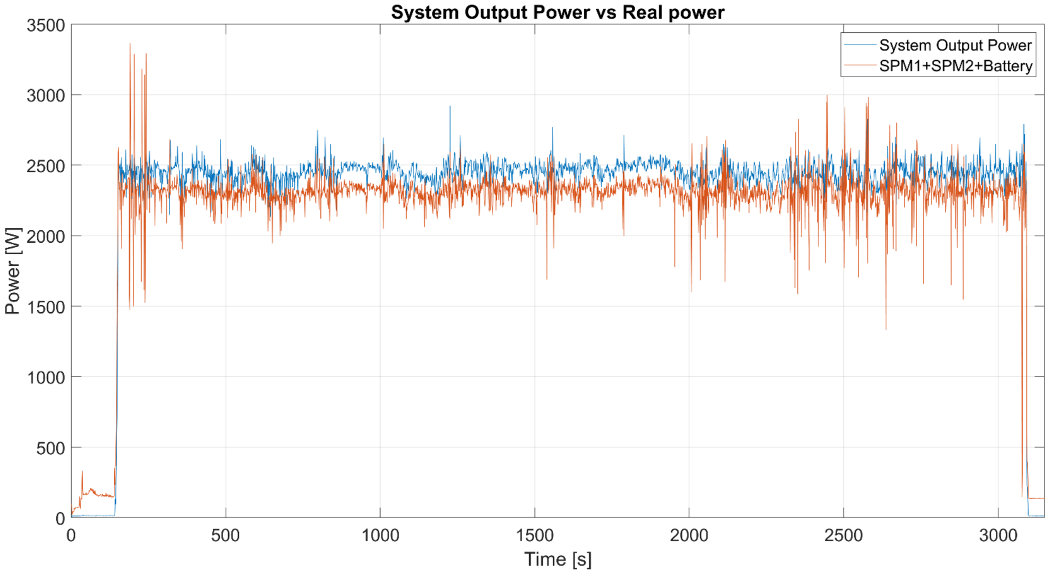

Figure 53: Comparison between System Output Power and sum of SPM1+SPM2+battery contribution – Hover flight

As already observed in the laboratory tests, this flight test also confirms that the SPM1 and SPM2 modules do not deliver exactly the same amount of power at every instant (Figure 54). Instead, they alternate, reflecting a dynamic power-sharing mechanism.

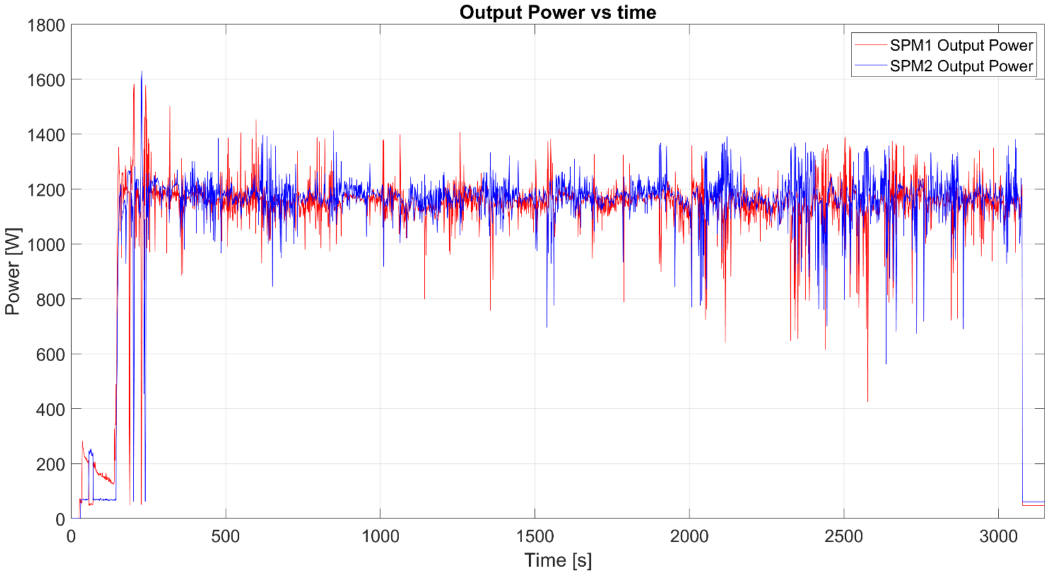

Figure 54: SPM1 and SPM2 output power - Hover flight

Figure 55 illustrates the distribution of power among SPM1, SPM2, and the battery. As in the bench test (section 3.3.2.2) it can be seen that the two Smart Power Modules share the power almost equally, while the battery provides a minimal yet essential contribution, in particular in this case it is important to enable landing once the hydrogen is depleted.

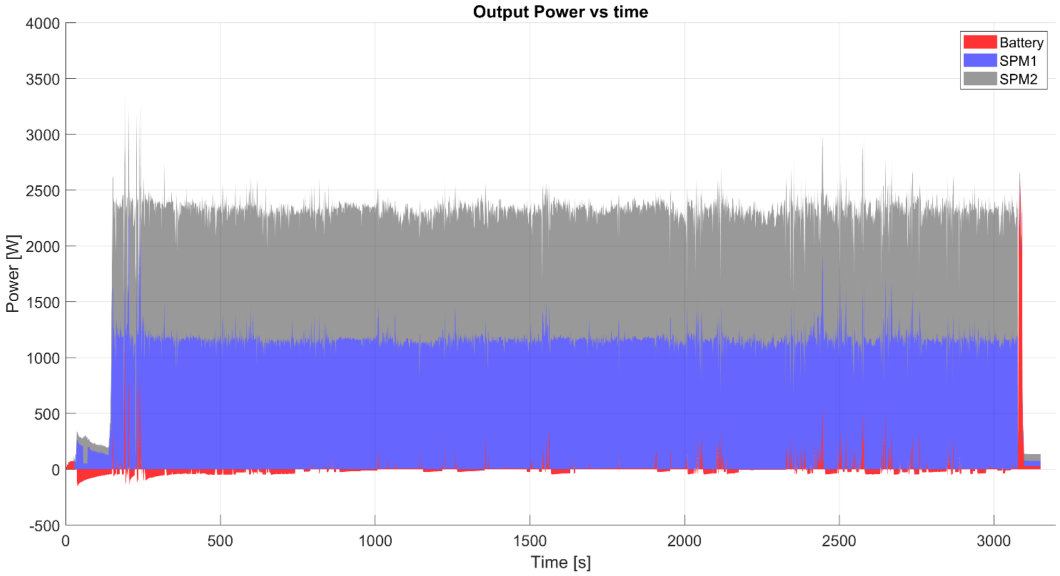

Figure 55: Power contribution of SPM1, SPM2 and battery

As shown in Figure 56, after an initial warm-up phase, during which the fuel cell temperature slightly increased from 24 °C to 26 °C, the air inlet temperature exhibited an oscillatory trend. Specifically, SPM1 showed more pronounced fluctuations, ranging between 21.3 °C and 24.9 °C, while SPM2 maintained a more stable profile, with temperatures between 21.7 °C and 23.7 °C.

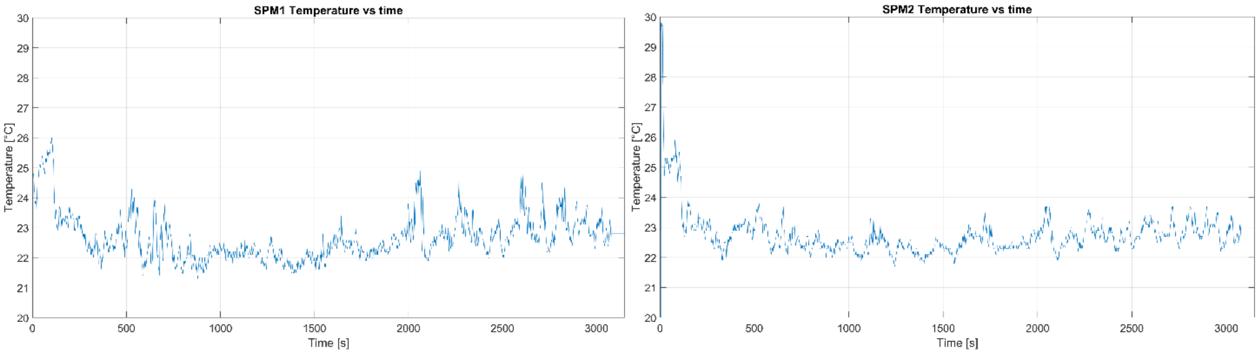

Figure 56: SPM1 and SPM2 air inlet temperature - Hover flight

Figure 57 illustrates the evolution of the tank pressure during the test. The initial value was approximately 185 bar, and it exhibited an almost linear decrease, dropping by about 60 bar every 1000 seconds, corresponding to 0.06 bar per second. At the end of the test, a residual pressure of 5 bar was reached.

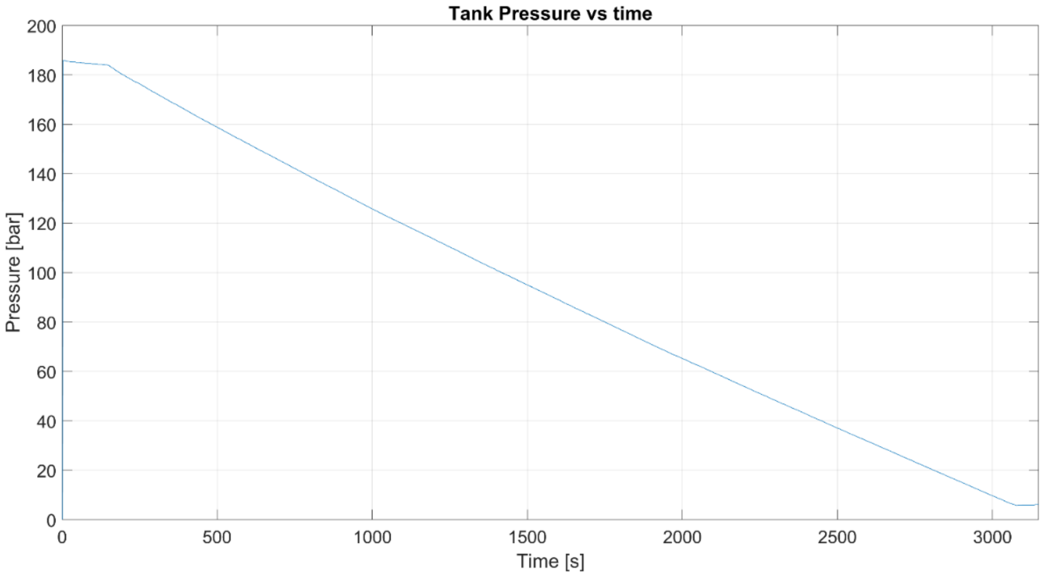

Figure 57: Tank pressure - Hover flight

Considering that the storage tank can theoretically be filled up to 300 bar, it is possible to estimate the maximum achievable endurance by applying the following proportional relationship:

$$[m_{H2}(185\ bar) - m_{H2}(5\ bar)] : [m_{H2}(300\ bar) - m_{H2}(5\ bar)] = t(185\ bar) : t(300\ bar)$$

The hydrogen mass can be rewritten as $m_{H2} = \rho * V$

Where ρ is the hydrogen density (at 20 °C) and V is the tank volume (9 L).

So:

$$t(300\ bar) = Max\ endurance = \frac{\rho(300\ bar) - \rho(5\ bar)}{\rho(185\ bar) - \rho(5\ bar)} * t(185\ bar)$$

Where:

- ρ (300 bar) = 20.839 g/L
- ρ (185 bar) = 13.723 g/L
- ρ (5 bar) = 0.41231 g/L
- t (185 bar) = 52 min

By replacing the hydrogen density values corresponding to the various pressure conditions, the following result is obtained:

$$Max\ endurance = 79.8\ [min]$$

To establish a comparison with a drone powered exclusively by batteries, it is possible to estimate the potential endurance that such a system would achieve if it were to possess the same weight as the drone operated by the hybrid power system.

An average energy density of 200 Wh/kg is considered, which, assuming an efficiency of 80%, corresponds to 160 Wh/kg. For a power system mass of 10 kg, this results in a total available energy of 1600 Wh. Given an average power consumption of approximately 2300 W, potential endurance can be obtained simply by dividing the available energy by the average power:

$$t = \frac{Total\ energy}{Average\ power} = \frac{1600\ Wh}{2300\ W} * 60\frac{min}{h} = 42\ min$$

It can be observed that the resulting value of 42 minutes is approximately half of the potential endurance of the drone powered by the hybrid system with the hydrogen tank filled to its maximum pressure of 300 bar.

Figure 58 shows the evolution of the battery state of charge (SOC) over the duration of the test, assuming an initial value of 80%. The SOC initially rises to a peak value of 84.7%, indicating a charging phase. After reaching its peak, the SOC remains relatively stable, reflecting a period of balanced charge and discharge. After 40 minutes, the battery began to discharge slowly, before experiencing a drop toward the end of the test (due to hydrogen depletion), reaching 75.8%. Overall, the graph highlights that, for the majority of the test, the battery was recharged by the power supplied from the fuel cell, with the exception of the final phase. The SOC reached a level of 82.5% prior to the observed drop, which can be considered a satisfactory value, providing the possibility of a few additional minutes of flight powered solely by the battery.

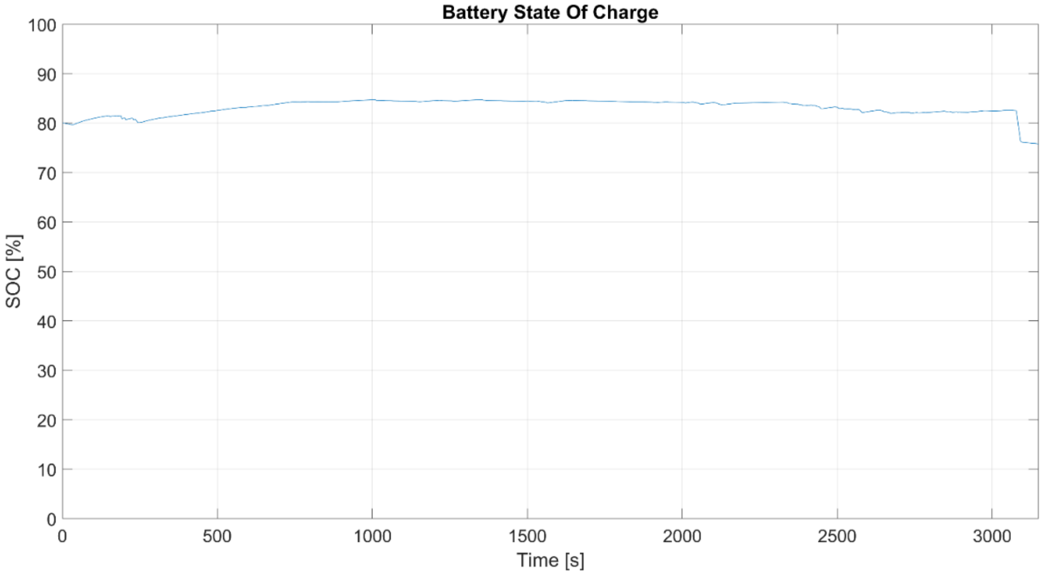

Figure 58: Battery state of charge - Hover flight

4 Hexacopter configuration analysis

4.1 Model description

In this chapter, a hexacopter drone model is presented, designed using SolidWorks and inspired by the layout of the Gryphon Hexacopter (Figure 59). The development of this model was driven by the objective of enhancing the drone's endurance and/or payload capacity. By adopting a six-rotor configuration, the design aims to provide greater thrust while potentially maintaining the same overall weight, thereby improving performance.

Figure 59: Gryphon Hexacopter [63]

The SolidWorks project includes the structural design of the drone and is illustrated in Figure 60, with details in Figure 61, Figure 62 and Figure 63.

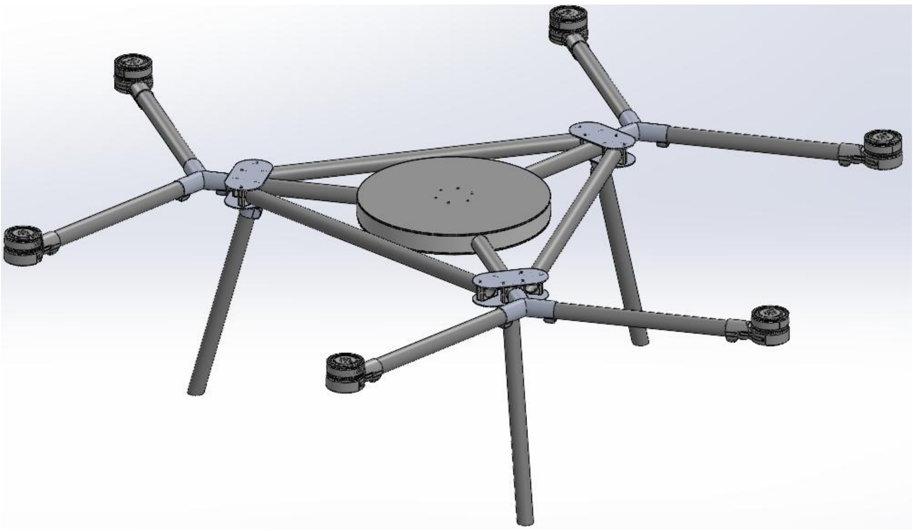

Figure 60: Solidworks model

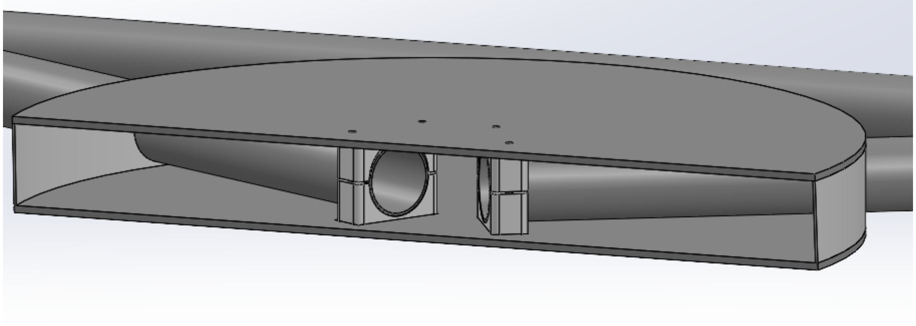

Figure 61: Central frame plates

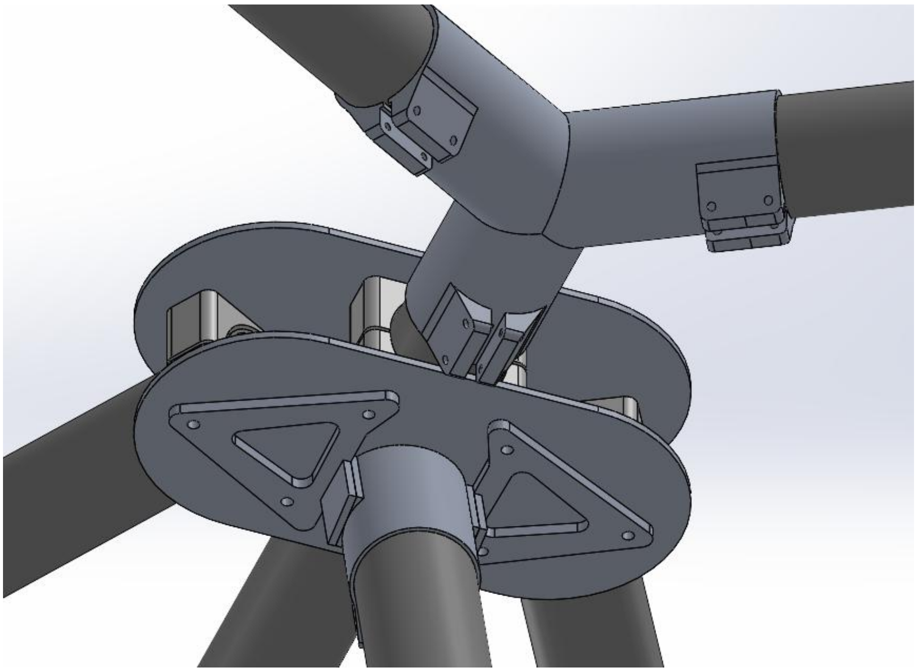

Figure 62: Landing gear attachment, Y-shaped connector and outer plates for arm attachment

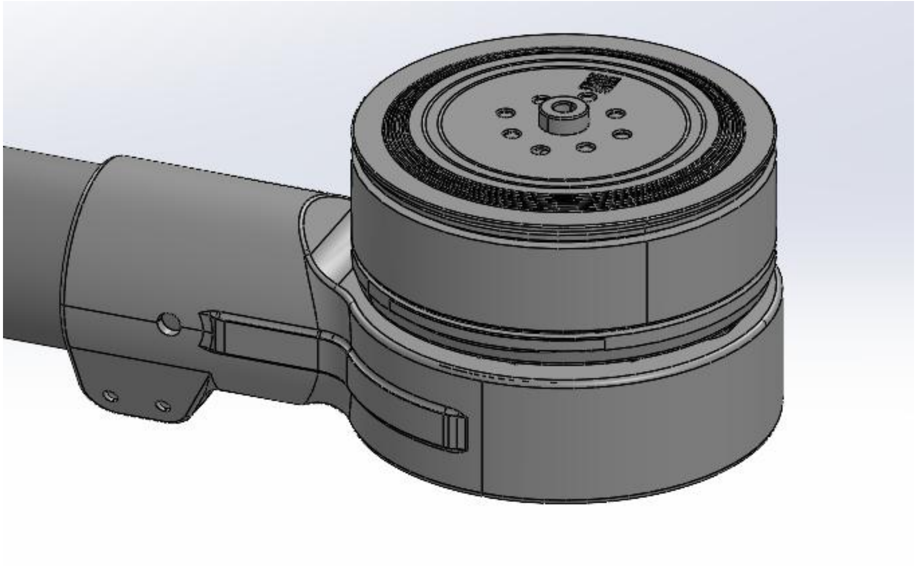

Figure 63: H8M motor

4.2 Weight and cost analysis

Table 12 summarizes the weights and costs of the various components of the drone's structural frame.

Table 12: Summary of weight and cost analysis for structural components [64], [65], [66], [67]

Component	Weight [g]	N°	Total Weight [g]	Total cost [€]
Central frame	1277.11	1	1277.11	490.3
Triangle-shaped arms	98.85	3	296.55	130.2
Outer plates	159.01	3	477.03	120
Y-shaped connector	79.75	3	239.25	225
Motor	458	6	2748	1002.9
Propeller arms	60.59	6	363.54	159.6
Landing gear arms	63.13	3	189.39	84
Propellers 30"	71	6	426	821.1
Total			**6016.87**	**3033.1**

The weight estimation was performed by assigning appropriate materials to each component within SolidWorks, such as carbon fiber for the arms and central plates, aluminum alloy for connectors and outer plates and plastic for arm mounting brackets. On the other hand, the weight and cost of the motor assembly (H8M by Hobbywing) and the propeller were obtained from commercially available data.

Figure 64: H8M Motor and propeller

With regard to the carbon tubes (30 mm diameter), the cost was estimated using an average value of €70 per meter of length. This value corresponds to the average market price for medium-high quality tubes and has been rounded up to account for processing and finishing costs.

The cost of the Y-connectors and the plates was calculated using the “madeinadd.com” website, where the SolidWorks part file was uploaded in order to obtain a realistic price estimate.

The values of other weights and costs related to the power supply system and the electronic components (reported in Table 13) were taken from sections 3.2 and 3.3 of the NODES project bill of materials, which therefore represent official data.

The only exceptions are the 800 W fuel cell and the 10.8 L H_2 tank, whose weight and cost were taken directly from market data and reported in the table. In addition, the weight and cost of cables and connectors was estimated on the basis of those used for the quadcopter.

Table 13: Summary of weight and cost analysis for other components [68], [69], [70]

Component	Weight [g]	N°	Total weight [g]	Total cost [€]
Fuel Cell 2400 W	5044	1	5044	33256.65
Fuel Cell 800 W	1500	2	3000	26247.6
Hydrogen tubes	250	1	250	Incl. FC
Pressure regulator	350	1	350	1359.44
Battery	852	1	852	233.38
H_2 cylinder 9 L	4000	1	4000	350.07
H_2 cylinder 6.8 L	3000	1	3000	800
H_2 cylinder 10.8 L	4250	1	4250	4484
Interface electronics	500	1	500	Prototype
PMD	108	1	108	271.9
Flight controller	13	1	13	280
GPS	12	1	12	57.02
Receiver with telemetry	160	1	160	-
Camera	90	1	90	98.35
Fuel cell supports	56	2	112	96.6
Cylinder supports	40	2	80	46.5
Motor cables and connectors	150	1	150	100

4.3 Configurations analysis

Several configurations were analyzed based on the same layout of the hexacopter shown in section 4.1, exploring different combinations of fuel cells and hydrogen tanks.

Specifically, the possibility of using two 800 W fuel cells (for a total of 1600 W) instead of a single 2400 W unit was examined, and three certified and commercially available H_2 tanks of 6.8 L, 9 L, and 10.8 L were considered.

Below is the specification of the H8M motor unit, which serves as a basis for assessing which configurations can be supported.

Table 14: H8M motor unit specifications

Throttle [%]	Thrust [g]	Power Input [W]	Efficiency [g/W]	Thrust*6 [g]	Power Input*6 [W]	P_{ideal} [W]	η (P_{id}/P_{real}) [%]
48	2595	211.3	12.3	15570	1267.8	121.5	57.5
51	2995	260.3	11.5	17970	1561.8	150.7	57.9
54	3265	294.8	11.1	19590	1768.8	171.5	58.2
57	3510	327.5	10.7	21060	1965	191.2	58.4
60	3865	377	10.2	23190	2262	220.9	58.6

The last two columns present the calculation of the propulsion system efficiency (motor and propeller), based on the ideal power computed using the formula shown below, obtained from the Momentum theory (or Disk Actuator theory) as already seen in section 3.4.1.

$$\eta = \frac{P_{ideal}}{P_{real}} = \frac{\frac{\left(\frac{Thrust * 9.81}{1000}\right)^{\left(\frac{3}{2}\right)}}{\sqrt{2\rho\pi r^2}}}{P_{real}}$$

Where ρ= 1.225 kg/m^3 is the air density at sea level and r = 15” = 38.1 cm = 0.381 m.

Note that in this case the thrust [g] refers to a single rotor, as well as P_{real} (Power input).

From the analysis of the quadcopter flight data, it was observed that the η value stabilized at approximately 51%, so to obtain a reliable comparison and ensure a fair evaluation, the power was recalculated using this value.

The total power, considering the presence of six rotors and the recalculated efficiency, was obtained as follows:

$$Power = \frac{N}{\eta} \frac{\left(\frac{Thrust * 9.81}{1000}\right)^{\left(\frac{3}{2}\right)}}{\sqrt{2\rho\pi r^2}}$$

Where N=6 is the number of propellers, with diameter of 30”, and η=0.51.

The difference between the calculated power and the one provided by Hobbywing can also be seen from the power input (Figure 65) and efficiency (Figure 66) plots shown below.

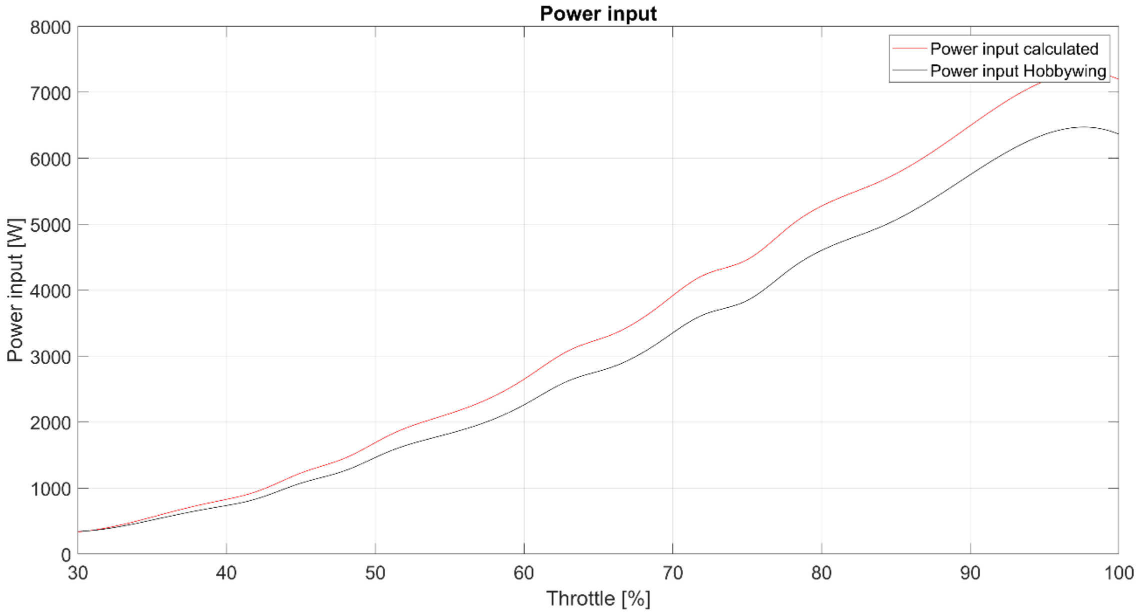

Figure 65: Power input [W] vs Throttle [%]

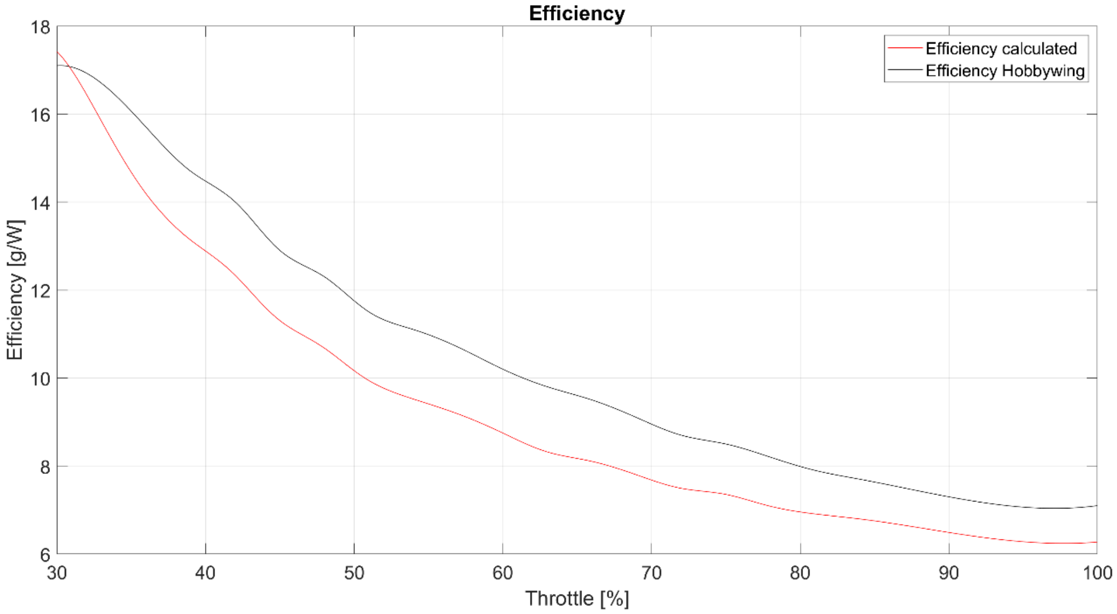

Figure 66: Efficiency [g/W] vs Throttle [%]

The payload was determined by calculating the difference between the thrust vector and the empty weight of the drone. For each configuration, the maximum payload was computed considering the power supplied by the fuel cell, which was set to either 1600 W or 2400 W. In essence, the procedure consisted of fixing the available power, evaluating the corresponding thrust, and then subtracting the empty weight of the drone.

To calculate the endurance, hydrogen consumption (in [g/s]) was first computed:

$$H_2\ consumption\ [\frac{g}{s}] = \frac{Power\ input}{0.45 * 120 * 1000}$$

Where:

- Power input is expressed in [W]=[J/s]
- 0.45 is the fuel cell efficiency (45%)
- 120 [kJ/g] is the hydrogen LHV (Lower Heating Value)
- 1000 is a conversion factor from [kJ] to [J]

The endurance can now be calculated based on the mass of hydrogen stored in the tank:

$$Endurance\ [\mathrm{min}] = \frac{m_{H_2}}{H_2\ consumption * 60}$$

The hydrogen mass is 140 g in the 6.8 L tank, 180 g in the 9 L tank and 260 g in the 10.8 L tank, while the factor 1/60 is applied to convert from seconds to minutes.

Table 15 represents a summary of the various configurations, highlighting the corresponding combination of endurance with zero payload and with maximum payload at sea level. The final column indicates the total cost of the respective configuration.

Table 15: Configurations summary

Configuration	Weight [g]	Payload at sea level [g]	Endurance [min]	Cost [€]
FC 2400 W + 6.8 L	16737.87	0	77.4825	39633
	16737.87	4968.5	52.4946	
FC 2400 W + 9 L	17737.87	0	91.31	39183
	17737.87	3968.5	67.4931	
FC 2400 W + 10.8 L	17987.87	0	129.1919	43317
	17987.87	3718.5	97.49	
FC 1600 W + 6.8 L	14693.87	0	94.2101	32624
	14693.87	1872.4	78.7335	
FC 1600 W + 9 L	15693.87	0	109.7709	32174
	15693.87	872.4	101.2287	
FC 1600 W + 10.8 L	15943.87	0	154.8025	36308
	15943.87	622.4	146.2193	

By using the same configuration as the tested quadcopter (2400 W fuel cell combined with the 9 L hydrogen tank) the MTOW is approximately 17.7 kg, which corresponds to a reduction of approximately 1 kg compared to the drone used in the test. This results in lower power demand, and therefore reduced hydrogen consumption, ultimately leading to increased endurance.

Calculating the power requirement based on the same propulsive efficiency, the estimated endurance at zero payload reaches approximately 91 minutes. This represents an improvement of 14% compared to the theoretical value of nearly 80 minutes calculated for the quadcopter in section 3.4.1, page 59.

The last option reported in Table 15 is indeed the most interesting configuration: with a power system consisting of two 800 W fuel cells and the 10.8 L hydrogen tank, the hexacopter could fly for roughly 150 minutes, although only with a very low payload.

From the economic point of view, the most influential factor is clearly the fuel cell: with the most affordable configuration (composed by the 1600 W fuel cell setup and the 9 L tank) it would be possible to achieve about 110 minutes of flight time with zero payload. The higher cost of the 10.8 L tank is justified by the significant increase in endurance.

Overall, the choice of configuration depends on the mission requirements: if a higher payload is needed, the throttle can be increased at the expense of endurance; conversely, reducing the throttle lowers consumption and therefore extends flight time.

The following plots show how endurance (in minutes) varies as a function of payload (in kilograms). The red curve represents the values calculated, while the black curve is based on the data provided by Hobbywing.

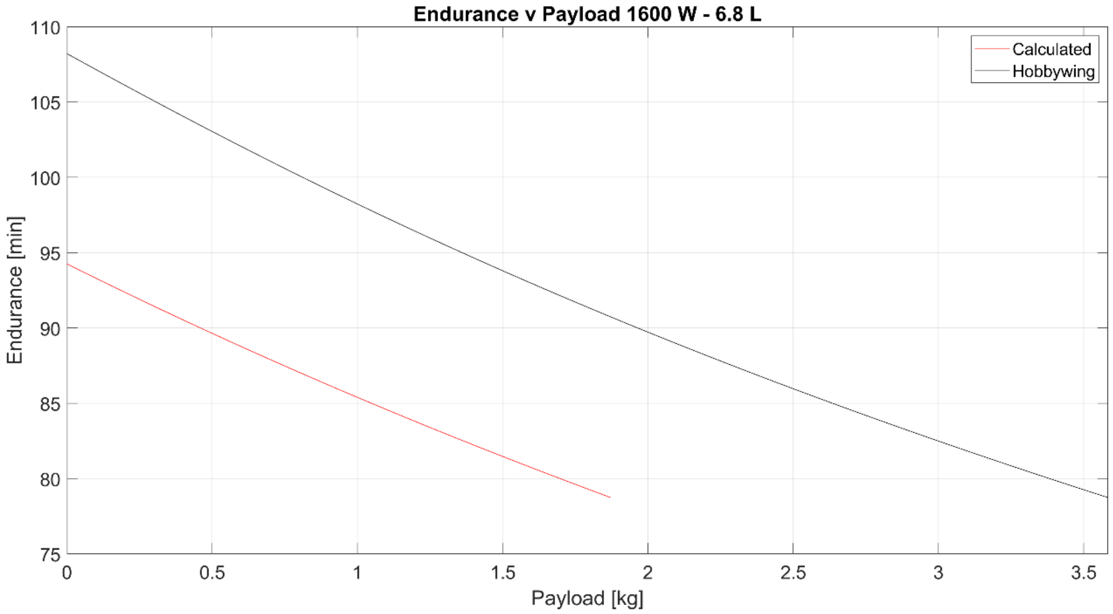

Figure 67: Endurance [min] vs Payload [kg] - 1600 W+6.8 L

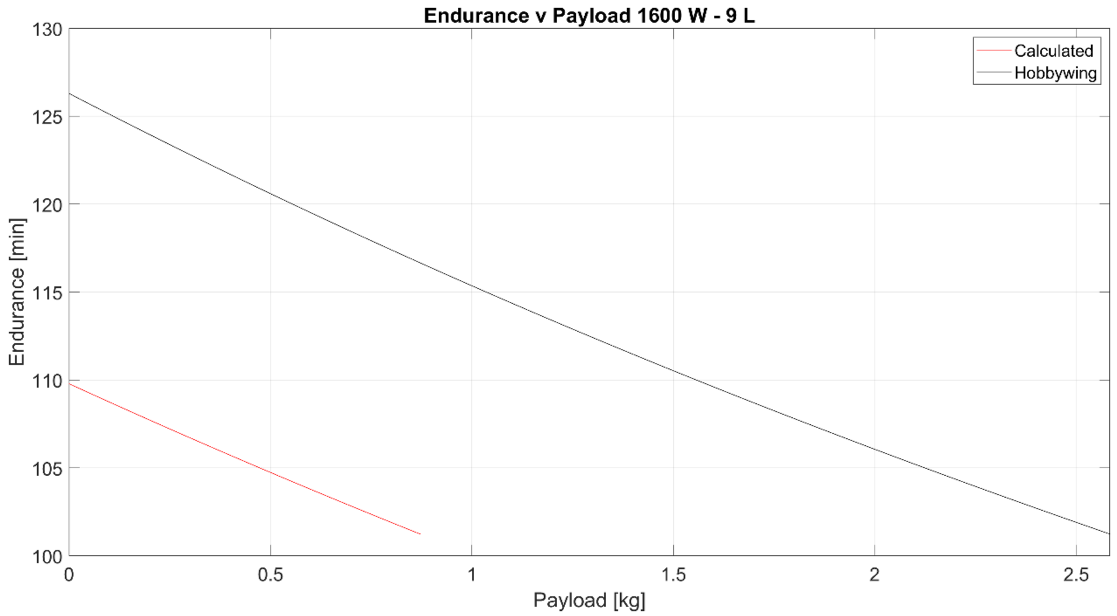

Figure 68: Endurance [min] vs Payload [kg] - 1600 W+9 L

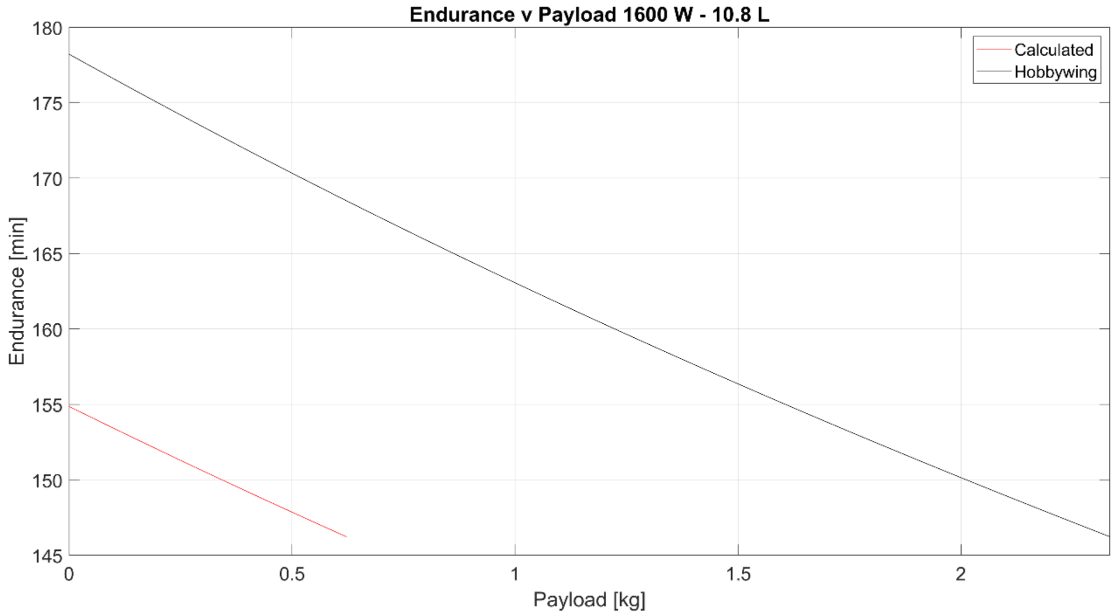

Figure 69: Endurance [min] vs Payload [kg] - 1600 W+10.8 L

The configurations equipped with the 2400 W fuel cell offer slightly reduced endurance, but they are capable of carrying a significantly higher payload, with the configuration 2400 W+6.8 L which could afford almost 5 kg for more than 50 minutes.

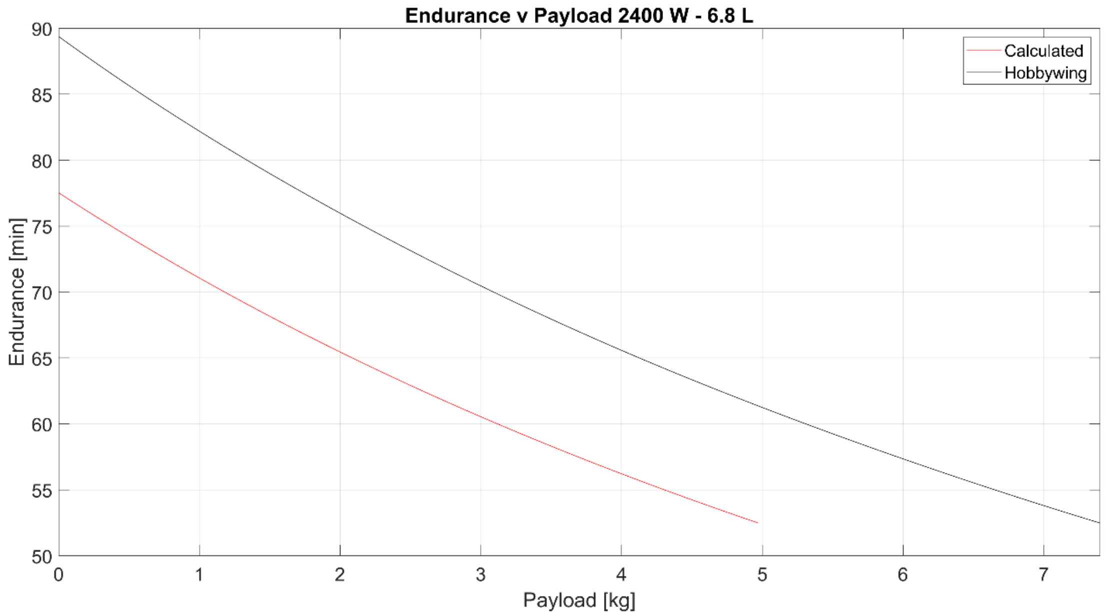

Figure 70: Endurance [min] vs Payload [kg] - 2400 W+6.8 L

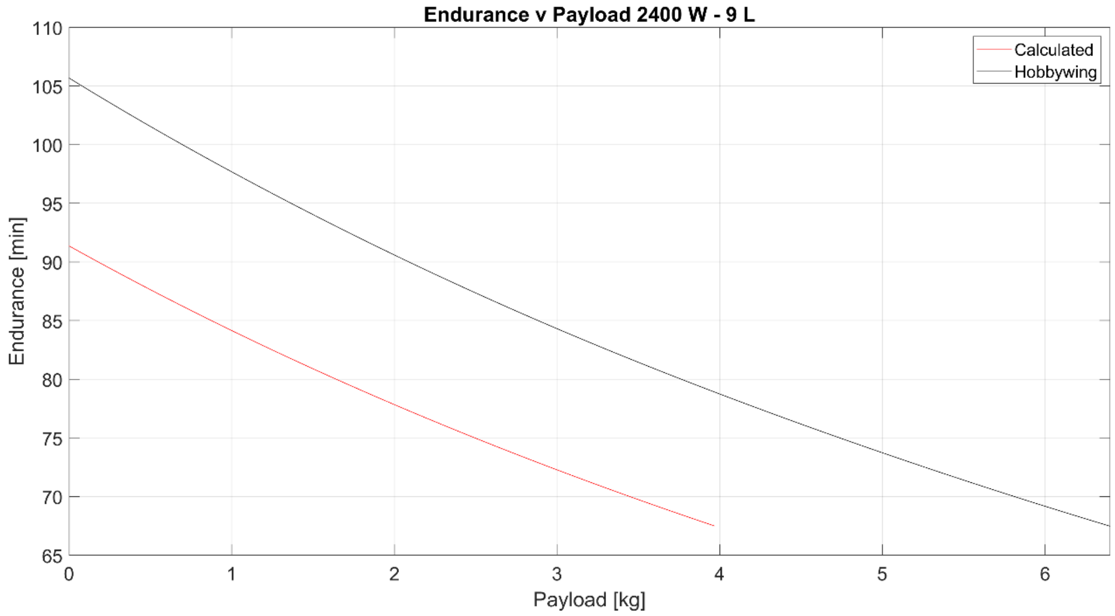

Figure 71: Endurance [min] vs Payload [kg] - 2400 W+9 L

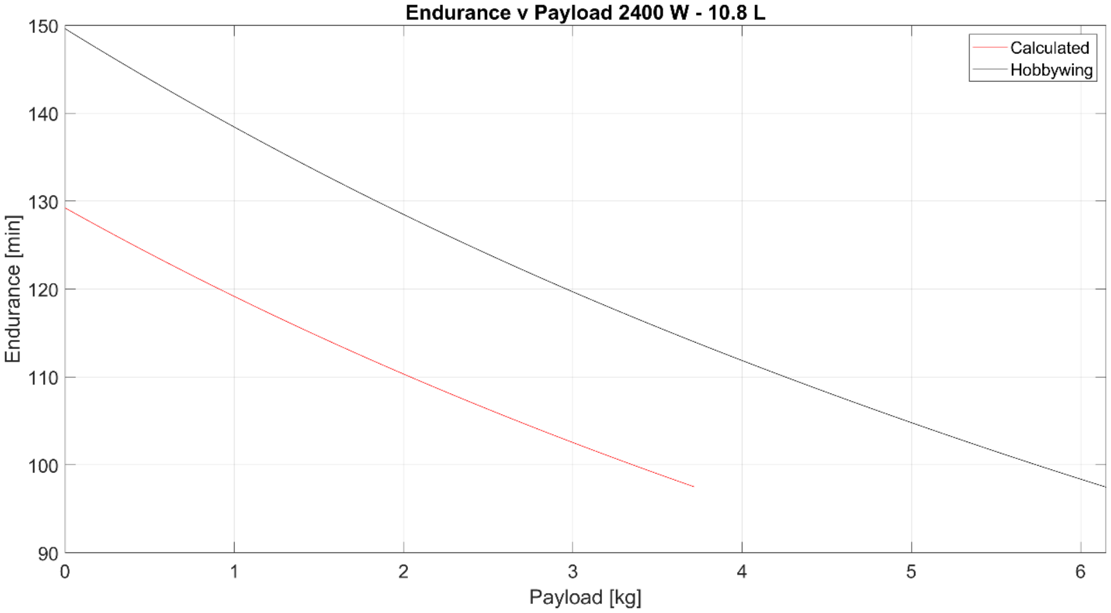

Figure 72: Endurance [min] vs Payload [kg] - 2400 W+10.8 L

5 Conclusions

The primary objective of this thesis was to investigate and experimentally validate a hybrid power system combining a hydrogen fuel cell and a battery for application on an unmanned aerial vehicle (UAV). This approach aimed at leveraging the high energy density of hydrogen with the fast response and power buffering capabilities of batteries, in order to enhance flight endurance and overall system efficiency.

The proposed hybrid architecture was first characterized through extensive bench testing, which provided key performance data and confirmed the feasibility of the design under controlled conditions. Subsequently, a flight test was conducted to evaluate the system in a real operational scenario. The results demonstrated that the hybrid hydrogen-battery system operated reliably during flight, and the performance metrics closely matched the experimental data obtained during bench testing. This consistency validates the robustness of the integration strategy and confirms that the system can deliver stable power supply while meeting the dynamic demands of UAV propulsion.

In addition to the experimental validation, a conceptual model of a hexacopter powered by the same hybrid architecture was developed. Preliminary evaluations suggest that such a configuration could potentially achieve higher efficiency compared to the tested quadcopter. With a lower MTOW, the hexacopter design could either provide greater endurance or accommodate a larger payload. This opens promising opportunities for applications requiring extended flight times or heavier mission equipment.

Beyond the technical validation, the successful implementation of this hybrid solution highlights its potential industrial and environmental implications. Hydrogen-based systems offer a promising pathway toward reducing carbon emissions in aviation, particularly for small and medium UAV platforms used in logistics, surveillance, and emergency response. By enabling longer endurance and cleaner energy sources, this technology can contribute to sustainable aerial operations and support the transition toward low-emission mobility.

Future research should focus on optimizing system weight and explore advanced energy management strategies, such as predictive algorithms for dynamic power distribution, and investigate the integration of complementary technologies. Additionally, the use of liquid hydrogen or alternative storage methods could further increase energy capacity, enabling longer missions and heavier payloads without compromising efficiency.

Ultimately, this research represents a step toward the next generation of UAVs powered by zero-emission technologies, paving the way for greener, more efficient aerial systems capable of meeting the growing demands of modern applications.

Acknowledgments

Desidero innanzitutto ringraziare il prof. Santarelli e Mohsen per la disponibilità durante lo sviluppo di questo lavoro di tesi.

Ringrazio profondamente Pierpaolo per avermi dato l'opportunità di svolgere la tesi in azienda, Michele, Paolo e Salvatore per la costante presenza e supporto e tutto il team di Dumarey per l'accoglienza e i preziosi consigli.

Infine, ci tengo a ringraziare la mia famiglia e i miei amici per avermi sempre supportato e motivato, festeggiando con me nei momenti belli e sostenendomi in quelli brutti.

Bibliography

[1] Z. Shen, S. Liu, W. Zhu, D. Ren, Q. Xu, and Y. Feng, “A Review on Key Technologies and Developments of Hydrogen Fuel Cell Multi-Rotor Drones,” *Energies*, vol. 17, no. 16, p. 4193, Aug. 2024, doi: 10.3390/en17164193.

[2] M. N. Boukoberine, M. F. Zia, M. Benbouzid, Z. Zhou, and T. Donateo, “Hybrid fuel cell powered drones energy management strategy improvement and hydrogen saving using real flight test data,” *Energy Convers. Manag.*, vol. 236, p. 113987, May 2021, doi: 10.1016/j.enconman.2021.113987.

[3] Q. Cai, D. J. L. Brett, D. Browning, and N. P. Brandon, “A sizing-design methodology for hybrid fuel cell power systems and its application to an unmanned underwater vehicle,” *J. Power Sources*, vol. 195, no. 19, pp. 6559–6569, Oct. 2010, doi: 10.1016/j.jpowsour.2010.04.078.

[4] J. Apeland, D. G. Pavlou, and T. Hemmingsen, “Sensitivity Study of Design Parameters for a Fuel Cell Powered Multirotor Drone,” *J. Intell. Robot. Syst.*, vol. 102, no. 1, p. 6, May 2021, doi: 10.1007/s10846-021-01363-9.

[5] J. Apeland, D. Pavlou, and T. Hemmingsen, “Suitability Analysis of Implementing a Fuel Cell on a Multirotor Drone,” *J. Aerosp. Technol. Manag.*, no. 12, p. e3220, Aug. 2020, doi: 10.5028/jatm.v12.1172.

[6] J. Dutczak, “Issues related to fuel cells application to small drones propulsion,” *IOP Conf. Ser. Mater. Sci. Eng.*, vol. 421, p. 042014, Oct. 2018, doi: 10.1088/1757-899X/421/4/042014.

[7] R. O’Hayre, S. Cha, W. Colella, and F. B. Prinz, *Fuel Cell Fundamentals*, 1st ed. Wiley, 2016. doi: 10.1002/9781119191766.

[8] A. Savvaris, Y. Xie, K. Malandrakis, M. Lopez, and A. Tsourdos, “Development of a fuel cell hybrid-powered unmanned aerial vehicle,” in *2016 24th Mediterranean Conference on Control and Automation (MED)*, Athens, Greece: IEEE, Jun. 2016, pp. 1242–1247. doi: 10.1109/MED.2016.7536038.

[9] O. Z. Sharaf and M. F. Orhan, “An overview of fuel cell technology: Fundamentals and applications,” *Renew. Sustain. Energy Rev.*, vol. 32, pp. 810–853, Apr. 2014, doi: 10.1016/j.rser.2014.01.012.

[10] H. Tsuchiya, “Mass production cost of PEM fuel cell by learning curve,” *Int. J. Hydrog. Energy*, vol. 29, no. 10, pp. 985–990, Aug. 2004, doi: 10.1016/j.ijhydene.2003.10.011.

[11] H. M. Irshad and S. Shahgaldi, “Comprehensive review of bipolar plates for proton exchange membrane fuel cells with a focus on materials, processing methods and characteristics,” *Int. J. Hydrog. Energy*, vol. 111, pp. 462–487, Mar. 2025, doi: 10.1016/j.ijhydene.2025.02.300.

[12] S. Porstmann, T. Wannemacher, and W.-G. Drossel, “A comprehensive comparison of state-of-the-art manufacturing methods for fuel cell bipolar plates including anticipated future industry trends,” *J. Manuf. Process.*, vol. 60, pp. 366–383, Dec. 2020, doi: 10.1016/j.jmapro.2020.10.041.

[13] A. Hermann, T. Chaudhuri, and P. Spagnol, “Bipolar plates for PEM fuel cells: A review,” *Int. J. Hydrog. Energy*, vol. 30, no. 12, pp. 1297–1302, Sep. 2005, doi: 10.1016/j.ijhydene.2005.04.016.

[14] Fan R., Peng Y., Tian H., Zheng J., Ming P., and Zhang C., “Graphite-Filled Composite Bipolar Plates for Fuel Cells: Material, Structure, and Performance,” *Acta Phys. Chim. Sin.*, vol. 0, no. 0, pp. 2009095–0, 2020, doi: 10.3866/PKU.WHXB202009095.

[15] Y. Song *et al.*, “Review on current research of materials, fabrication and application for bipolar plate in proton exchange membrane fuel cell,” *Int. J. Hydrog. Energy*, vol. 45, no. 54, pp. 29832–29847, Nov. 2020, doi: 10.1016/j.ijhydene.2019.07.231.

[16] Yu. A. Dobrovol’skii *et al.*, “Materials for bipolar plates for proton-conducting membrane fuel cells,” *Russ. J. Gen. Chem.*, vol. 77, no. 4, pp. 752–765, Apr. 2007, doi: 10.1134/S1070363207040366.

[17] Y. Gou, G. Jiang, J. Geng, and Z. Shao, “Properties of NbC/a-C:H films on titanium bipolar plates for proton exchange membrane fuel cells,” *Fuel Cells*, vol. 23, no. 1, pp. 51–59, 2023, doi: 10.1002/fuce.202200049.

[18] A. Sveshnikova, K. Abrosimov, A. Khayrullina, and A. Ustinov, “Effect of ambient air conditions on PEM fuel cell performance,” *J. Renew. Sustain. Energy*, vol. 9, no. 4, p. 044301, Jul. 2017, doi: 10.1063/1.5001138.

[19] “Gas diffusion layer”, [Online]. Available: https://www.sciencedirect.com/topics/engineering/gas-diffusion-layer

[20] N. Zamel and X. Li, “Effective transport properties for polymer electrolyte membrane fuel cells – With a focus on the gas diffusion layer,” *Prog. Energy Combust. Sci.*, vol. 39, no. 1, pp. 111–146, Feb. 2013, doi: 10.1016/j.pecs.2012.07.002.

[21] “Aquivion - an overview | ScienceDirect Topics.” Accessed: Oct. 16, 2025. [Online]. Available: https://www.sciencedirect.com/topics/engineering/aquivion

[22] D. N. Ozen, B. Timurkutluk, and K. Altinisik, “Effects of operation temperature and reactant gas humidity levels on performance of PEM fuel cells,” *Renew. Sustain. Energy Rev.*, vol. 59, pp. 1298–1306, Jun. 2016, doi: 10.1016/j.rser.2016.01.040.

[23] S. Kim and I. Hong, “Effects of humidity and temperature on a proton exchange membrane fuel cell (PEMFC) stack,” *J. Ind. Eng. Chem.*, vol. 14, no. 3, pp. 357–364, May 2008, doi: 10.1016/j.jiec.2008.01.007.

[24] Z. Chen, D. Ingham, M. Ismail, L. Ma, K. J. Hughes, and M. Pourkashanian, “Effects of hydrogen relative humidity on the performance of an air-breathing PEM fuel cell: A numerical study,” *Int. J. Numer. Methods Heat Fluid Flow*, vol. 30, no. 4, pp. 2077–2097, Apr. 2020, doi: 10.1108/HFF-11-2018-0674.

[25] S. I. Nefedkin, M. A. Klimova, V. S. Glasov, V. I. Pavlov, and Y. V. Tolmachev, “Effect of the corrugated bipolar plate design on the self-humidification of a high power density PEMFC stack for UAVs,” *Fuel Cells*, vol. 21, no. 3, pp. 234–253, Jun. 2021, doi: 10.1002/fuce.202000163.

[26] J. Chen, H. He, Z. Zhang, J. Wu, and Y.-X. Wang, “Optimization and matching of the air loop system in a fuel cell for high-altitude application,” *Int. J. Hydrog. Energy*, vol. 141, pp. 523–535, Jun. 2025, doi: 10.1016/j.ijhydene.2024.11.193.

[27] “Open Cathode vs. Closed Cathode Fuel Cells,” Hydrogenergy Technologies. Accessed: Sep. 24, 2025. [Online]. Available: https://www.hydrogenergy.in/open-cathode-vs-closed-cathode-fuel-cells

[28] P. Koski, J. Viitakangas, and J. Ihonen, “Determination of fuel utilisation and recirculated gas composition in dead-ended PEMFC systems,” *Int. J. Hydrog. Energy*, vol. 45, no. 43, pp. 23201–23226, Sep. 2020, doi: 10.1016/j.ijhydene.2020.04.252.

[29] Q. Chen, G. Zhang, X. Zhang, C. Sun, K. Jiao, and Y. Wang, “Thermal management of polymer electrolyte membrane fuel cells: A review of cooling methods, material properties, and durability,” *Appl. Energy*, vol. 286, p. 116496, Mar. 2021, doi: 10.1016/j.apenergy.2021.116496.

[30] H. Q. Nguyen and B. Shabani, “Proton exchange membrane fuel cells heat recovery opportunities for combined heating/cooling and power applications,” *Energy Convers. Manag.*, vol. 204, p. 112328, Jan. 2020, doi: 10.1016/j.enconman.2019.112328.

[31] G. Zhang and S. G. Kandlikar, “A critical review of cooling techniques in proton exchange membrane fuel cell stacks,” *Int. J. Hydrog. Energy*, vol. 37, no. 3, pp. 2412–2429, Feb. 2012, doi: 10.1016/j.ijhydene.2011.11.010.

[32] M. Ramezanizadeh, M. Alhuyi Nazari, M. Hossein Ahmadi, and L. Chen, “A review on the approaches applied for cooling fuel cells,” *Int. J. Heat Mass Transf.*, vol. 139, pp. 517–525, Aug. 2019, doi: 10.1016/j.ijheatmasstransfer.2019.05.032.

[33] A. Baroutaji *et al.*, “Advancements and prospects of thermal management and waste heat recovery of PEMFC,” *Int. J. Thermofluids*, vol. 9, p. 100064, Feb. 2021, doi: 10.1016/j.ijft.2021.100064.

[34] Z. You, L. Wang, Y. Han, and F. Zare, “System Design and Energy Management for a Fuel Cell/Battery Hybrid Forklift,” *Energies*, vol. 11, no. 12, p. 3440, Dec. 2018, doi: 10.3390/en11123440.

[35] J. C. Kurnia, B. A. Chaedir, A. P. Sasmito, and T. Shamim, “Progress on open cathode proton exchange membrane fuel cell: Performance, designs, challenges and future directions,” *Appl. Energy*, vol. 283, p. 116359, Feb. 2021, doi: 10.1016/j.apenergy.2020.116359.

[36] V. A. s.r.o, “Air Cooled v Liquid Cooled PEM Fuel Cell Stacks.” Accessed: Sep. 22, 2025. [Online]. Available: https://www.horizoneducational.com/air-cooled-v-liquid-cooled-pem-fuel-cell-stacks/t1643

[37] J. Apeland, D. Pavlou, and T. Hemmingsen, “State-of-Technology and Barriers for Adoption of Fuel Cell Powered Multirotor Drones,” in *2020 International Conference on Unmanned Aircraft Systems (ICUAS)*, Athens, Greece: IEEE, Sep. 2020, pp. 1359–1367. doi: 10.1109/ICUAS48674.2020.9213971.

[38] Q. Wu, Y. Zhang, T. Ru, and C. Cai, “Improved sliding mode temperature control of hydrogen fuel cells for multirotor drones,” *Frankl. Open*, vol. 10, p. 100214, Mar. 2025, doi: 10.1016/j.fraope.2025.100214.

[39] J. Zhao, W. Wei, L. Zhao, N. Xie, T. Yang, and K. Jiang, “Multi-objective optimization of PEMFC performance at different altitudes through integrated RSM, NSGA-II, EWM, and TOPSIS methodology,” *Int. J. Hydrog. Energy*, vol. 177, p. 151615, Oct. 2025, doi: 10.1016/j.ijhydene.2025.151615.

[40] Y. Zhang, Z. Jia, Z. Yuan, T. Yang, Y. Qi, and D. Zhao, “Development and Application of Hydrogen Storage,” *J. Iron Steel Res. Int.*, vol. 22, no. 9, pp. 757–770, Sep. 2015, doi: 10.1016/S1006-706X(15)30069-8.

[41] M. Li *et al.*, “Review on the research of hydrogen storage system fast refueling in fuel cell vehicle,” *Int. J. Hydrog. Energy*, vol. 44, no. 21, pp. 10677–10693, Apr. 2019, doi: 10.1016/j.ijhydene.2019.02.208.

[42] S. M. Cho, C. Kim, K. S. Kim, and D. K. Kim, “Lightweight hydrogen storage cylinder for fuel cell propulsion systems to be applied in drones,” *Int. J. Press. Vessels Pip.*, vol. 194, p. 104428, Dec. 2021, doi: 10.1016/j.ijpvp.2021.104428.

[43] E. A. Yatsenko, B. M. Goltsman, Y. V. Novikov, A. I. Izvarin, and I. V. Rusakevich, “Review on modern ways of insulation of reservoirs for liquid hydrogen storage,” *Int. J. Hydrog. Energy*, vol. 47, no. 97, pp. 41046–41054, Dec. 2022, doi: 10.1016/j.ijhydene.2022.09.211.

[44] W. Osborn *et al.*, “Solid-state hydrogen storage: Storage capacity, thermodynamics, and kinetics,” *JOM*, vol. 61, no. 4, pp. 45–51, Apr. 2009, doi: 10.1007/s11837-009-0051-5.

[45] M. Saad Salman, N. Rambhujun, C. Pratthana, Q. Lai, P. Sapkota, and K.-F. Aguey-Zinsou, “Solid-state hydrogen storage as a future renewable energy technology,” in *Nano Tools and Devices for Enhanced Renewable Energy*, Elsevier, 2021, pp. 263–287. doi: 10.1016/B978-0-12-821709-2.00020-7.

[46] S. S. Samantaray, S. T. Putnam, and N. P. Stadie, “Volumetrics of Hydrogen Storage by Physical Adsorption,” *Inorganics*, vol. 9, no. 6, p. 45, Jun. 2021, doi: 10.3390/inorganics9060045.

[47] E. Özbek, G. Yalin, S. Ekici, and T. H. Karakoc, “Evaluation of design methodology, limitations, and iterations of a hydrogen fuelled hybrid fuel cell mini UAV,” *Energy*, vol. 213, p. 118757, Dec. 2020, doi: 10.1016/j.energy.2020.118757.

[48] O. Erdinc and M. Uzunoglu, “Recent trends in PEM fuel cell-powered hybrid systems: Investigation of application areas, design architectures and energy management approaches,” *Renew. Sustain. Energy Rev.*, vol. 14, no. 9, pp. 2874–2884, Dec. 2010, doi: 10.1016/j.rser.2010.07.060.

[49] S. Ahmadi, S. M. T. Bathaee, and A. H. Hosseinpour, “Improving fuel economy and performance of a fuel-cell hybrid electric vehicle (fuel-cell, battery, and ultra-capacitor) using optimized energy management strategy,” *Energy Convers. Manag.*, vol. 160, pp. 74–84, Mar. 2018, doi: 10.1016/j.enconman.2018.01.020.

[50] L. Karunarathne, J. T. Economou, and K. Knowles, “Power and energy management system for fuel cell unmanned aerial vehicle,” *Proc. Inst. Mech. Eng. Part G J. Aerosp. Eng.*, vol. 226, no. 4, pp. 437–454, Apr. 2012, doi: 10.1177/0954410011409995.

[51] X. Zhang, Y. Zhang, X. Wang, T. Ru, and C. Cai, “Energy equivalent consumption and optimization strategies for hybrid hydrogen fuel systems in multirotor drones,” *Frankl. Open*, vol. 10, p. 100211, Mar. 2025, doi: 10.1016/j.fraope.2025.100211.

[52] J. Dutczak, “Compressed hydrogen storage in contemporary fuel cell propulsion systems of small drones,” *IOP Conf. Ser. Mater. Sci. Eng.*, vol. 421, p. 042013, Oct. 2018, doi: 10.1088/1757-899X/421/4/042013.

[53] P. Di Giorgio, S. Mafrici, M. Mabritto, G. Ristorto, M. Mansourkiaei, and M. Santarelli, “Design and Validation of a Hydrogen Fuel Cell-Powered Multirotor Drone for Long-Endurance Missions,” 2025. doi: 10.2139/ssrn.5723343.

[54] S. Tasevski, “Review of Hydrogen Storage in Fuel Cell Propulsion Systems of Small Drones.” Accessed: Oct. 31, 2025. [Online]. Available: https://dronebelow.com/2018/10/23/review-of-hydrogen-storage-in-fuel-cell-propulsion-systems-of-small-drones/

[55] FuelCellWorks, “MetaVista Breaks Guinness World Record of Multi Rotor UAV Flight Time Using Intelligent Energy Fuel Cell Power Module - Fuelcellsworks.” Accessed: Sep. 30, 2025. [Online]. Available: https://fuelcellsworks.com/news/metavista-breaks-guinness-world-record-of-multi-rotor-uav-flight-time-using-intelligent-energy-fuel-cell-power-module

[56] “BK-precision 8520 electronic load.” [Online]. Available: https://www.bkprecision.com/products/dc-electronic-loads/8520

[57] “Multifunctional Electronic Load PLZ-5W Series,” KIKUSUI ELECTRONICS CORP. Accessed: Sep. 22, 2025. [Online]. Available: https://global.kikusui.co.jp/w2-2/electronic-load-en/plz-5w_5wz-en/plz-5w-series/

[58] “Reliable EL-FLOW Select mass flow meter/controller,” Bronkhorst. Accessed: Sep. 22, 2025. [Online]. Available: https://www.bronkhorst.com/products/gas-flow/el-flow-select/

[59] “Intelligent Energy - IE-SOAR 2.4 fuel cells for drones.” [Online]. Available: https://www.intelligent-energy.com/our-products/ie-soar-fuel-cells-for-uavs/ie-soar-2-4/

[60] Intelligent Energy, “IE-SOAR 2.4kW.” Accessed: May 05, 2025. [Online]. Available: https://www.intelligent-energy.com/wp-content/uploads/2022/09/ie-soar-24kw.pdf

[61] “what is a lipo battery？,” https://www.pknergy.com/. Accessed: Sep. 22, 2025. [Online]. Available: https://pknergy.com:443/news/what-is-a-lipo-battery/

[62] “What is NI LabVIEW? Graphical Programming for Test & Measurement.” Accessed: Sep. 22, 2025. [Online]. Available: https://www.ni.com/en/shop/labview.html

[63] “Gryphon Hydrogen Endurance Drone,” The Bionic Eye. Accessed: Dec. 09, 2025. [Online]. Available: https://shop.thebioniceye.co.uk/products/gryphon-hydrogen-drone

[64] HOBBYWING, “H8M - Integrated Propulsion System for Industrial Drones,” HOBBYWING. Accessed: Dec. 09, 2025. [Online]. Available: https://www.hobbywing.com/en/products/h8m

[65] “Buy Hobbywing CM-H8M-8108-85KV-CW at Hobbywing UAV - Hobbywing UAV.” Accessed: Dec. 09, 2025. [Online]. Available: https://hobbywinguav.com/product/cm-h8m/

[66] “Buy Hobbywing ML 30*9.8" at Hobbywing UAV - Hobbywing UAV.” Accessed: Dec. 09, 2025. [Online]. Available: https://hobbywinguav.com/product/ml-309-8/

[67] “MadeInAdd | Produzione on-demand: Stampa 3D, CNC.” Accessed: Dec. 09, 2025. [Online]. Available: https://www.madeinadd.com/it

[68] “IE-SOAR 800WHydrogen Fuel Cell,” The Bionic Eye. Accessed: Dec. 09, 2025. [Online]. Available: https://shop.thebioniceye.co.uk/products/ie-soar-800-hydrogen-fuel-cell

[69] “Hydrogen Tank,” Doosan Mobility Innovation. Accessed: Dec. 09, 2025. [Online]. Available: https://www.doosanmobility.com/en/products/hydrogen-tank/

[70] “10.8 litre DMI Hydrogen Tank,” The Bionic Eye. Accessed: Dec. 09, 2025. [Online]. Available: https://shop.thebioniceye.co.uk/products/10-8l-dmi-hydrogen-tank